DE# 0420-9

DOE/ID/12566-T1
(DE88004025)

Energy CONSERVATION

ASSESSMENT OF STRENGTH LIMITING FLAWS IN CERAMIC HEAT EXCHANGER COMPONENTS

Final Report for the Period September 28, 1984—June 30, 1986

Phase I

By
T. Powers
J. Snyder

October 1986

Work Performed Under Contract No. AC07-84ID12566

For
U. S. Department of Energy
Office of Industrial Programs
Washington, D.C.

By
Babcock & Wilcox Company
Lynchburg, Virginia

DISCLAIMER

DISCLAIMER

Available from the National Technical Information Service, U. S. Department of Commerce, Springfield, Virginia 22161.

Price: Printed Copy A08
Microfiche A01

Codes are used for pricing all publications. The code is determined by the number of pages in the publication. Information pertaining to the pricing codes can be found in the current issues of the following publications, which are generally available in most libraries: *Energy Research Abstracts (ERA); Government Reports Announcements* and Index *(GRA* and I); *Scientific and Technical Abstract Reports (STAR);* and publication NTIS-PR-360 available from NTIS at the above address.

Printed in the United States of America
USDOE Office of Scientific and Technical Information
Oak Ridge, Tennessee

DOE/ID/12566-T1
(DE88004025)
Distribution Category UC-95f

ASSESSMENT OF STRENGTH LIMITING FLAWS IN CERAMIC HEAT EXCHANGER COMPONENTS

Final Report
Phase I
September 28, 1984 - June 30, 1986

by

T. Powers
J. Snyder

October 1986

Work Performed Under Contract No. DE-AC07-84ID12566

Prepared for
U.S. Department of Energy
Idaho Operations Office, Idaho Falls, Idaho
Sponsored by the Office of the Assistant Secretary for
Conservation and Renewable Energy
Office of Industrial Programs
Washington, DC

Prepared by
Babcock & Wilcox Company
Research & Development Division
Lynchburg Research Center
Lynchburg, VA 24506

LEGAL NOTICE

"This report was prepared by Babcock & Wilcox (B&W) as an account of work sponsored by the U.S. Department of Energy Idaho National Engineering Laboratory (INEL). Neither INEL members of INEL, nor B&W nor any person acting on behalf of either:

a. Makes any warranty or representation, expressed or implied with respect to the accuracy, completeness, or usefulness of the information contained in this report, or that the use of any information, apparatus, method, or process disclosed in this report may not infringe privately owned rights; or

b. Assumes any liability with respect to the use of, or for damages resulting from the use of, any information, apparatus, method or process disclosed in this report.

ABSTRACT

Assurance of energy efficient design lifetimes of high temperature structural ceramics requires the ability to specify acceptance criteria and to test to those criteria. These criteria will be established through nondestructive testing, to determine which defects are detectable, together with fracture mechanics, to calculate effects of indetectable flaws.

The first phase of this program is to examine heat exchanger material with four test methods which have shown promise for use in ceramics; ultrasonic scanning, microfocus x-ray, Scanning Laser Acoustic Microscope, and Acoustic Holography. The capabilities, limits, and potential for improvement of these are presented in this report. Destructive testing, material sectioning, and fractography are included.

FOREWORD

This project was funded through the U.S. Department of Energy - Idaho Operations and in collaboration with the Idaho National Engineering Laboratory and by Babcock & Wilcox.

ACKNOWLEDGEMENTS

This report reflects leadership efforts of the following project team members:

C. Youell, Administrative Manager
J. Bower, Acoustic Microscopy and Holography Technology
J. Coulter, Radiographic Technology
W. Lawrie, Ultrasonics Technology
H. Moeller, Ceramics Technology
D. Hindman, Ceramics Technology
T. Powers, Technical Manager - NDE
J. Snyder, Technical Manager - Ceramics

Numerous other technical staff members provided the support necessary to complete the technical work included herein; their contributions are gratefully acknowledged.

EXECUTIVE SUMMARY

This is the final report on Phase I of a potential three phase project. The ultimate goal is to be able to assure energy efficient design lifetimes of high temperature structural ceramics by being able to specify acceptance criteria. These criteria will be established through nondestructive testing, to determine which defects are present, and fracture mechanics, to determine the effects of any detected flaws. The strength of material with the worst possible undetectable flaw can be used to design a tube which will survive the design lifetime.

Phase I is an assessment of the applicability of various NDE methods to the inspection of silicon carbide heat exchanger tubes. The four methods investigated were ultrasonic testing, microfocus x-ray, acoustic holography, and the Scanning Laser Acoustic Microscope (SLAM).

All testing methods were limited by surface roughness and bulk porosity of the tube material. Improved porosity control and surface quality would greatly aid testing. In addition, fractography of fractured surfaces of test specimens implicated clusters of large grains in some cases.

Ultrasonic testing detected Electro-Discharge Machined (EDM) notches on both the inside and outside surfaces of tube sections. These similate surface breaking cracks, which are probably the worst possible defects. Minor inclusions were not reliability separated from porosity, and testing showed that minor inclusions and porosity were not generally strength limiting.

Microfocus x-ray is the only method to reliably locate inclusions of denser material. Surface condition and porosity limit sensitivity.

Acoustic holography was not able to produce any results, even on polished surfaces, because of porosity.

SLAM was able to detect outer surface EDM notches more quickly than the other test methods except real time radiography. It should do as well on real, tight, cracks which real time radiography would lack the sensitivity to locate.

Test specimens included both flat plates with seeded defects and sections of a heat exchanger tube. The seeded defects were ceramic fibers, wires, graphite spheres, and metal spheres. The tube samples were sections with EDM notches, samples of different geometries, and C-rings. The C-rings and bars from the flat samples were strength tested and the broken surfaces were examined to determine the cause of failure. Then the location of failure was ocmpared with previous NDE indications.

(This page intentionally left blank.)

CONTENTS

LIST OF FIGURES

LIST OF FIGURES (Continued)

LIST OF FIGURES (Continued)

LIST OF FIGURES (Continued)

LIST OF TABLES

Section 1
INTRODUCTION

Ceramic materials are attractive for use in heat exchangers because they retain their strength at higher temperatures than metal tubes. The tube material studied in this project was silicon carbide, which has a high thermal conductivity, an obvious benefit in a heat exchanger. The difficulty in the use of ceramic tubes is that ceramics are subject to brittle failure.

As advanced ceramics make the transition from research materials to high performance structural materials, it is essential to identify performance limiting conditions in the structures, to develop some means of assessing suitability for service, and to estimate expected lifetime. Energy efficiency and productivity both push designs toward minimal over-design, which limits the acceptability of marginal defects. The desired designs have higher mean stresses, and therefore the critical flaw size is smaller. The effects of various types of defects on lifetime and the limits of detection of these defects must be known for a rational, optimum design.

The object of this program is to assure energy efficient design lifetimes of high temperature structural ceramics. This requires acceptance criteria against which the components can be tested. These criteria must be beased on both knowledge of which defects can be detected through nondestructive methods and a fracture mechanics analysis of the effects of various flaws.

Phase I of this project includes the fabrication, inspection and mechanical testing of a range of material conditions that can limit strength and ultimately service lifetime. There is an evaluation of several material inspection technologies that were specifically developed to evaluate material conditions unique in ceramics, where flaw sizes an order of magnitude smaller than in metals can cause failure. Both natural flaws and artificially induced flaws in silicon carbide ceramics were destructively evaluated to establish preliminary strength limiting information and evaluate test methods. This data is used to establish technical direction and to define the scope of Phase II, which will lead us to the ultimate goal of life prediction.

These results provide a basis for Phase II; testing and fracture analysis model building of ceramics at room temperature and working temperature. The model will be subjected to testing, verification, modification, and extension of applicability in Phase III. The demonstrated testing methods will be extended as far as possible in Phase II to get the best sensitivity and discrimination, based on limitations and capabilities described in this report.

Section 2
REFINEMENT OF NONDESTRUCTIVE EXAMINATION (NDE) TECHNIQUES

2.1 INTRODUCTION

Four nondestructive examination (NDE) techniques were applied to the test specimens: conventional ultrasonics, microfocus X-Ray, Scanning Laser Acoustic Microscopy (SLAM), and acoustic holography. The following sections describe the equipment, the physical basis of the techniques, and their potential improvements.

Examination of the tube material was expected to be difficult because of fixturing problems, so some flat specimens of similar thickness were manufactured. Some of these had implanted defects. These deliberately implanted defects are described in Sections 3.2 and 3.3. The surface roughness of both the flat specimens, and the tube sections, caused difficulties for the acoustic techniques, so some of the flat specimens were ground and polished to provide baseline information. Testing on all specimens was directed toward determining the potentials of these techniques for use on as-manufactured tubes.

2.1.1 Literature Review

A brief literature review was undertaken with two objectives in mind; to find sources of information released since the last literature review in 1982, and to find any available data on the more practical aspects of NDE of ceramics.

To a large extent, the papers published in the last several years are repetitious of papers given earlier. Work is still being done on bulk wave and surface wave scattering,

and on the analogous interaction of a surface breaking crack with both static stress and low frequency Rayleigh waves. An additional paper on thermal wave imaging of vertical cracks in opaque solids included some results on Knoop indentations in silicon carbide. Very little new information was elicited by this survey.

Negative results were also obtained on the other aspect of the literature survey: the practical application of NDE techniques. All of the results obtained using a variety of techniques involved ceramic samples with polished surfaces. Most of the papers fell in the category of technique development, with no practical applications. Although project activities involved some samples with polished surfaces, test personnel were constantly aware of the far-from-ideal surfaces of the heat exchanger tubing. The rough surfaces of the as-manufactured and tubing samples drastically limited the results that could be obtained because of the production of interfering density variations in radiography and significant scattering of ultrasound at the frequencies needed to detect small defects in ceramics. Information on how problems of this type could be solved was not found in the current literature.

2.2 TECHNIQUE DESCRIPTION

This section contains descriptions of the physical processes involved in the four selected nondestructive testing methodologies.

2.2.1 Microfocus Radiography

2.2.1.1 Radiographic Image Quality

Radiographic image quality can be defined in terms of spatial resolution and contrast sensitivity. The spatial

resolution of a radiographic system depends upon film graininess and the geometric unsharpness, U_g, given by

$$U_g = fb/a$$

where "f" is the focal spot size of the X-Ray source, "a" is the source-to-object distance, and "b" is the object-to-film distance.

A microfocus radiographic system having a focal spot size of the order of several micrometers allows the use of large magnification factors to image very small defects without geometric unsharpness. Therefore, the focal spot size of the X-Ray source is the limiting factor for spatial resolution using a microfocus system. A special image quality indicator (IQI), designed for use in semiconductor photolithography, was required to obtain an indirect measurement of the focal spot size of the X-Ray source. The IQI consisted of gold lines etched onto a polymer substrate where the gold thickness was 0.8 μm, and the gold lines had various widths and spacings. Figure 2-1 illustrates the dimensions of one individual test pattern in the IQI which included an array of approximately fifty of these test patterns. The radiographic film images of the IQI showed that the qold lines havinq a width of 3 μm and spacings of 4 μm could be resolved; however, the 2 μm width lines with 2 μm spacings could not be resolved. Therefore, the focal spot size (and basic spatial resolution) of the microfocus system was measured to be less than or equal to 4 μm but greater than 2 μm. Figure 2-2 is a photographic reproduction of an IQI radiographic film image where the magnification factor was approximately 60x. The two intersecting black lines in the radiographic image were 10 μm diameter tungsten wires used to obtain optimum beam focusing and centering on the target.

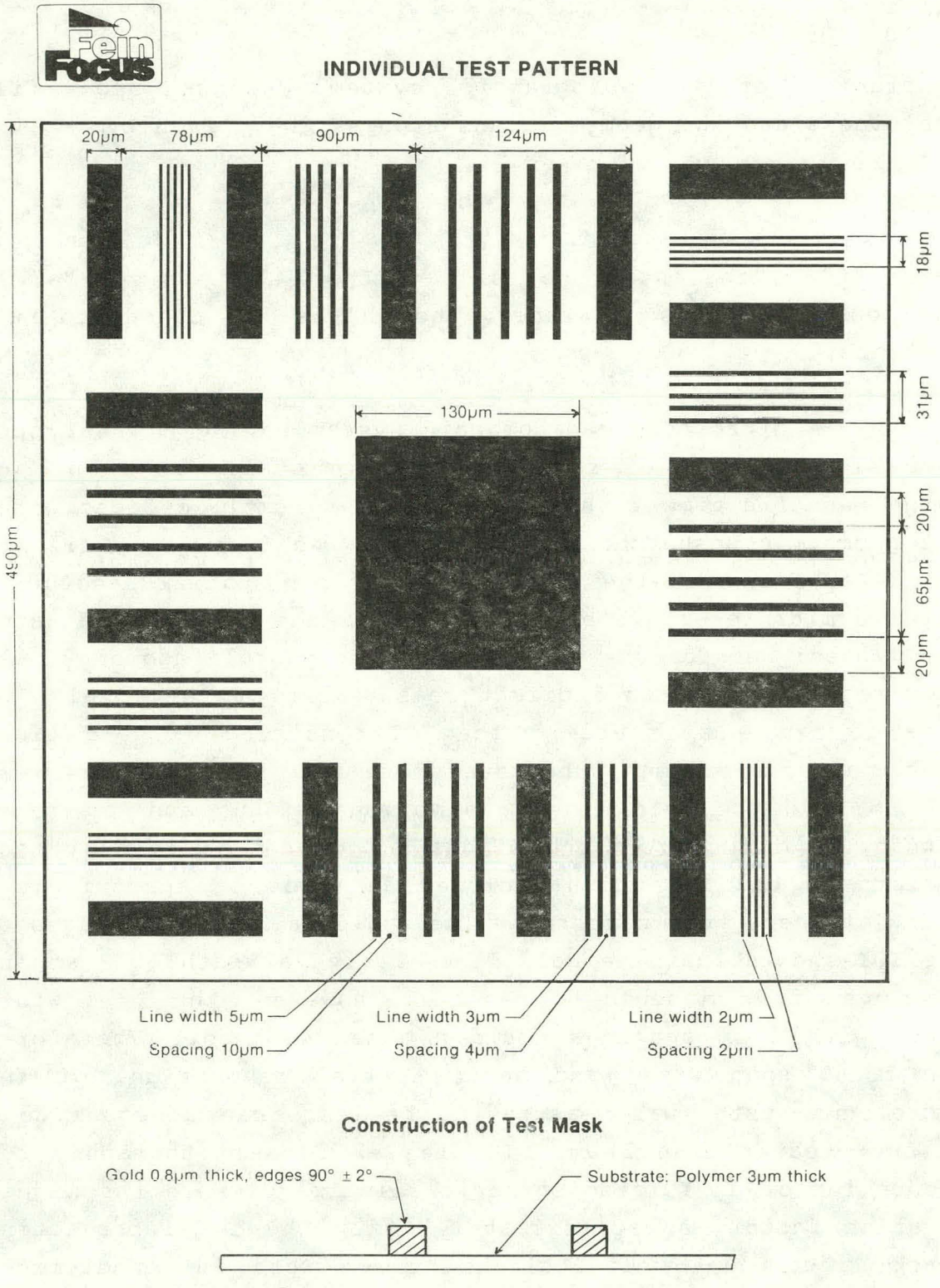

Figure 2-1. Test Pattern in Image Quality Indicator

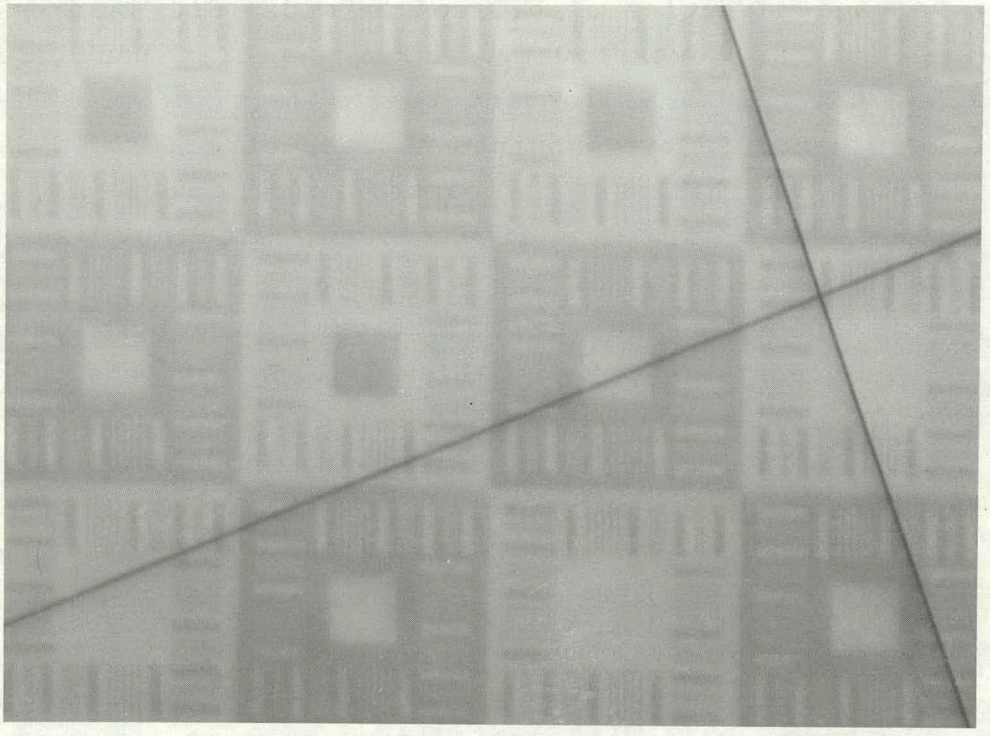

Figure 2-2. Radiographic Image of Image Quality Indicator Showing Spatial Resolution of Microfocus System

Contrast sensitivity depends upon three factors: film response, X-Ray absorption in the specimen, and visual response. Contrast sensitivity, "S", is defined by

$$S = \Delta x/x$$

where "Δx" is the defect depth or equivalent thickness change in the direction of the X-Ray beam and "x" is the specimen thickness.

Small particles of silicon carbide (SiC) were used to determine contrast sensitivity. The particles had irregular shapes and nominal sizes ranging from 900 to 75 μm. The particles were taped to the machined surface of a silicon carbide plate having a thickness of approximately 6.1 mm. The surfaces of the plate were fine ground, with no discernable roughness. The density of the plate was 99% of theoretical. Projection radiography using magnification factors of 5x or greater was required to visually distinguish the smallest particles having nominal sizes ranging from 63 to 88 μm. The radiographic film images of the SiC plate and particles showed that the percent contrast sensitivity was within the range of 1.0 to 1.5 percent. It was also noticed that both a single layer of scotch tape and residue from the adhesive used in grinding operations were visible.

In summary, radiographic image quality can be defined by the spatial resolution and contrast sensitivity of the radiographic system. The spatial resolution of the system determines the smallest linear dimension that can be resolved in a plane perpendicular to the X-Ray beam. Spatial resolution is independent of specimen material properties. Contrast sensitivity is determined by the smallest change in linear dimension that can be distinguished in a plane parallel

to the X-Ray beam. Contrast sensitivity is highly dependent upon specimen material properties. For silicon carbide type specimens having a nominal thickness of 6 mm, the contrast sensitivity is the dominant factor for defect detectability. The measured contrast sensitivity for SiC established a lower limit for the detectability of defects to sizes within the range of 60 to 90 μm.

2.2.2 SLAM Technique

The operation of the SLAM is discussed in Section 2.3.2 and illustrated in Figure 2-6. In the basic mode, a crack will produce a shadow region. However, for ceramics with rough surfaces, there is so much scattering that this does not work. The scattering not only fills in the crack's shadow, but also creates other apparent shadows by interference effects. During this project, an alternative mode of operation was developed; it works very well.

The essential feature of this new SLAM mode is to observe only the desired rays, not all the scattering. Reversing the direction of the sound beam is a major step. The rays reflected from the crack surface are detected as a bright spot in the field of view. Most of the scattered waves are in the forward direction of the beam, to which the SLAM is quite insensitive, thus reducing background clutter.

The SLAM is sensitive to waves arriving over a limited range of angles. This range is determined by the internal filtering and the local oscillator, because the signal arriving at the optical diode is near the ultrasonic frequency with a doppler shift determined by the relative velocities of the ultrasonic wave along the coverslip and the laser scan rate. Varying the local oscillator changes the

doppler shift which can pass the IF filter, and hence the directional sensitivity of the SLAM. Narrowing the reception range reduces the scattered wave reception.

The combination of reversing the sound field and narrowing the reception angle allows the detection of small surface cracks even in rough ceramics, such as heat recovery tube samples made of silicon carbide.

2.2.3 Conventional Ultrasonics

Conventional ultrasonic techniques are being used for wall thickness measurement and for defect detection. In industry, most conventional ultrasonic examinations are performed using frequencies between 1 and 10 MHz; occasionally, frequencies higher and lower than this are used. For silicon carbide heat exchanger tubes, material properties allow the use of much higher frequencies; in fact, the size of critical defects makes the use of higher frequencies mandatory.

The conventional ultrasonic techniques have been divided according to application. Separate techniques have been used to measure wall thickness, to detect embedded flaws and to detect surface flaws. Surface finish and sample shape must be considered during the selection and application of a technique. Many of the samples are in the form of flat, square plates. However, cylindrical and conical sections removed from a heat exchanger tube have also been used to verify that selected techniques can be applied to other geometrical configurations.

Throughout the application of conventional ultrasonic techniques, problems have arisen due to the combination of high ultrasonic velocities and rough surfaces. This will be discussed in Section 3.4.3.

2.2.3.1 Thickness Measurements

Ultrasonic thickness measurement is conceptually simple. The time for an ultrasonic pulse to make a round trip through the material is measured and the thickness is obtained as the product of half this time and the known sound velocity of the material. To obtain a well behaved ultrasonic pulse in the ceramic samples, the wavelength should be long compared to surface roughness. Low ultrasonic frequencies are used. However, the velocity in the ceramic is high so that short pulses are required if the incident pulse is to be completed before the reflected pulse returns. Low frequencies imply long periods so that, even with pulses of only one or two cycles, the pulse length is excessive.

The method of thickness measurement developed for this project employs long pulses at a relatively low frequency. The pulses are sufficiently long that a standing wave is established in the sample. The standing wave causes the reflection coefficient at the surface of the immersed sample to vary, depending upon the thickness to wavelength ratio. The pulses are generated by using a continuous oscillator and a gated amplifier. Changing the oscillator frequency changes the reflection coefficient at the sample surface, and the amplitude of the reflected pulses will cycle through maxima and minima. By measuring a number of the frequencies at which either maxima or minima occur, the fundamental thickness frequency can be obtained. The period corresponding to the fundamental frequency and the known sound velocity can then be used to obtain thickness.

It has been assumed that velocity is known. Unfortunately, for thickness measurements, velocity depends linearly upon density of the silicon carbide samples.

Velocity increases by about 8% over the range of 90 to 99% of theoretical density. This velocity variation produces an upper limit on the accuracy of ultrasonic thickness measurement. If density is unknown, then an ultrasonic measurement can only give an approximate thickness since velocity is also unknown.

2.2.3.2 Embedded Flaw Detection

The techniques used by both B&W and INEL to detect embedded flaws are in essence acoustic microscopy which utilizes highly focused ultrasonic transducers to produce magnified images. Resolution capabilities of this technique can rival those of optical microscopes when frequencies near 3 GHz are used. Unfortunately, with engineering materials such as silicon carbide, high frequencies are strongly attenuated thus reducing acoustic penetration. For this reason, frequencies less than 100 MHz are generally required to interrogate subsurface structure at the expense of resolution. For silicon carbide, the use of 50 MHz is a good compromise between resolution and penetration.

The resolution of an acoustic microscope is determined by the physical dimensions of the focal spot produced by the transducer on or in the test specimen. The equations which described the -6 dB focal spot diameter (E_d) and depth of field (E_x) in a medium are

$$E_d = 1.22\ L\ F/D \qquad (1)$$

$$E_x = 8.0\ L\ (F/D)^2 \qquad (2)$$

where L, F, and D are the acoustic wavelength in the medium, focal length, and element diameter, respectively. To ultra-

sonically examine internal sections of a sample the ultrasonic wave must propagate through two media generally with different acoustic velocities. This results in refraction of the ultrasonic wave at the interface which is described by Snell's law.

$$\text{Sin } \theta_1 / \text{ Sin } \theta_2 = C_1/C_2 \qquad (3)$$

where θ_1 and θ_2 are the incident and refracted angles and C_1 and C_2 are the acoustic velocities in medium 1 and 2, respectively. For this investigation, the measured longitudinal acoustic velocity for silicon carbide is 11.8 mm/μs; for water which is used as a couplant it is 1.48 mm/μs. For a focused acoustic beam propagating from water to silicon carbide, refraction results in reducing the focal length of the transducer to one eighth of its original length. The focal spot size E_d as described in Equation 1 is not significantly altered in the silicon carbide due to the approximate eightfold increase of L times the approximate eightfold decrease of (F/D). However, due to the square dependence of (F/D) in Equation 2, the depth of focus, E_x, in silicon carbide is about one eighth of that in water. Refraction of the longitudinal acoustic wave at the interface also imposes a limit upon the maximum incident angle. This angle is reached when Sin θ_2 of Equation 3 equals 1.0.

$$\theta_{cr} = \text{Sin}^{-1} (C_1/C_2) \qquad (4)$$

where θ_{cr} is called the first critical angle. Beyond this angle, the energy of the incident longitudinal wave can only penetrate the test piece through mode conversion to shear waves. Shear waves propagate at about one-half the longitudinal velocity and will produce a focal point deeper into the material. Utilization of shear waves for imaging is not always straightforward and is usually avoided. For silicon carbide in water, the critical angle, θ_{cr}, is 7.21 degrees. The previous discussion dealing with the interaction of an

acoustic wave with an interface has dealt only with flat surfaces. Curved surfaces can also be handled but the resulting quantitative expressions are more complex. In general, the depth of focus and actual shape and size of the focal spot will directly depend upon the radius of curvature of the interface through which the acoustic wave is refracted. Non-uniform concave or convex curvature or roughness of a sample surface will tend to defocus the acoustic wave and distort the focal spot, ultimately reducing resolution.

The ability to detect and size a defect depends upon its physical characteristics, position with respect to the focal point, and threshold settings. Assuming the same threshold settings, the farther from the focal point a defect is located, the larger it has to be before it is detected. This is primarily due to the increased size of the acoustic beam. Similar problems are encountered when a determination of the physical size of a defect is made. A defect located at the point of focus that is larger than the -6 dB focal spot diameter will be imaged at nearly its true size when the threshold is set to trigger at -6 dB of the signal's maximum amplitude. For example, with the appropriate conditions, a machined notch 0.517 mm wide by 1.541 mm long located on the back side of a 4.5 mm thick silicon carbide sample was imaged with a maximum dimensional error of 0.072 mm. Under any other conditions, a defect will not be directly sized but still may be detected.

2.2.4 Acoustic Holography System

A coherent burst of energy is generated by amplifying a gated portion of the signal from a stable, free running, sine wave oscillator, then using this signal to drive a transducer. The return echo signals are amplified and

compared to the reference signal from the oscillator in a double balanced mixer. The output of the mixer is the relative phase. The transducer is raster scanned to create a square array of this phase information which is the hologram.

The hologram and some other significant parameters, such as propagation time and angle, are used to reconstruct an image of the defect using a modified backward wave propagation algorithm. The image is then available for sizing and edge detection analysis.

Two major problems were encountered in applying this process to ceramics. First, because the wavelength is very short, the sample positions must be very close together and extremely accurately positioned. Second, because the beam must fill a large volume, the return signals are very weak. Because of these problems, it was not possible to acquire any holograms on any of the samples.

2.3 EQUIPMENT DESCRIPTION, SETUP, OPERATION

2.3.1 Microfocus X-Ray

The microfocus X-Ray system is shown in Figures 2-3 and 2-4. Figure 2-3 shows the control console for real time radiography and the X-Ray system controls. From this console the operator adjusts X-Ray tube current, voltage, and spot size while monitoring the X-Ray image and specimen position. Images can be computer enhanced and stored on videotape. Figure 2-4 shows the X-Ray room with H.V. supply, X-Ray tube and vacuum system, and image intensifier tube.

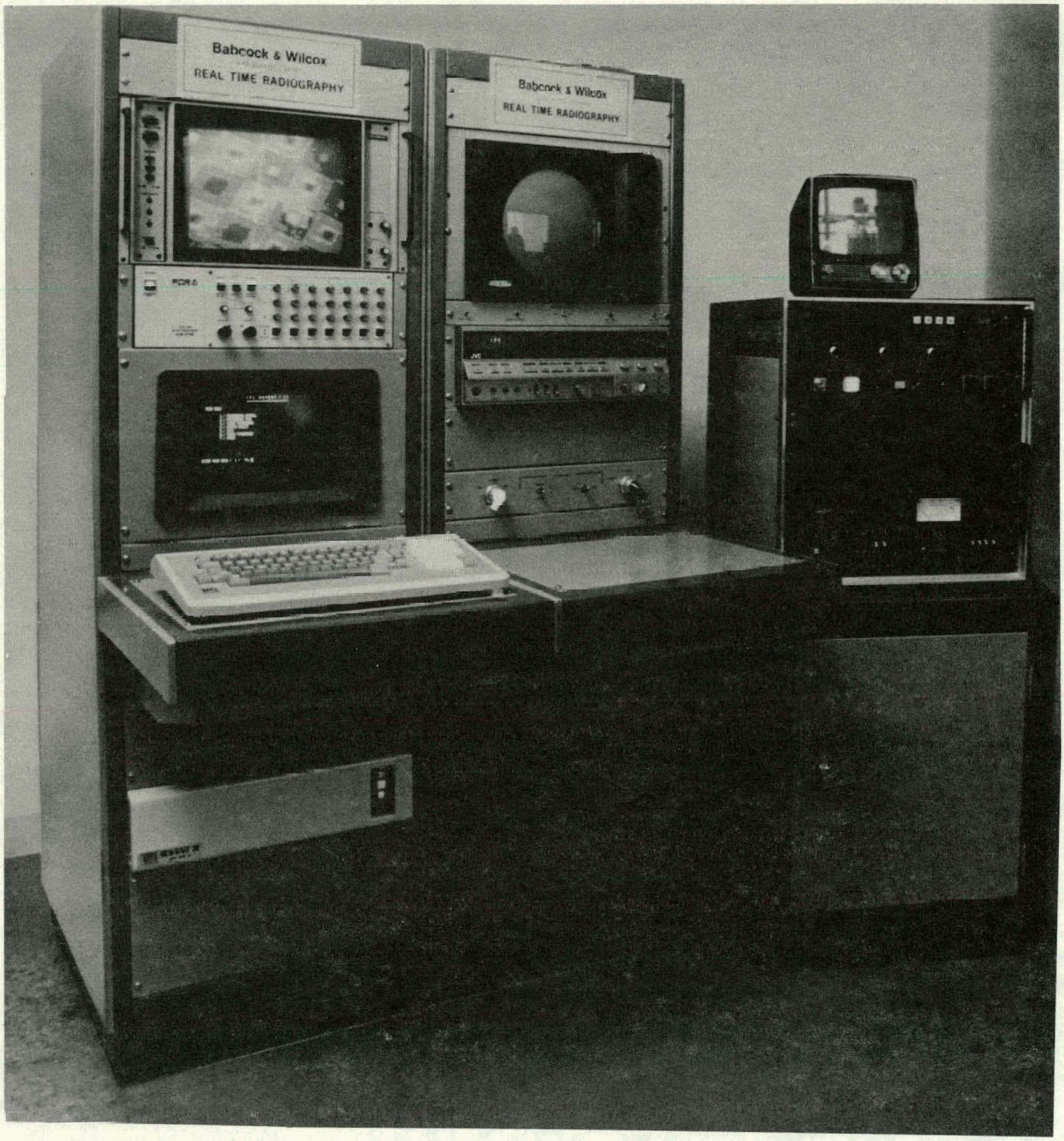

Figure 2-3. Microfocus X-Ray Control Console

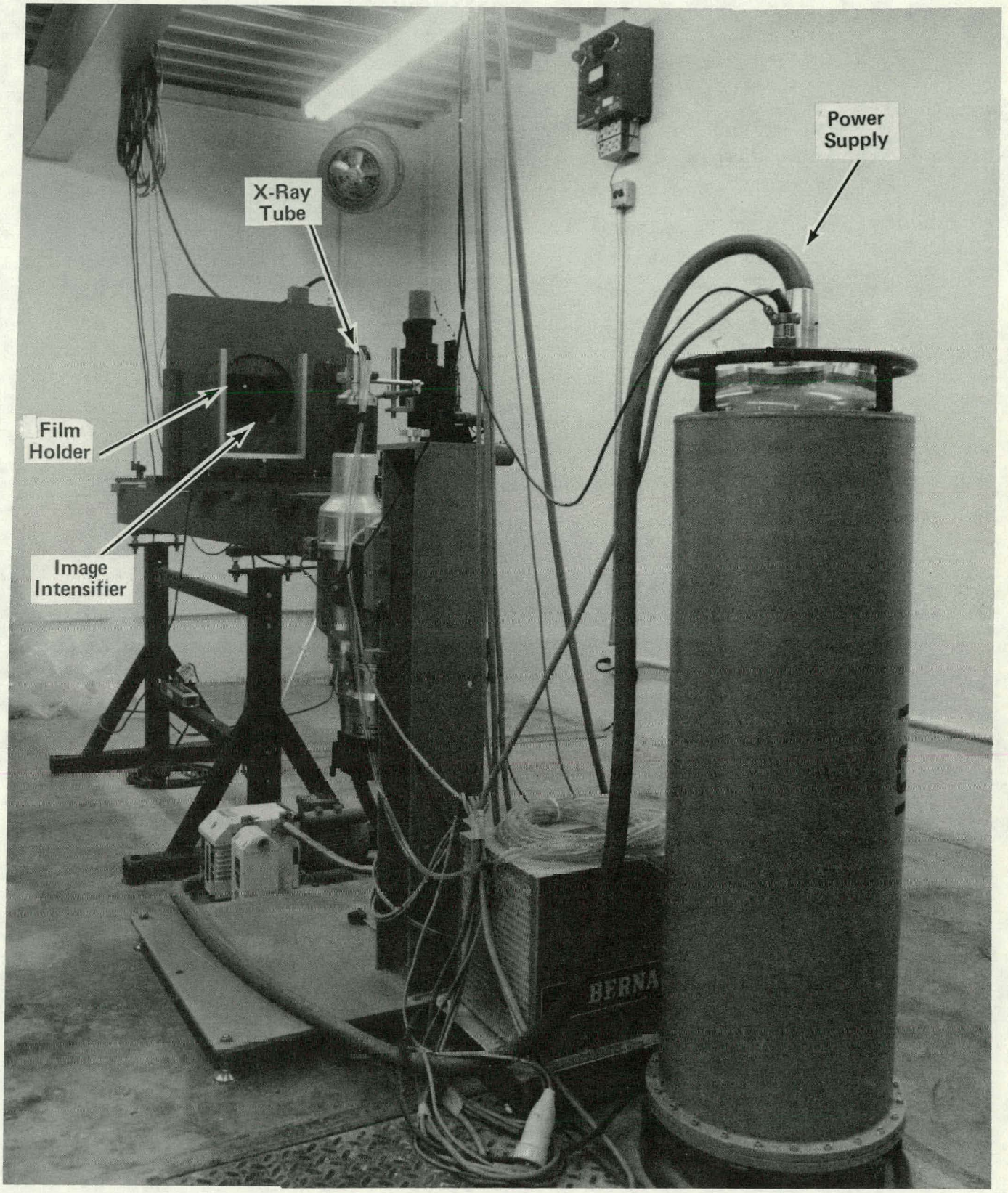

Figure 2-4. Microfocus X-Ray Room

The microfocus x-ray system can be used in two modes, real-time and film. In film radiography, the x-rays passing through the sample expose a sheet of film. The film imposes essentially no constraints on position resolution because the individual grains are microscopic, and long exposures allow great contrast sensitivity. However, the film must be exposed and developed before any results are available. Typically, several successive attempts are needed to get the proper exposure.

In real-time radiography, the film is replaced by an electronic unit which is essentially a fluorescent screen and a TV camera. This allows viewing the image on a monitor. The object may be remotely manipulated to find the best viewing angles, and results are available immediately. The limitations are in the spatial resolution of a TV image, the limited gray scale range, and the lack of long time exposure to suppress random noise.

Experience to date with the microfocus radiographic system has shown that real-time radiography and film radiography are not mutually exclusive. In fact, both types of radiographic detectors have been found to be essential in obtaining good quality images of defects in a reasonable time frame. Real-time radiography is an invaluable aid in specimen setup, making critical microfocus adjustments such as beam focusing, centering, and determining areas of interest when using high magnification. Both real-time and film images have been obtained for every specimen examined and both are considered necessary for the location and detection of defects in a reasonable time period.

As expected, the spatial resolution and contrast sensitivity using real-time radiographic methods are not as

good as that of film radiography. Using real-time radiography with digital image processing, the spatial resolution was on the order of 10 μm, while the percent contrast sensitivity was within the range of 3 to 4 percent for silicon carbide specimens having a nominal thickness of 6 mm. Therefore, film radiography is about a factor of three better than real-time radiography for the detection of defects in silicon carbide specimens. Film is also much more useful for precise location of defects prior to cutting the test samples described in Sections 4.2 and 5.4.

2.3.1.1 Radiographic Method

The majority of the silicon carbide specimens had a nominal thickness of 6 to 8 mm; however, several specimens were examined that had a thickness of about 14 mm. The operating parameters for the microfocus X-Ray system were 60-80 kV with a beam current of 0.3 to 0.5 mA. The source-to-film distance was 635 mm. The exposure times varied from five to ten minutes to obtain a film density of 2.4 to 3.2. Film density is the negative logorithm of light transmission. A density of 2 lets 10^{-2}, or 1 percent, of light to pass through. A projection radiographic technique with magnification factors of 2x to 10x was used to examine the silicon carbide (SiC) specimens.

For image standardization and quality indication, most exposures were made using an ASTM #5 Aluminum Penetrameter. In addition, several exposures were made using a DIN 62 AL Penetrameter which consisted of several parallel aluminum wires having diameters in the range of 0.100 to 0.40 mm. Aluminum penetrameters were chosen because the radiation absorption properties of aluminum, at low energy, are similar to those of silicon carbide.

2.3.2 Scanning Laser Acoustic Microscope (SLAM)

The SLAM equipment is shown in Figure 2-5. Operation of the SLAM is illustrated in Figure 2-6. Specimens are located in the central area for scanning, and images are displayed on the various CRT screens. A keyboard allows labels to be superimposed on the images, which can be photographed or videotaped.

The system operates by passing continuous wave ultrasound through the specimen and onto a plastic mirror coverslip. The sound waves in the coverslip cause deflections of the reflective surface at amplitudes proportional to the amplitude of the incident sound amplitude at each point.

The coverslip is scanned by a laser beam in a raster pattern and the reflected beam is passed by a knife edge to a photodetector. The small displacements of the surface cause the beam angle to be slightly modulated, and the knife edge causes the photodetector output to be modulated near the ultrasonic frequency. There is a slight doppler frequency shift because the ultrasound and the laser beam are both sweeping along the coverslip. The photodetector signal is mixed and filtered to extract this frequency component and the result is converted to a video amplitude. The CRT sweep is synchronized with the laser sweep, and the result is that the CRT displays a map of the sound intensity transmitted by the specimen. Defects are recognized by their characteristic disruption of the sound waves.

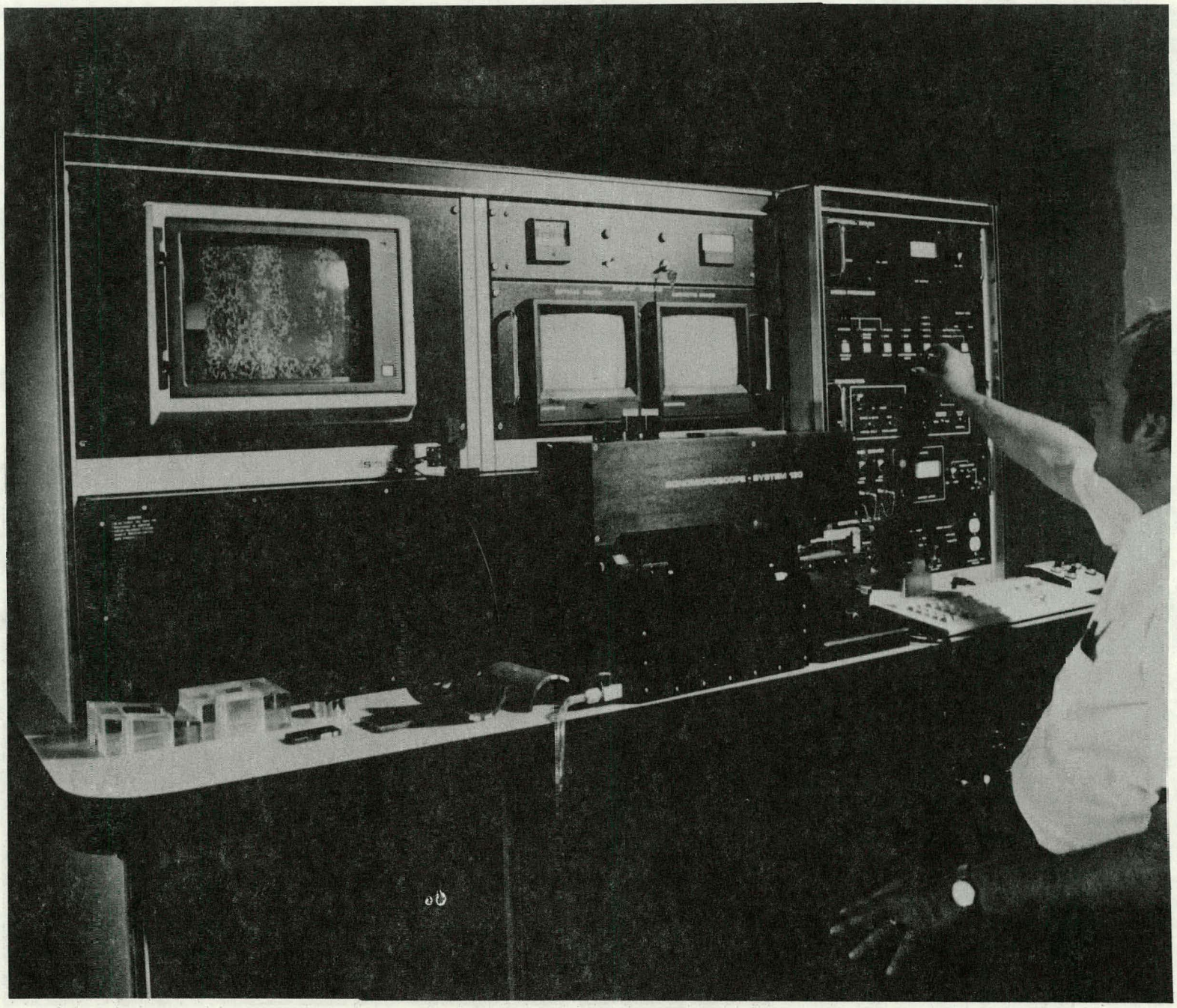

Figure 2-5. Scanning Laser Acoustic Microscope (SLAM)

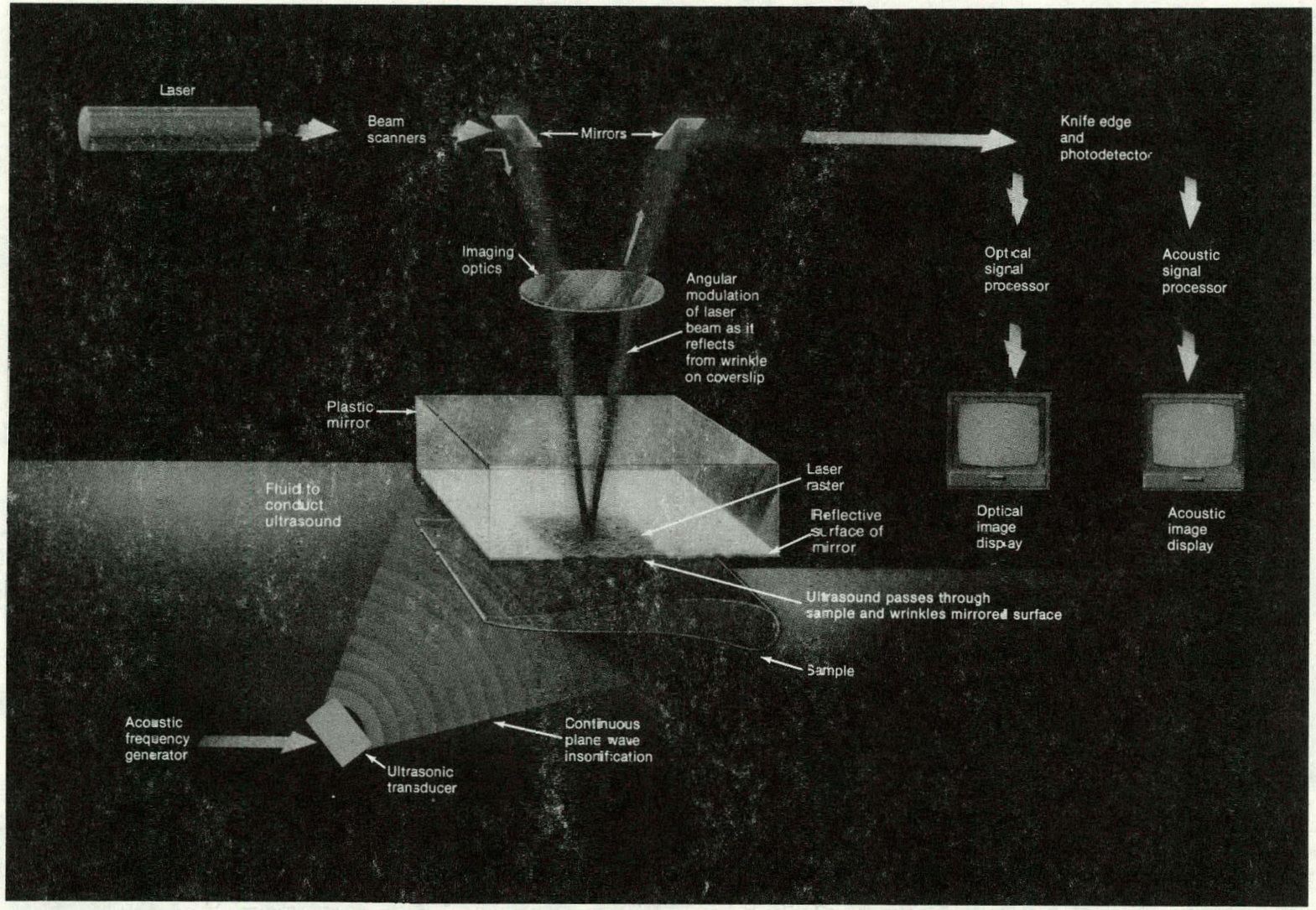

Figure 2-6. SLAM Functional Diagram

2.3.2.1 Penetration, Attenuation, and Scattering

In many ceramic materials, SLAM results are limited by strong absorption of the high frequency ultrasonic waves. This was investigated to determine operational limits for this program. Lack of penetration because of absorption is not a problem in silicon carbide, but scattering is. Based solely on impedance differences, one would expect reflection losses of about 8 dB for longitudinal waves and 6 dB for shear waves. However, at normal incidence (the longitudinal mode), standing wave patterns are set up and transmission loss is near zero, even at 90% density and 100 MHz, where we would expect greatest attenuation. At the other normal SLAM operating mode, 10° angle of incidence, the wave propagates through SiC as a 65° shear wave. At 100 MHz, the measured shear wave attenuation of specimens with polished surfaces are 17 dB (90% density), 20 dB (97%), and 28 dB (99%). These are exactly opposite the expected order.

It was expected that all three samples (about 0.6 cm thick for 90 and 99% densities and twice as thick for the 97%) would have essentially the same surface reflection losses, and the bulk losses should be proportional to the volume fraction of porosity. This should be true regardless of whether the sound is scattered or absorbed. After some experimentation, a probable cause of these anomolous measurements was discovered.

The measured loss at 90% density may correspond to the results expected from this model, 6 dB at each of two interfaces and another 5 dB over 1.4 cm path length. In the other two densities, the dominant effect is the multiple internal reflections and scattering that fills the test specimen with standing waves of ultrasound.

In most material samples, the size of the ultrasonic beam is clearly defined. The transducer is about the size of the laser scan pattern, and if the two are not aligned properly, there is a clear boundary between the areas insonified and those outside the sound beam. In the high density SiC samples, this is not the case. In the 99% dense samples, there is no trace of the boundary in the forward reflecting direction, and even in the backward direction, there is no significant loss of intensity. The 65° shear wave simply runs back and forth from end to end of the sample. The apparent loss at the center of the beam is the result of interference from waves making multiple round trips the length of the sample. In the transverse directions, where ray theory predicts no sound at all, there is a gradual loss of intensity. It any part of the sample is receiving ultrasound, it can be found coming from any other part.

2.3.2.2 Resolution

The resolution is limited by ultrasonic wavelength and the laser beam spot size. At 100 MHz, the spot size is 22 micrometers; at 30 MHz, it is 85 μm. The wavelengths in SiC are: 100 Mhz, 125 microns longitudinal and 78 microns shear; 30 MHz, 420 microns longitudinal and 260 microns shear. These numbers give minimum sizes for resolution of structure. Minimum detectable size is considerably smaller, given the right conditions.

2.3.3 Conventional Ultrasonic Equipment

Several different assemblies of laboratory equipment were used for ultrasonic examination of silicon carbide samples. These assemblies are discussed below and shown in the attached block diagrams. Two techniques were established

for wall thickness measurement and one for a compression wave bulk flaw measurement. In addition to the techniques investigated by B&W, the Idaho National Engineering Laboratory (INEL) examined selected samples using a pulse echo acoustic microscopy technique which utilizes acoustic time-of-flight measurements for imaging.

2.3.3.1 Thickness Measurement by Ultrasonic Resonance

Standard laboratory measurement techniques such as pulse overlap are available for measuring thickness or velocity. However, for small thicknesses, the standard pulse-overlap technique requires a very short pulse duration because of the high velocity. This requires a very high frequency, but sample surfaces limit the use of high frequencies. To overcome this, a resonance technique was developed and used for thickness measurement, using the equipment shown in Figure 2-7.

A counter monitors the frequency of a continuous wave oscillator, the output of which drives a transducer after amplification in a gated amplifier. The gated amplifier produces a tone burst of sufficient length to allow a standing wave to develop in the sample. The pulse reflected from the sample is amplified in a broadband receiver and monitored on an oscilloscope.

At the start of each pulse, the reflection coefficient at the front of the sample is dependent only upon the characteristic impedances of water and silicon carbide. When a standing wave has developed, the reflection coefficient is based on the characteristic impedance of water, and the input impedance of silicon carbide which can range from the characteristic impedance of water to well above the impedance of silicon carbide, depending upon the sample thickness in wavelengths.

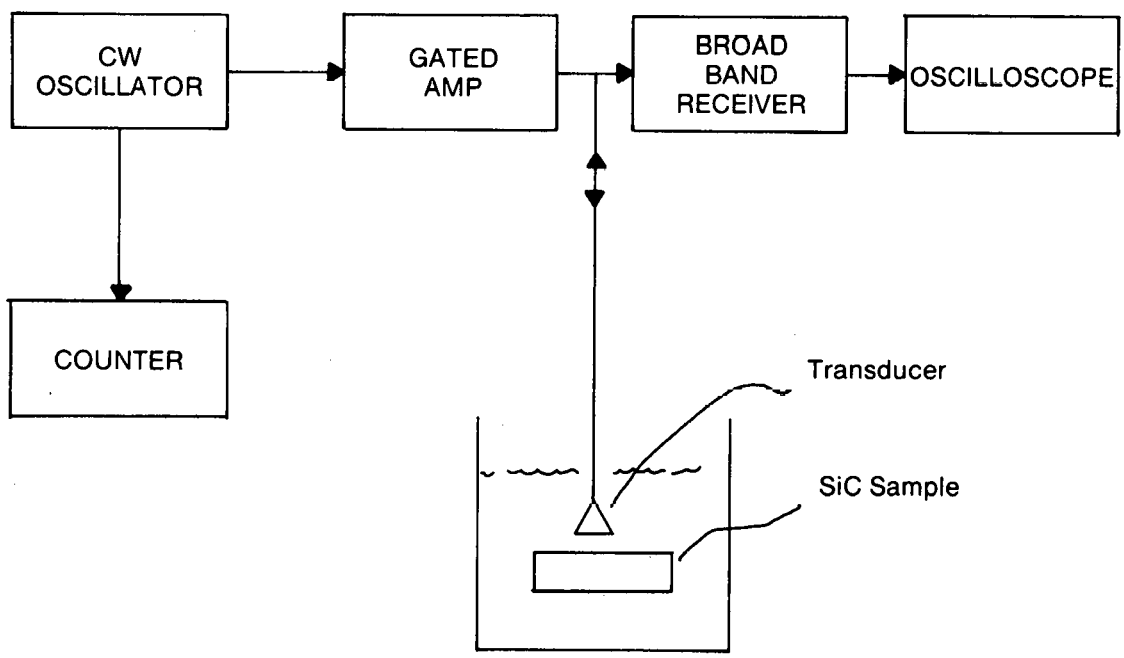

Figure 2-7. Resonance Thickness Measurement System

By slowly tuning the oscillator through a range of frequencies, a number of resonant frequencies, at which the thickness is a multiple of a half wavelength, can be selected using the minimum amplitude in the center of the pulse as an indicator.

A nominal 10 MHz transducer, 3/8 inch diameter, gave good results between 7 and 13 MHz. The difference in frequencies of the first and last minima were divided by the number of peaks between to get the frequency step. The various minimum amplitude frequencies were divided by this step and, as expected, produced a series of integers. In the tube sample, the frequency step was close to 1 MHz.

2.3.3.2 Thickness Measurement Using Spectrum Analysis

In a second thickness measurement technique (Figure 2-8), a spectrum analyzer was used to determine the resonant frequencies. The gate in the pulser/receiver did not sufficiently reduce the initial pulse, so a gate pulse generator with adjustable delay and gate width was used. The gate activated an HP double balanced mixer which then passed the double gated RF pulse from the receiver to the spectrum analyzer. Broadband pulses were sent to and received from the transducer. The received pulses contained information on sample resonant frequencies which were displayed as a series of minima in the amplitude spectrum.

The transducer used was 10 MHz, 3/8 inch diameter, 1.625 inch focal length. The spectrum analyzer used was an HP3585A, which stores data digitally and allows moving a cursor for digital readout of frequencies. Minima were clearly readable beyond 30 MHz.

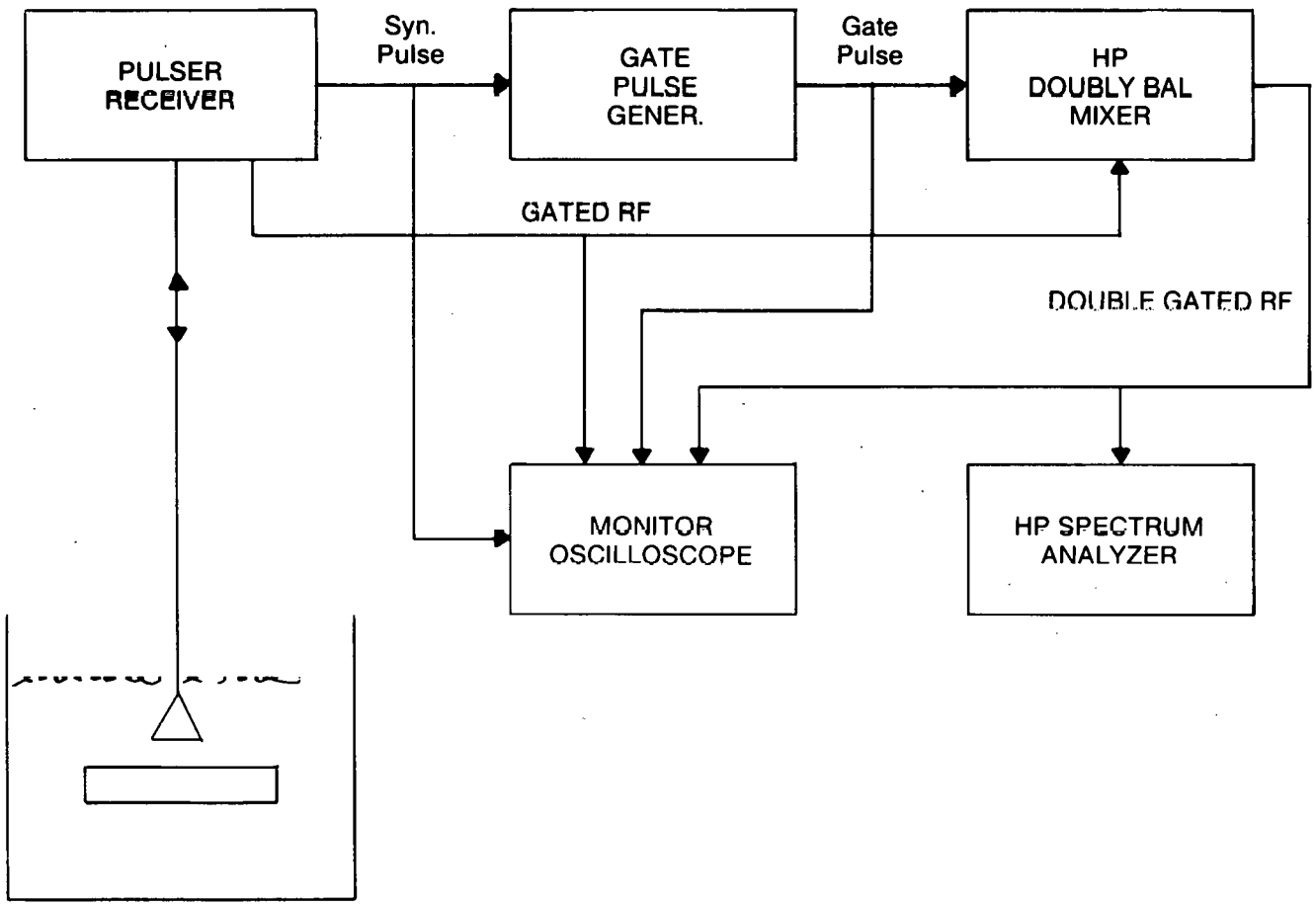

Figure 2-8. Spectral Analysis Thickness Measurement System

2.3.3.3 C-Scan Examination of Samples

The electronic circuitry used for C-scan recording is shown in Figure 2-9. A Panametrics 5600 was used to excite a 50 MHz, 1/4 inch diameter, 2-inch focal length transducer.

This transducer was scanned over the sample surface, and a gated echo was extracted from the receiver before being amplified in an HP8447F broadband amplifier. This echo signal was then peak detected using a peak detector designed and built by B&W. This signal was sent to a Metrotek MA601 gated alarm. The gated alarm incorporated a threshold control so that the output would switch from low to high when the input crossed the threshold. The output of the gated alarm activated the plotter which is part of the scanning system.

2.3.3.4 INEL Time-of-Flight Acoustic Microscopy

The instrumentation for the INEL time-of-flight system is based on Nuclear Instrumentation Module (NIM) and Computer Automated Measurement And Control (CAMAC) and uses both commercial and INEL built components. A logic diagram of the system is provided as Figure 2-10. The generation and detection of the acoustic signals are accomplished using a Panametrics 5626 pulser receiver and a Panametrics spherically focused 50 MHz transducer with an 11.2 mm diameter element and a 56 mm focal length. Signal processing and system control are performed by a DEC LSI 11/73 computer.

C-scan images are produced by scanning the transducer over the surface of the sample and recording the round trip transit time (time-of-flight) of the reflected acoustic wave. During scanning, the arrival times of the acoustic waves are compared to a simple set of conditions derived from a defect

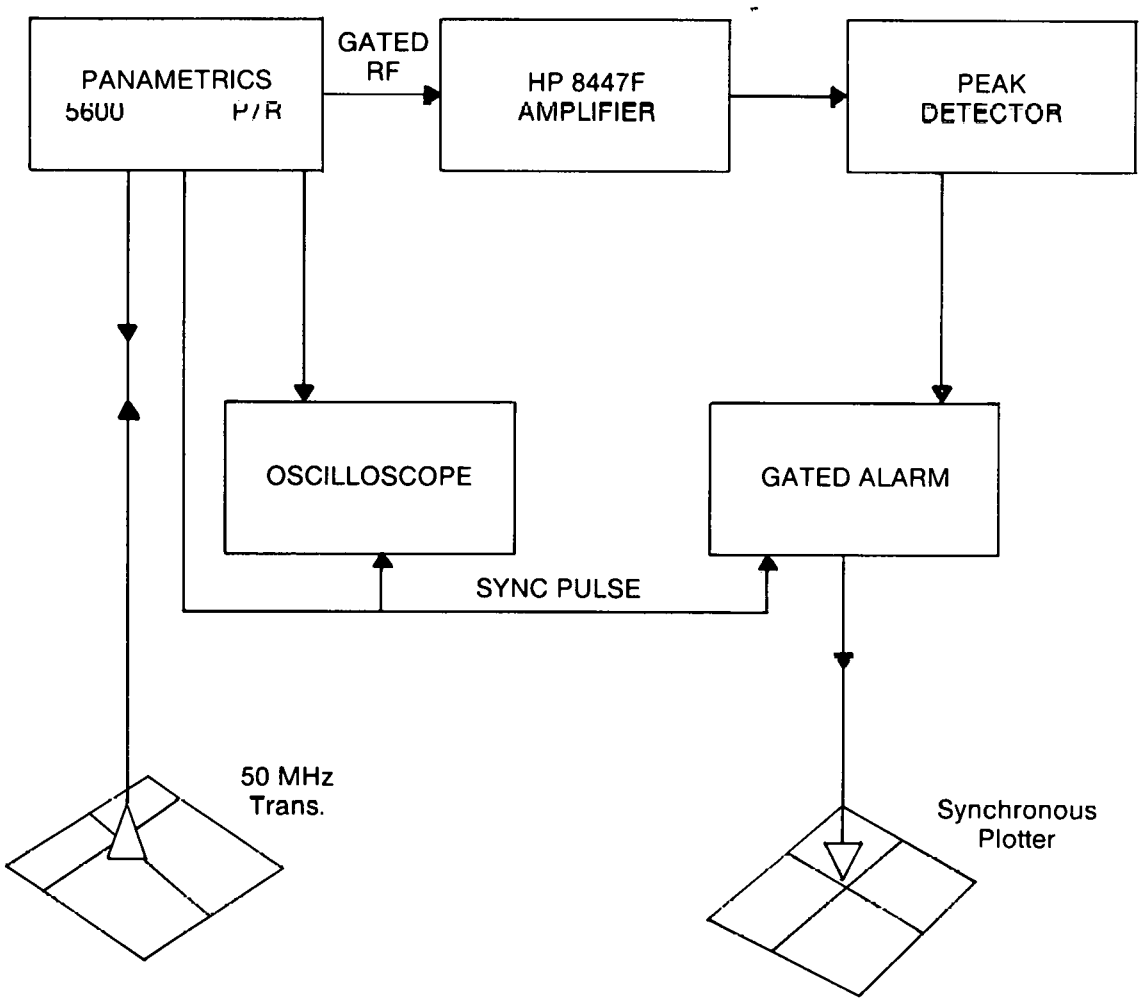

Figure 2-9. Ultrasonic C-Scan System

Time of Flight Acoustic Microscope

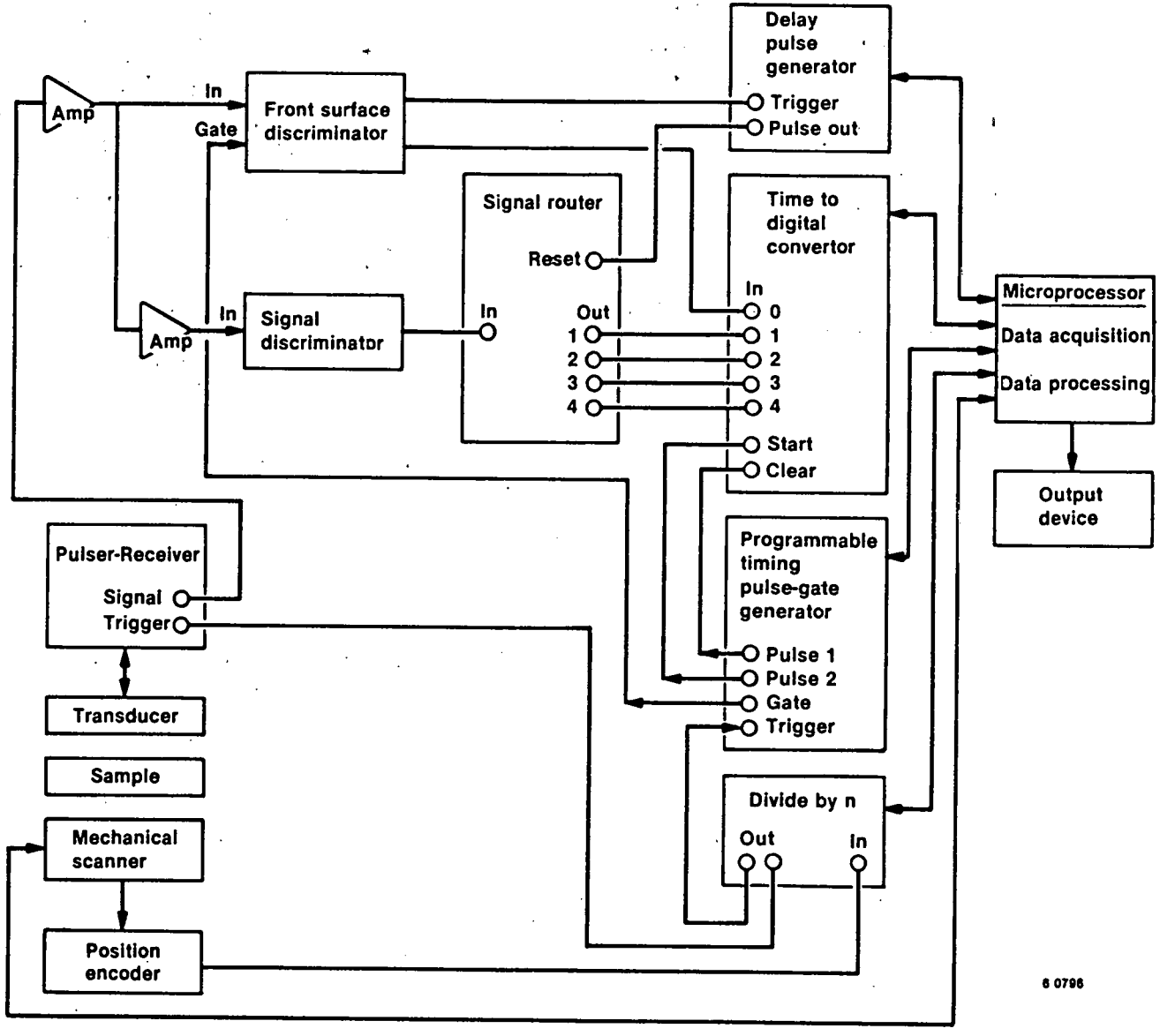

Figure 2-10. Time of Flight Acoustic Microscope

free sample. All deviations detected are considered to be defects and imaged. The standard form of output for this system is color coded to distinguish either the type of defect or the time interval in which it is detected. Given the velocity of the material being examined, arrival times of the reflected signals can be directly related to depth in the material. Typically, the transit times for acoustic waves reflected from the interior of the test piece are divided into five equal intervals whose size and location are determined during the initial setup. With the proper setup parameters, the same system can be used to acquire maps of surface irregularities, bulk flaws, and transit times which can be used to measure changes in acoustic velocity, provided dimensional changes are taken into account. A LeCroy 2228A TDC was modified to obtain full scale time ranges of 1.0, 2.0, and 5.0 μs and then used to digitize the arrival times of the reflected acoustic waves. Eleven bit (2048) resolution is obtained independent of range yielding minimum achievable time periods of 0.5, 1.0, and 2.5 ns corresponding to 0.006, 0.012, 0.030 mm of silicon carbide, respectively. Depth measurements on the order of magnitude of these dimensions can be made provided the material remains isotropic. The advantage of the time-of-flight method over conventional digital methods is that signal processing is minimized for each scan point. Therefore, the scan can proceed at a fast rate and the flaws can be displayed in real time. With the present system, a maximum theoretical scan rate of 2800 data points/second can be obtained. In actual practice, this scan rate is reduced by the limitations of the mechanical scanning mechanism and of the 9600 baud output device used to physically display the data collected. As constructed, the system is capable of scanning an 89.0 mm OD tube, 2.44 m long in 68 minutes using 0.2 mm axial and 0.3 mm circumferential increments.

2.3.4 Acoustic Holography

Acoustic holography techniques have been used at B&W since 1973, primarily to image and size defects which were located within thick-section steel components such as nuclear pressure vessels and pressurizers. The techniques make use of the phase and amplitude of ultrasonic echoes returned from the defect. The phase information is related to the time for the ultrasound to travel from the transducer to the defect and back to the transducer, a pulse echo technique. Acoustic holography requires the sampling of one data value at each scanned array position; each value is a measurement of the sum of contributions from the entire defect, and the reconstruction process effectively sorts them out to determine the original defect's shape and size.

In order to use holographic techniques on the SiC materials of interest in this study, the frequency range of the signal processor and electronics was extended to greater than 50 MHz. This was necessary because of the small defect sizes of concern, on the order of a few thousandths of an inch. These efforts are described in the next few paragraphs, followed by some preliminary results.

2.3.4.1 Technique Development

The useful frequency range for thick-section metal components is typically 1 to 5 MHz. Above 5 MHz attenuation becomes severe, especially for stainless steel clad samples. These frequencies generate ultrasonic wavelengths of 6 mm for 1 MHz longitudinal waves down to 0.64 mm for 5 MHz transverse (shear) waves. These wavelengths are generally sufficient to resolve the details of significant defects in steels.

Higher frequencies are required for detecting and characterizing the small defects of concern in ceramic heat exchanger tubes. Therefore, efforts were made to extend the frequency range at which holographic techniques can be used.

To aid in development of holography at 10 to 50 MHz, a series of 0.4 mm diameter holes were drilled parallel to the surface of a zircaloy plate, within 0.25 mm of the surface as shown in Figure 2-11.

The holes were scanned using 10 and 25 MHz focused transducers to obtain acoustic holograms. The images were then reconstructed and two are shown in Figure 2-12. Note that these holes are in a fairly ideal piece of material - smooth, flat surface and ultrasonically clean. The 6.75 MHz image is generally pretty good although the defect is about the same as the ultrasonic wavelength - 0.34 mm.

The 25 MHz transducer images are not quite as good as the 10 MHz transducer images. This is mainly because the scanner does not have fine enough step resolution for this frequency. The so-called Nyquist limit requires that a waveform be sampled at least twice the highest frequency to prevent aliasing. This criterion cannot be met without a very high precision scanner - at least 0.0125 mm. The undersampling of the phase data caused the smearing in the 31 MHz image at the top of Figure 2-12.

Multiple holograms were made of all the holes. Sizing results were good at or below 10 MHz. Lengths and throughwall dimensions (diameter) agreed fairly well in most cases, with no dimensional errors greater than 0.15 mm diameter and 1.0 mm length, which is expected at these lower frequencies.

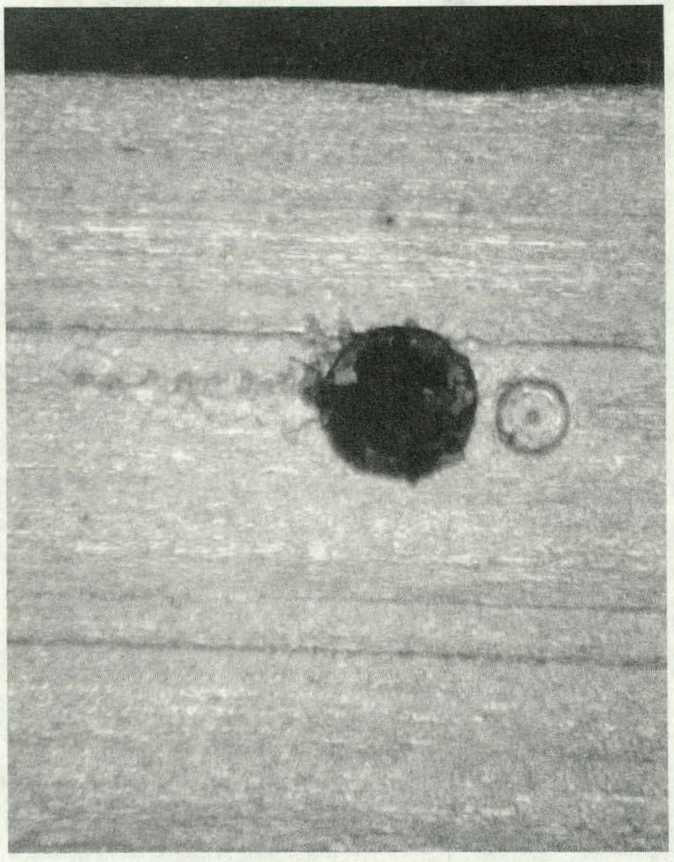

Figure 2-11. Side Drilled Hole in Zircaloy Plate (50X)

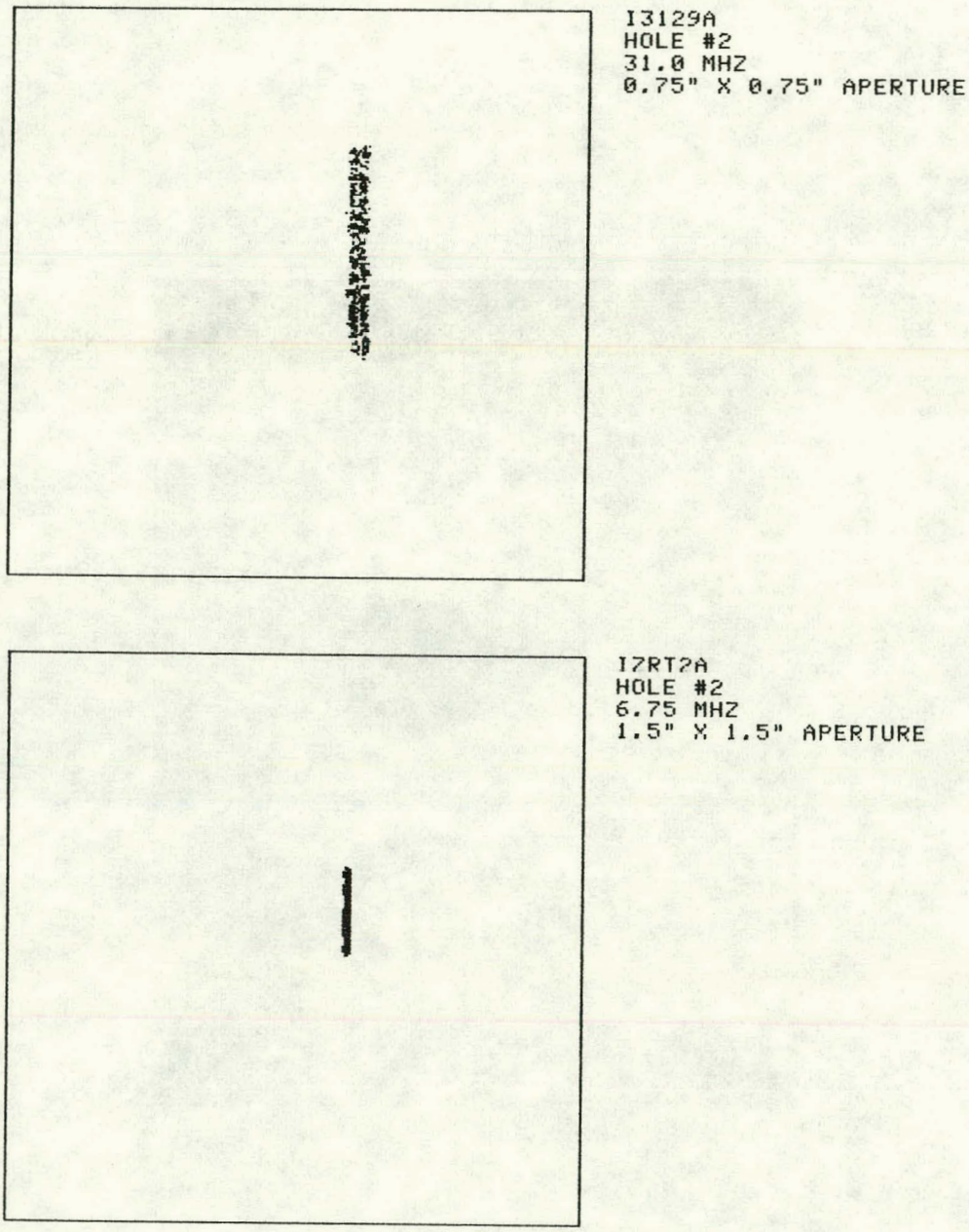

Figure 2-12. Image of Hole #2 at 6.75 MHz and 31.0 MHz

2.3.4.2 Experimental System

The signal generation and processing equipment required for these tests is based upon a B&W design produced at the Lynchburg Research Center. This design was, in turn, based upon the Holosonics 200 system, acquired in 1973, which was highly modified based upon B&W field experience.

The acoustic holography technique which is followed at B&W relies upon driving the transducer with a coherent burst of energy (sine wave) rather than pulse excitation which is typically used in ultrasonic detection systems. The high frequency signal is obtained from a Tektronix SG702 leveled sine oscillator. This signal serves as the reference signal, a portion of which is gated out, then amplified to drive the transducer. The return echo from a defect is also sinusoidal, at the same frequency as the reference. This return echo signal is amplified and fed to one side of a double balanced mixer. The reference signal is fed to the mixer as well, and the output of this device is the phase signal.

The phase signal is directly related to the distance from the transducer to the defect and also the amplitude of the return echo signal. The outcome of raster scanning the transducer while sampling the phase data is an amplitude modulated, phase only hologram. This hologram is processed to reconstruct an image of the defect. The reconstruction process effectively determines what kind of object (defect) exists within the part that could have caused the observed hologram.

A system block diagram of the Acoustic Holography System is shown in Figure 2-13.

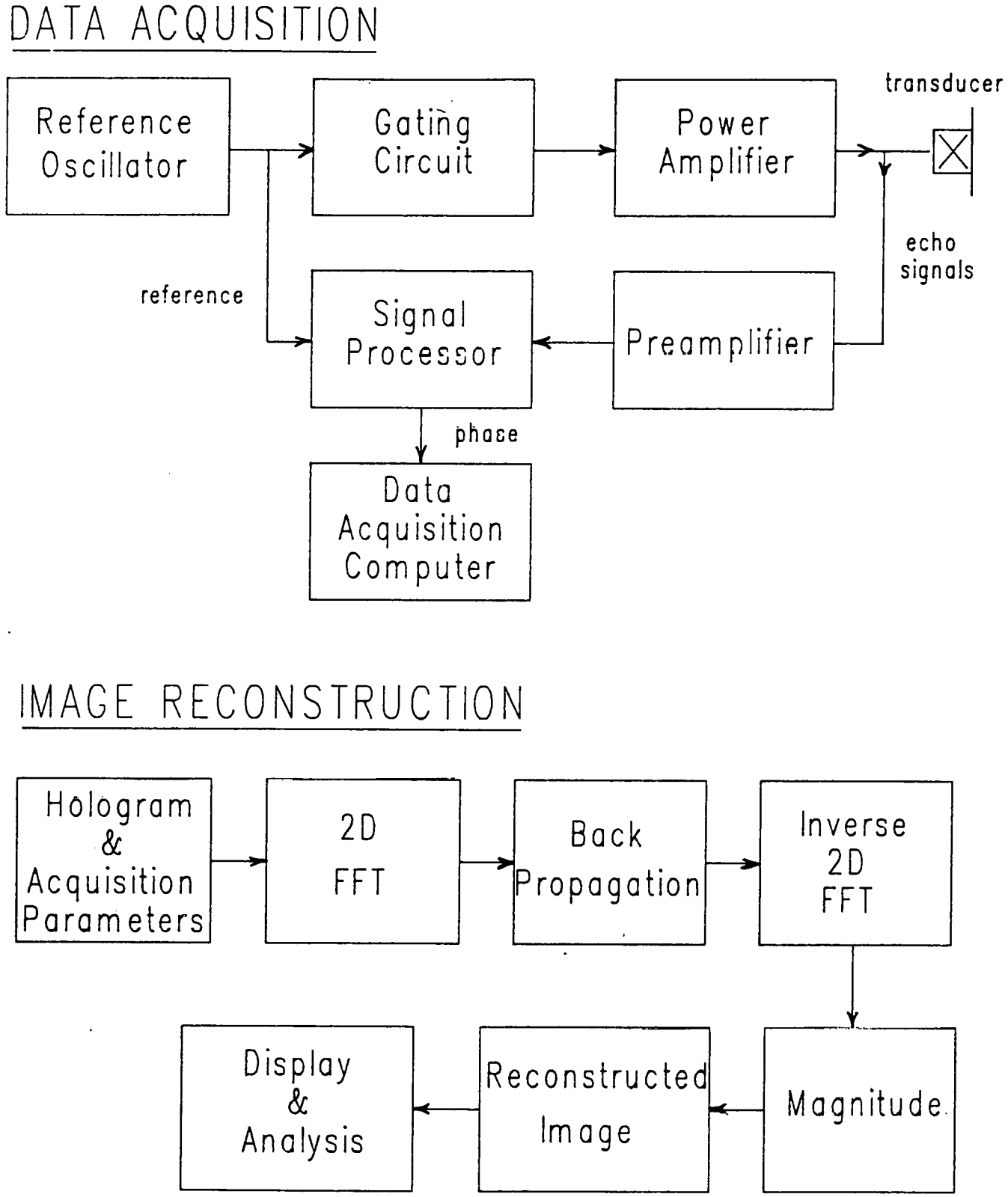

Figure 2-13. Block Diagram of Acoustic Holography System

2.3.4.3 Results

A number of samples, which exhibited the largest responses to conventional UT, were examined using the acoustic holography technique. For example, sample 759 was examined using a 25 MHz, 25 mm focal length transducer. The wires were barely detectable at this frequency, and the signal levels too low to produce useful results. The same was true of all other samples. For this reason, no results on Acoustic Holography are presented in Sections 3 or 5. The equipment was not adequate to the task.

2.4 TECHNIQUE IMPROVEMENT POTENTIALS

One potential improvement that would benefit all the methodologies is the development of manipulators to allow scanning of entire tubes and location of specific points on a tube by an indexing system.

The microfocus X-Ray system can be improved by adding CAT scanning capability. The combination of microfocus resolution and magnification with computed tomography's cross-sectional imaging would greatly improve the evaluation of defects.

The SLAM can be improved by adding an acoustic holographic capability. The attempt to use holography in this program failed because of scanning resolution problems and signal strength problems; therefore, holography will not be further addressed in this program. However, the SLAM has an operating mode in which the received signal is mixed with a reference oscillator. The resulting display looks like, and is mathematically equivalent to, an acoustic hologram.

This holographic image could be digitized by a video "frame grabber" and transferred to a computer for reconstruction by existing algorithms. Scanning precision is resolved by choosing a regular array of pixels from the image and low signal strength is corrected by the SLAM's higher power transducer and frame averaging, which reduces the random noise in weak signals.

Section 3
NONDESTRUCTIVE EXAMINATION (NDE) OF SEEDED AND UNSEEDED SPECIMENS

3.1 INTRODUCTION

Twenty-three silicon carbide specimens were produced for NDE testing. Twelve were hot pressed flat plates and nine were sections of a recuperator tube. Two more were made from a cut and polished plate. Samples were classified as shown below.

Classification of Samples

I. Samples with Seeded Defects

   A. Cylindrical Defects

   B. Spherical Defects

   C. Samples with Mechanically Induced Surface Defects

II. Samples without Seeded Defects

   A. High Porosity Samples

   B. Medium Porosity Samples

   C. Low Porosity Samples

A listing of the samples and the methods used in their preparation is given in the next two subsections.

3.2 SEEDED FLAW FABRICATION

The specimens prepared for NDE testing are summarized in Table 3-1. All samples were hot pressed from a powder designated Mix 37 which consisted of 96.4% Lonza UF-15 silicon carbide powder, 2.9% Varcum phenolic resin, and 0.7% boron carbide powder. Nondestructive testing of the seeded flaw samples is described in Section 3.9. Destructive sectioning is described in Section 4.3.

3.2.1 Cylindrical Defects

Sample 571 was a hot pressed plate with dimensions 6.6 cm x 6.6 cm x 0.6 cm. It contained two carbon fibers and two alumina fibers lying parallel to one another approximately in the mid-plane of the plate. All fibers were approximately 4 cm long. Two-thirds of the length of each fiber was parallel to the large surfaces of the plate and the remaining 1/3 was inclined slightly toward one large surface. The carbon fibers were 12 μm in diameter and the alumina fibers were 10 μm in diameter.

In order to produce the sample, one-half of the silicon carbide powder was lightly pressed to form a compact. Two-thirds of the upper surface of the compact was parallel to the lower surface. The remaining surface was inclined away from the lower surface. The fibers were then placed on the compact and covered with the remaining silicon carbide powder. The compact was then hot pressed to form the sample.

Sample 759 was manufactured by the same technique used to make sample 571. However, in this sample were three 4 cm long metal wires. The entire length of each wire was parallel to the large surfaces of the sample. The wires were:

Table 3-1

Summary of NDE Samples

Hot Pressed Plates, 6.6 cm x 6.6 cm x 0.6 cm

571	carbon and alumina fibers
759	platinum and tungsten/rhenium wires
570	graphite particles
763	platinum particles
564	90% dense
566	91.5% dense
534	97% dense, double thickness, cut and polished to study porosity
567	98% dense
568	97.6% dense
528	99+% dense, double thickness
563	99+% dense, cut and polished for Knoop indents
565	99+% dense

Samples Cut from Tube

D1-D4	14 cm tubes, cut lengthwise, with EDM notches
D5	flange section
D6	closed end of tube
D7	stepped wall thickness

0.5 mm diameter platinum, 0.3 mm diameter platinum, and 0.25 mm diameter tungsten/25% rhenium.

3.2.2 Spherical Defects

Sample 570 was a hot pressed plate of 98.8% Theoretical Density (T.D.). It was made with four spherical graphite particles embedded in the mid-plane of the plate along a straight line. Particle sizes are shown below, stated as a range rather than as an exact size since the size was determined by sieve analysis.

Size of Spherical Graphite Particles

1. 707-841 μm
2. 250-297 μm
3. 74-105 μm
4. less than 37 μm

Half of the powder used to make the sample was lightly pressed into a compact. The four graphite particles were then pressed into the compact and covered with the remaining powder. The complete assembly was then hot pressed.

Sample 763 was a hot pressed plate at 96.5% T.D. It contained platinum particles approximately in the mid-plane of the sample. This sample was manufactured in the same manner as sample 570.

Platinum spheres were made by melting the end of a platinum wire in an oxy-acetylene flame so that a molten bead

formed on the end of the wire. After repeated attempts, four beads were obtained. The diameter of each of the beads, determined with an optical comparator, are listed below.

Size of Platinum Particles

1. .40 mm
2. .65 mm
3. 1.40 mm
4. 1.90 mm

3.2.3 Samples with Mechanically Induced Surface Flaws

Sample 563, a low porosity sample, was cut in half to produce samples 563A and 563B. These samples were approximately 6.6 cm x 3.3 cm x 0.6 cm.

Sample 563A was ground so that the surfaces with largest dimensions were parallel. Three Knoop indents were placed in one surface, one indent each at loads of 27.6, 48.5, and 94.3 newtons. The opposing surface was polished with 9 micron diamond and indented with loads of 8.0, 10.2, 22.2, 23.1, and 29.4 newtons.

Sample 563B was ground and polished on both sides and had three Knoop indents placed in one surface, one each at 45, 90, and 400 newtons.

3.2.4 Electrical Discharge Machining (EDM) Notches

EDM was used to simulate cracks. Four samples were made from two tubular sections taken from the straight portion of a silicon carbide recuperator tube. Both sections, which were approximately 14 cm long, were cut into two equal parts

parallel to the tube axis to form four sample blanks. Samples produced from the blanks were designated D1, D2, D3, and D4.

Sample D1 had five EDM notches on the convex (outer) surface, located along an imaginary line parallel to the tube axis. This line was centered in the blank and divided the sample into two equal parts. The five EDM notches had depths of 0.125, 0.25, 0.50, 0.75, and 1.25 mm. The length of each notch was three times the depth and the long dimension of each notch was parallel to the tube axis. An additional five notches were located on the convex surface along another imaginary line parallel to the tube axis. This line was located so as to divide the sample lengthwise into two parts, with one part twice as large as the other. The dimensions and orientations of these notches were identical to those of the other five notches.

Sample D2 had two sets of five EDM notches located on the concave (inner) surface. The dimensions and orientations of the notches were the same as for sample D1. The notches were also located along imaginary lines analogous to those in sample D1.

Sample D3 had five EDM notches located on the convex surface along an imaginary line parallel to the tube axis. This line divided the sample into two equal parts. The dimensions of the notches were the same as for the notches in sample D1. However, the long dimensions were oriented perpendicular to the tube axis.

Sample D4 had five EDM notches identical in dimensions, orientation, and location to the five notches in sample D3. Additionally, there were five notches located on the inner surface on an imaginary line parallel to the tube

axis. This line divided the sample into two parts with one part twice as large as the other. The dimensions and orientations of these notches were the same as those of the notches on the outer surface of the sample.

3.2.5 Samples with Different Geometries or Thicknesses

Sample D5 was a portion of the flange taken from the recuperator tube.

Sample D6 was the closed end of the recuperator tube.

Sample D7 was a stepped tube manufactured from a 7.5 cm long section taken from a commercially produced silicon carbide recuperator tube. The straight portion of the recuperator tube had an O.D. of approximately 8.9 cm and a wall thickness of about 0.6 cm. To produce sample D7, six shoulders, each 1.25 cm wide, were machined into the section. The O.D. of the shoulders ranged from 8.9 cm to 8.3 cm in 1.27 mm increments. Dimensional tolerance was plus or minus 0.127 mm.

3.3 SPECIMEN FABRICATION WITH POROSITY VARIATIONS

3.3.1 High Porosity Samples

Samples 564 and 566 were plates with dimensions 5.7 cm x 5.7 cm x 0.6 cm. They were hot pressed from the same silicon carbide based mixture used in the manufacture of all hot pressed specimens. The laboratory technique used to manufacture these samples was typical of the manufacturing procedure used.

The density of sample 564 was 89.8% T.D. and that of 566 was 91.5% T.D. The desired density was achieved by hot pressing a certain weight of powder, 110 gm, to a predetermined volume, rather than by using a specific hot pressing schedule. This appeared to give better control of final density.

3.3.2 Medium Porosity Samples

Samples 534, 567, and 568 were 5.7 cm x 5.7 cm square plates hot pressed from Mix 37. Sample 534 was 1.2 cm thick; the others were 0.6 cm. Densities were 97.0% T.D., 98.1% T.D., and 97.6% T.D., respectively.

A detailed analysis of specimen 534 was performed to evaluate density variations. Although the measured density was 97% of theoretical, the porosity distribution was uniquely inhomogeneous. Figure 3-1 gives a measure of the porosity variation across the specimen. Selected locations identified in the figure were subsequently evaluated for void diameter and population variations (Figures 3-2 to 3-6). The bulk of the porosity was approximately 2μ in diameter with significantly higher populations around positions #6 and #26 in the cross-section. The photographs are optical photomicrographs. The pore sizes and populations were determined by an optical analysis instrument at INEL.

3.3.3 Low Porosity Samples

Samples 528, 563, and 565 were 5.7 cm x 5.7 cm, hot pressed plates. 528 was 1.2 cm thick; the others were 0.6 cm. All three samples had densities of 99.0% T.D. or greater.

3.4 MATERIAL ROUGHNESS AND GEOMETRY VARIATIONS

Roughness and geometry variations are a major source of difficulty in tube inspection. Figure 3-7 shows sections of a full tube, giving a close view of surface conditions.

Roughness was measured on hot pressed samples and on the outside surface of tube material, using an instrument with a 0.025 mm radius diamond stylus. The results, shown in Figure 3-8, are consistent with visual inspection. The tube is smooth over the large scale with very fine roughness. The hot pressed specimens are smooth on the fine scale, with large scale uneven surfaces.

The inner surface of the tube is much worse than the outer surface, as can be seen in Figure 3-7. It could not be measured with the gauge because of the curvature of the surface.

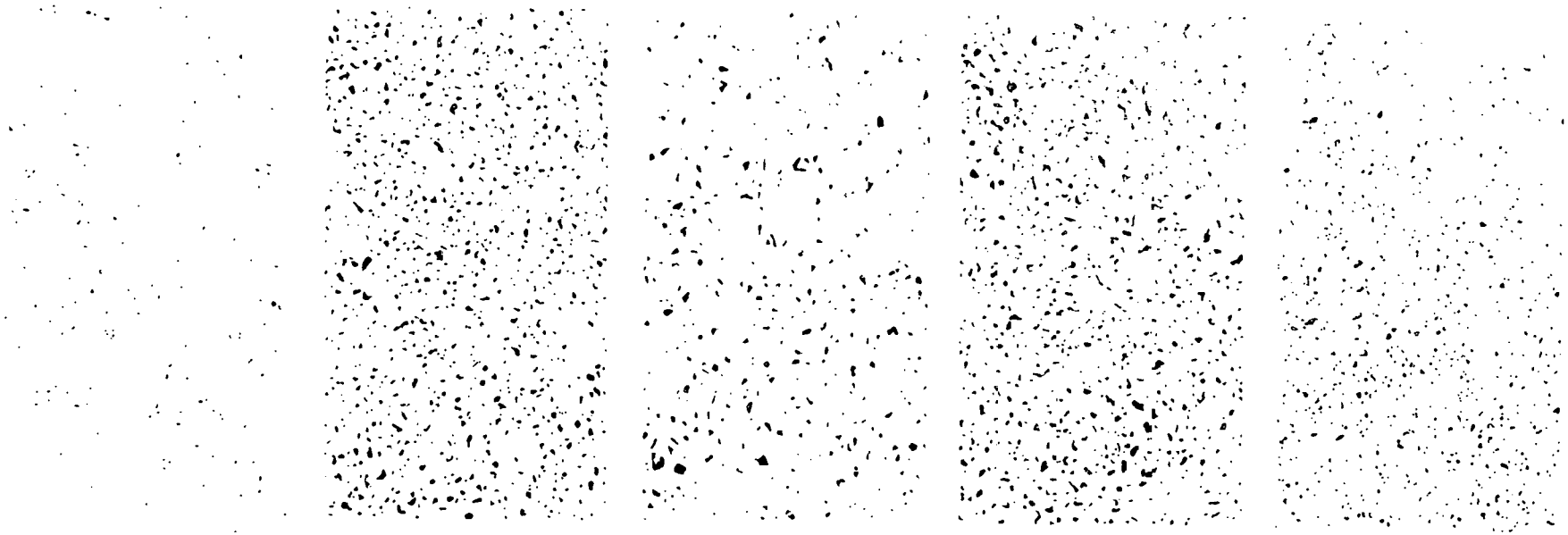

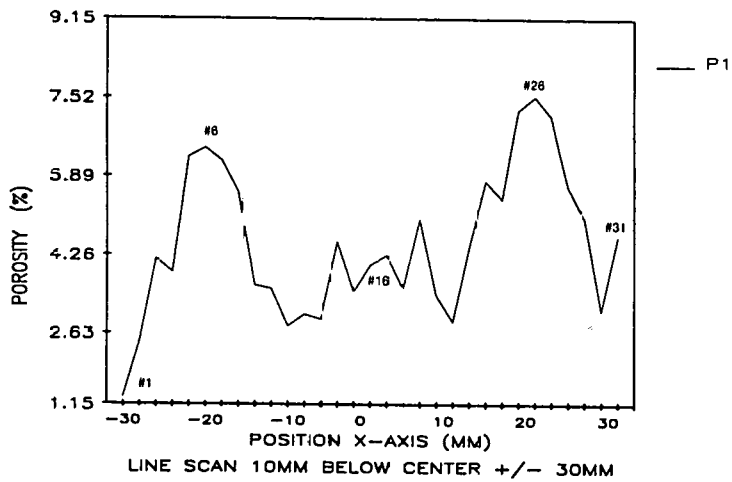

Figure 3-1. Measured Porosity of SiC Ceramic, Sample 534

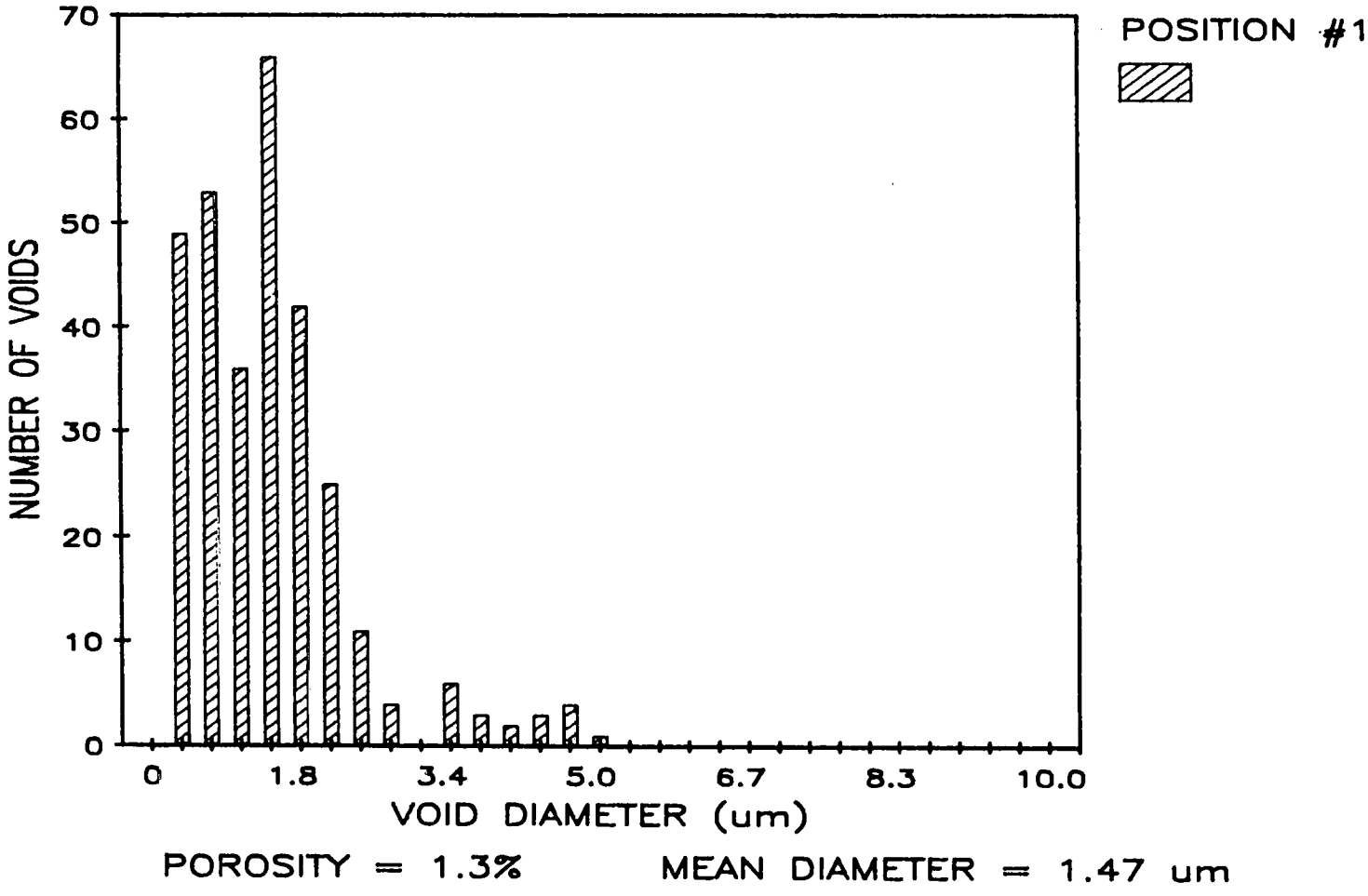

Figure 3-2. Void Size Distribution, SiC Ceramic, Position #1, Sample 534

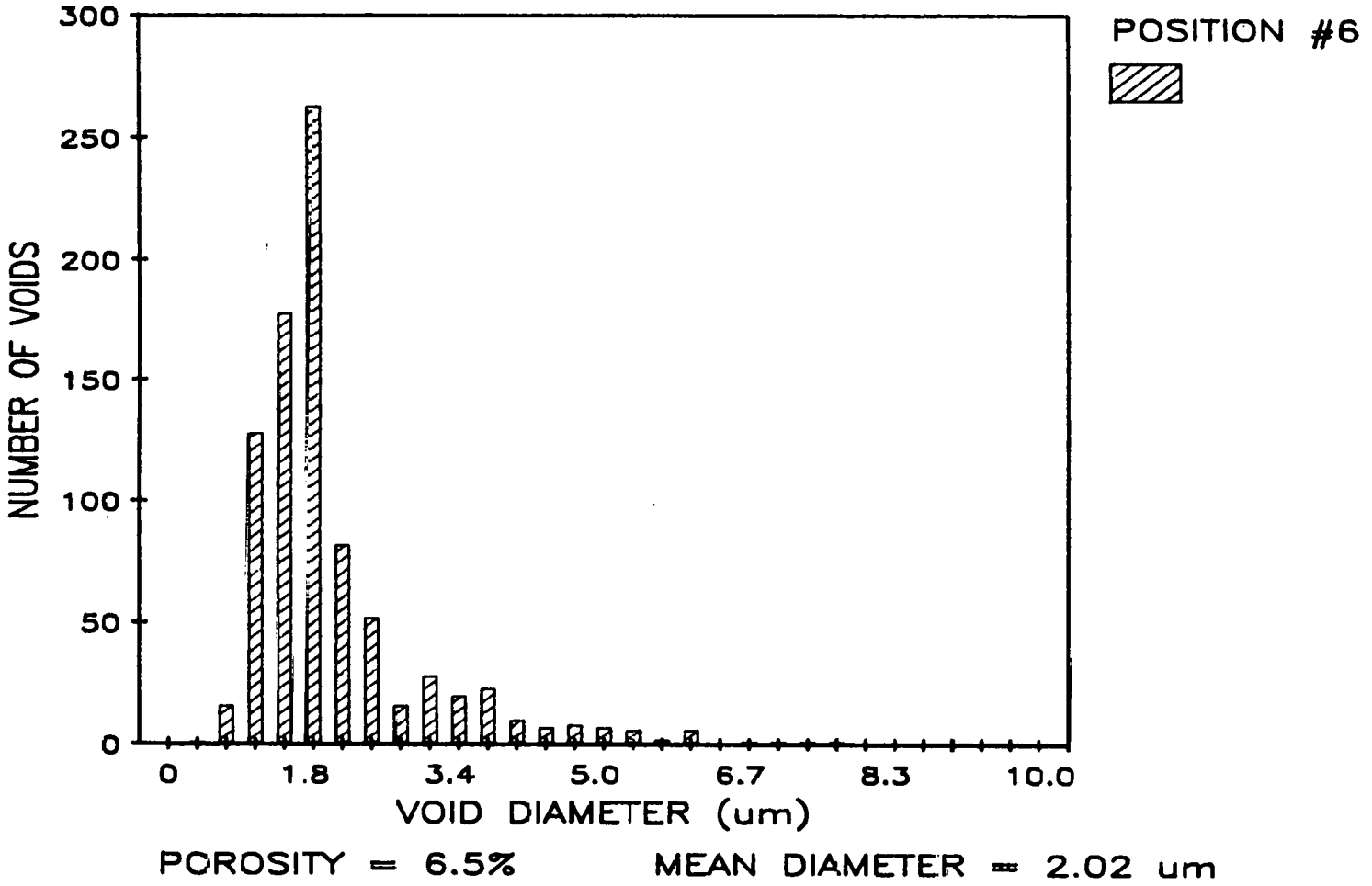

Figure 3-3. Vcid Size Distribution, SiC Ceramic, Position #6, Sample 534

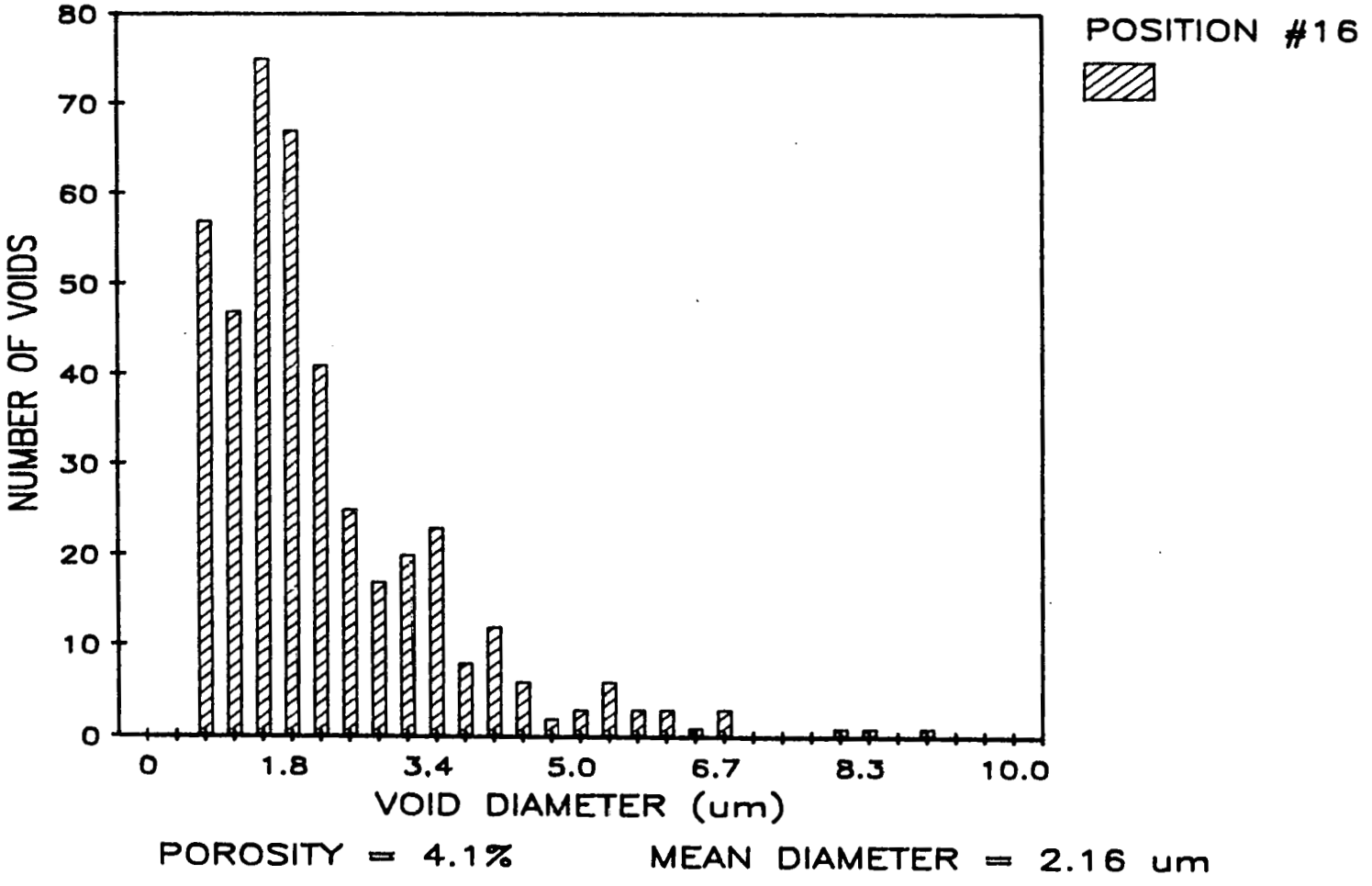

Figure 3-4. Void Size Distribution, SiC Ceramic, Position #16, Sample 534

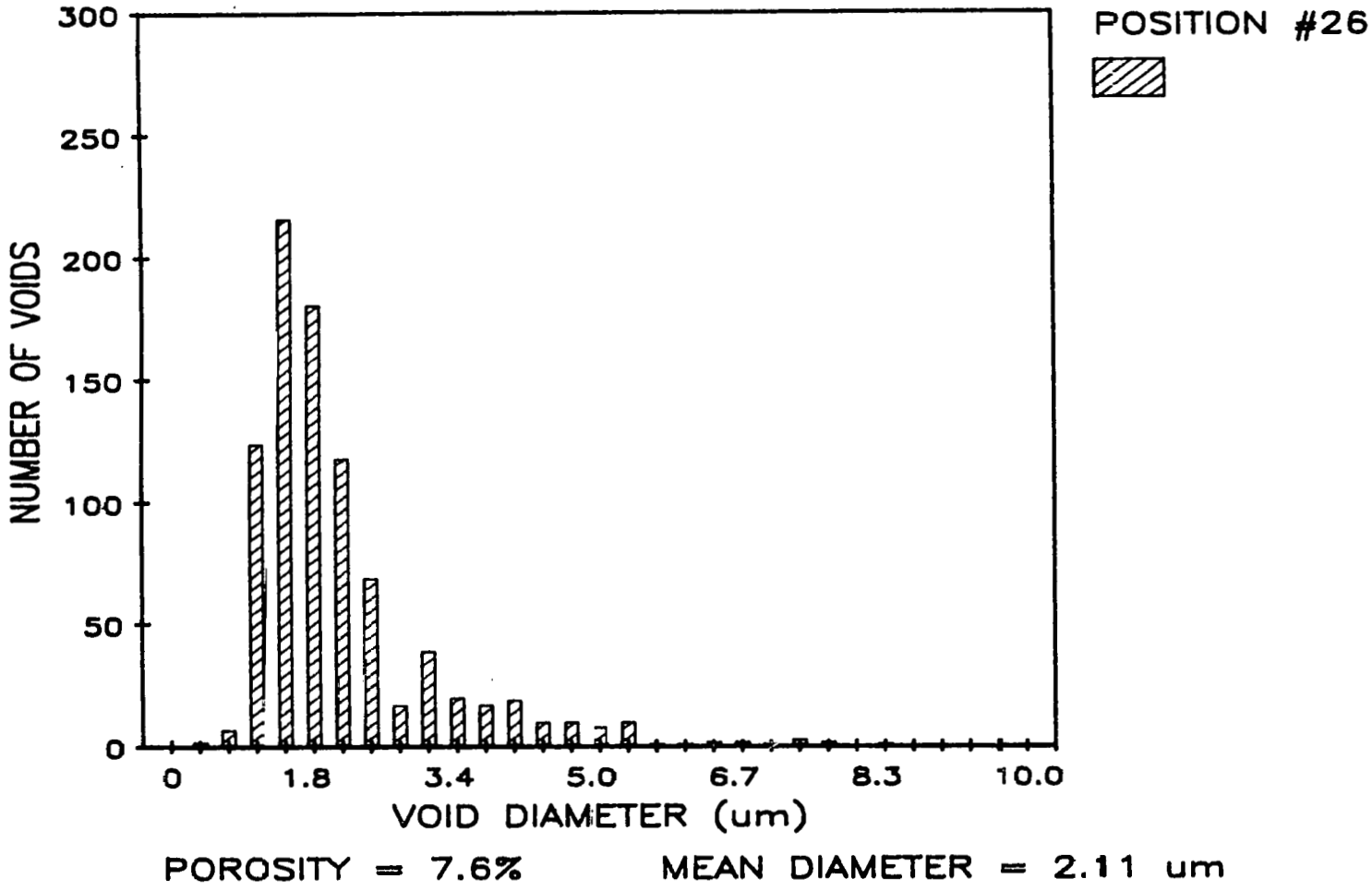

Figure 3-5. Void Size Distribution, SiC Ceramic, Position #26, Sample 534

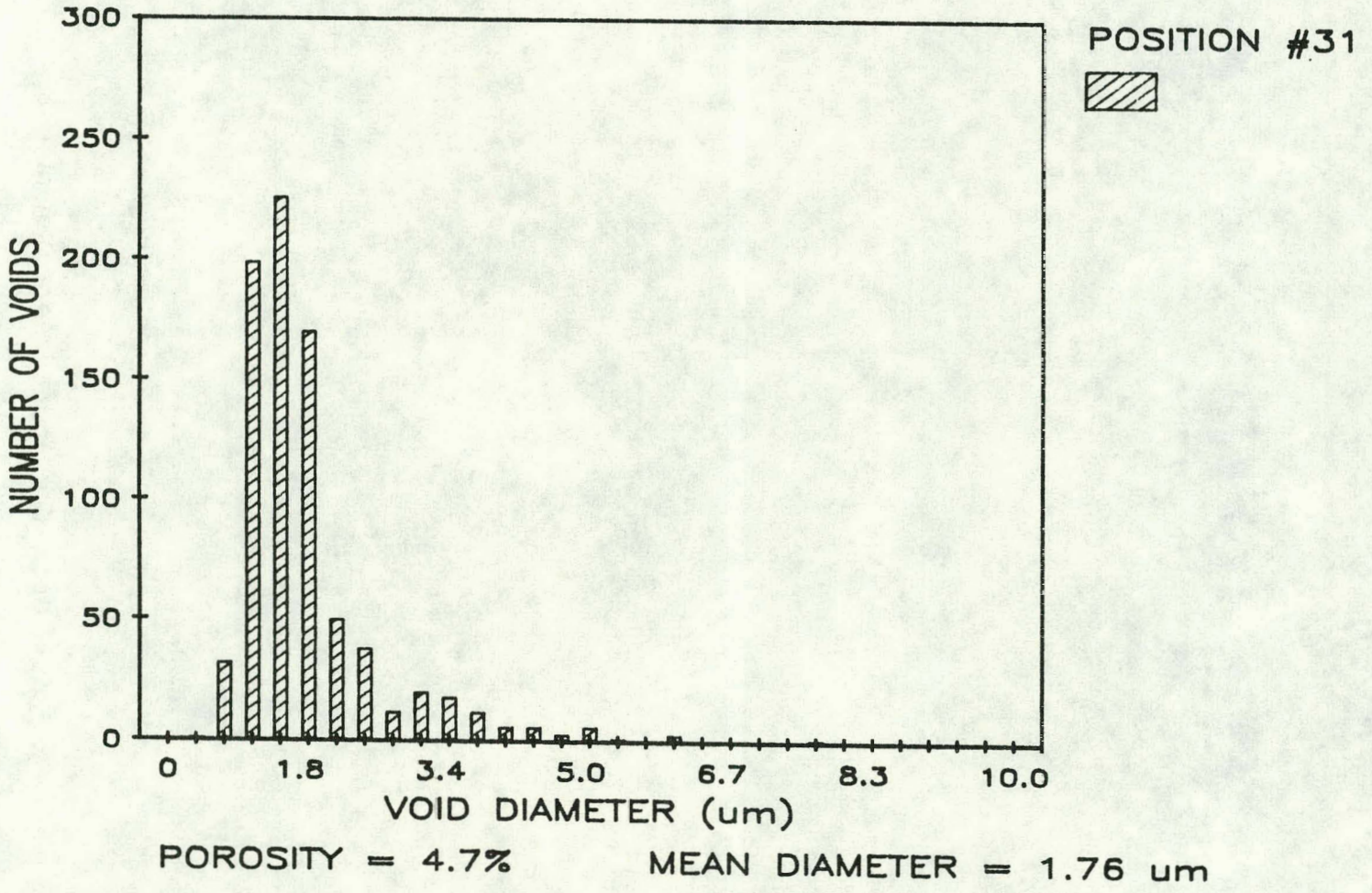

Figure 3-6. Void Size Distribution, SiC Ceramic, Position #31, Sample 534

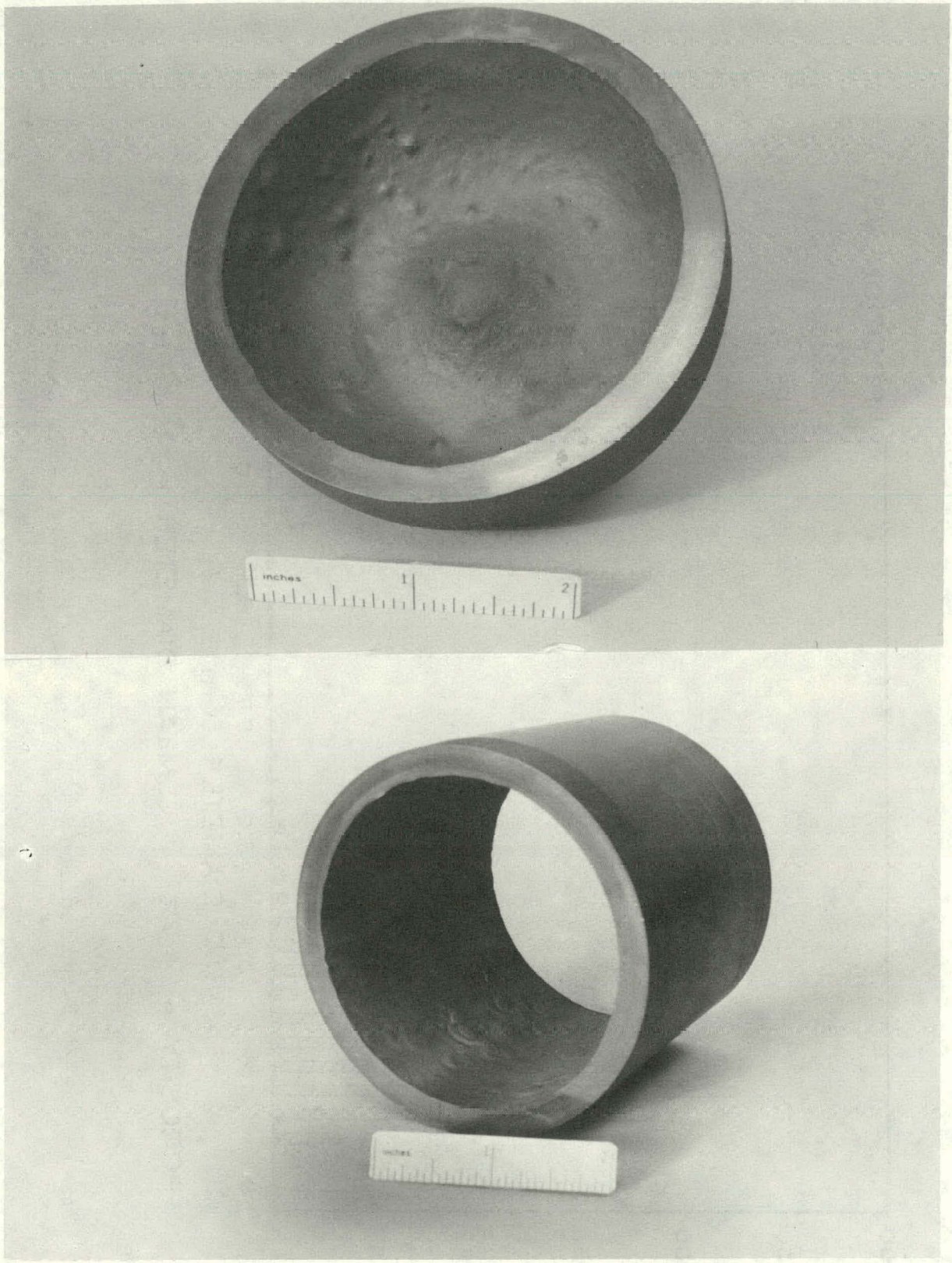

Figure 3-7. Tube Geometry and Surface Roughness

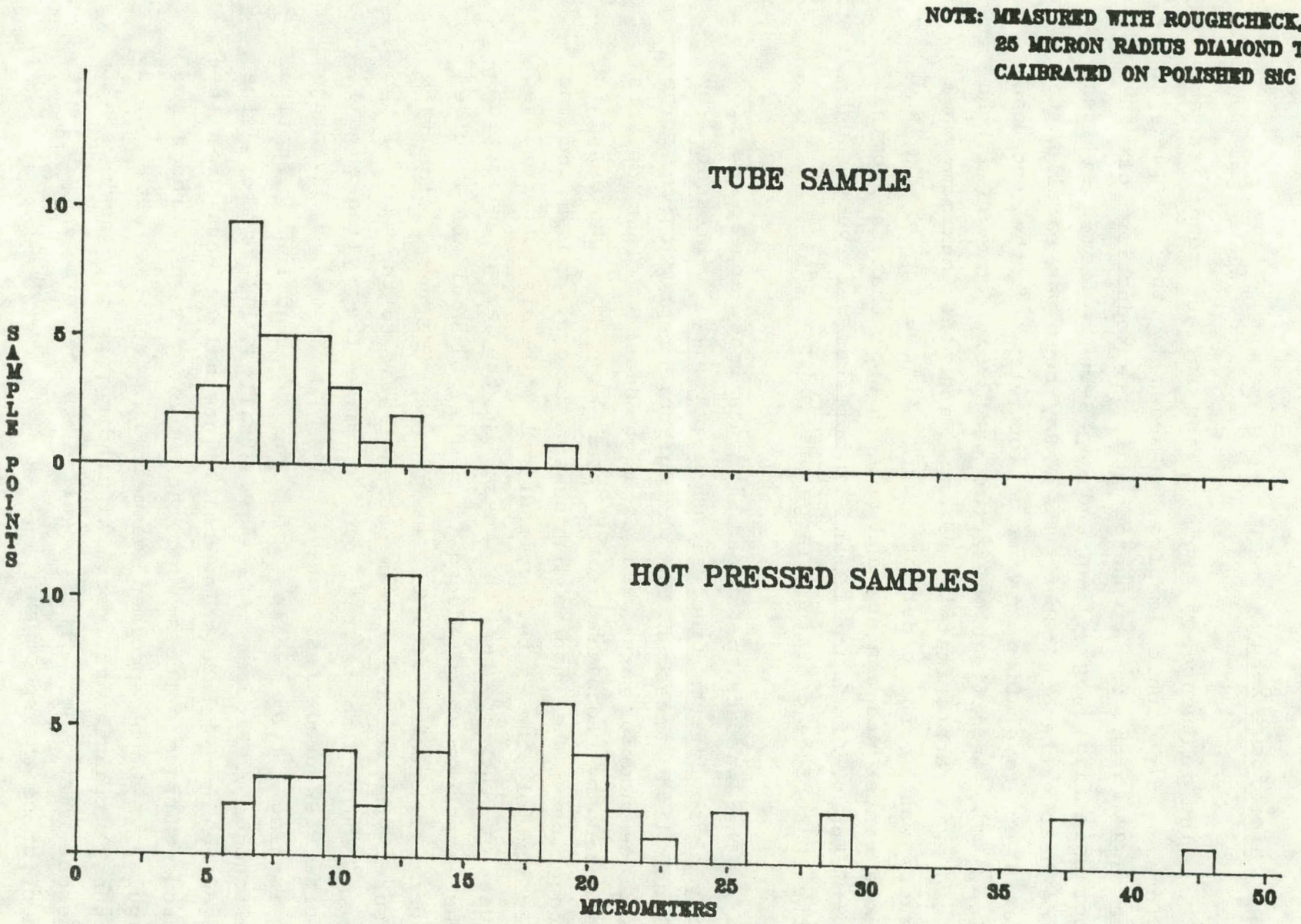

Figure 3-8. SiC Surface Roughness Measurements

3.4.1 Microfocus X-Ray

The influence of geometry and surface condition on microfocus radiographic imaging is shown by the example in Figure 3-9 which is a photographic reproduction of the radiographic film image of an end cap section from a silicon carbide heat exchanger tube. The X-Ray beam was parallel to the axis of revolution giving a top view of the end cap section. The magnification factor was 2.5x. The OD of the end cap was approximately 89 mm, and the maximum wall thickness was of the order of 7 mm. At the top of the end cap, the center was concave and much thinner than the nominal wall thickness. Both the OD and ID surfaces were very rough, and the ID surface contained large protruding nodules.

The surface pits and indentations appear as low density class defects (inclusions or porosity) represented by localized light areas on the photographic reproduction. The ID surface nodules are seen as high density class defects represented by localized dark areas on the photographic reproduction. The thin-walled center is overexposed and the projection of the outer cylindrical wall is underexposed because of the greater thickness in the axial direction. Another exposure at a reduced time interval would be required to image the center area of the end cap. Several side view exposures with the X-Ray beam perpendicular to the axis of the end cap would also be required to image the cylinder wall. The side view exposures, however, would have the disdavantage of imaging two walls of the cylindrical section simultaneously. Figure 3-9 graphically illustrates the difficulty in distinguishing small internal defects from the numerous surface defects when the surface is very rough and irregular. When specimen geometry is complex with rapid thickness transitions, several radiographic exposures at different views are often required to perform an adequate inspection of the specimen.

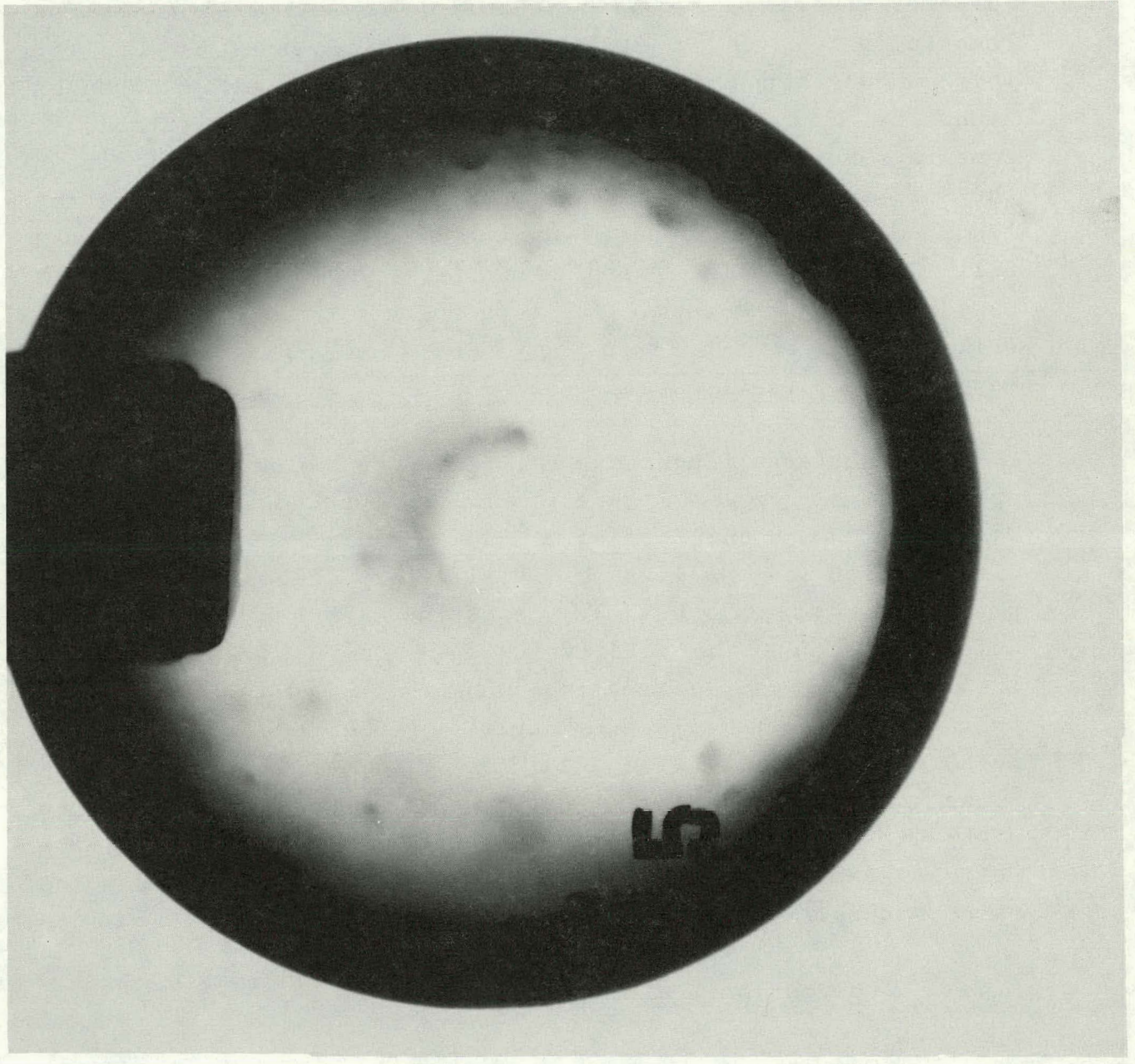

Figure 3-9. Microfocus Image of End Cap Section from Heat Exchanger Assembly

3.4.2 Scanning Laser Acoustic Microscope (SLAM)

In examinations using the SLAM, geometry , especially curvature, plays a significant role. The critical angle for longitudinal waves is 6.8°, and for shear waves it is 11°. This means that the entire width of the 30 MHz transducer cannot be used on the tube. Regardless of tube orientations, some rays must be beyond the shear critical angle. This means the full screen area cannot be used at maximum sensitivity for longitudinal defect scans. On the other hand, a rotary scan will present a defect with sound from many directions as it passes through the beam. The tapered section and flat section will need their own fixturing. The recurved bottom section may be impossible to scan.

Surface roughness is a real problem. The flat specimens, as pressed, have a surface roughness of about 20 μm. This takes the form of a locally smooth surface covered with hills and valleys of millimeter dimensions. This produces a scattered field obscuring all but the largest defects, because the relatively large areas on the sides of the hills and valleys scatter sound in all directions. The tube samples generally have only one-fourth the roughness, measured by a gauge with a stylus radius of 25 μm, but much worse microscopic roughness. They are not as difficult to work with as the flat samples, but not nearly as good as the polished samples. The primary difficulty in the tube samples is curvature.

3.4.3 Conventional Ultrasonics

The ceramic heat exchanger tubes tested in this project are composed of several different shaped sections. At the closed end, the shape is approximately hemispherical with a dimple indented from the outside which appears as a raised point on the inside. This hemisphere terminates a long

cylindrical section at one end. At the other end, the cylinder turns into an expanding truncated conical section. The conical section is terminated by a flange of uniform thickness.

In all cases, the radius of curvature of the various sections is so large in comparison to ultrasonic wavelengths in use that little effect should be seen. The major effect to be expected is that if curvatures locally change, then methods will be required to maintain angles of incidence of the impinging ultrasonic beam. Because of the large ratios of velocities in ceramic compared to water, a small change in incident angle will produce a significant change in refracted angle.

The only region where shape produced a problem is the dimple in the hemispherical end. The size and shape of the dimple prevents introducing ultrasound at an angle of incidence below any of the critical angles for longitudinal, shear or Rayleigh waves.

Surface roughness appears to be responsible for the inability to apply Rayleigh waves to surface defect detection. However, surface roughness also contributes to problems in using shear and longitudinal waves. Propagation through the rough surface of both the square samples and the tube samples contributes to loss of coherence in the ultrasonic waves and scattering of the beam. Two transducers have been used for much of the conventional ultrasonic work, one with a bandwidth from about 15 MHz to 45 MHz, and the other from about 10 MHz to 100 MHz. The useable frequency response of the higher frequency transducer can be limited to about 60 MHz when propagating through rough sample surfaces. The lower frequency transducer's response is sometimes limited to 20 MHz, again by surface roughness.

Although inherent attenuation has not been measured, it does not appear to be a problem. Surface roughness causes much greater signal loss than does attenuation arising from other sources.

3.5 WALL THICKNESS VARIATION

Ultrasonic methods, described in Sections 2.2.3 and 2.3.3, are the best and fastest means of measuring wall thickness over most of the tube. They are useful everywhere except at the dimple in the end of the tube, where the curvature prevents adequate control of beam angle. The sharp curvature causes excessive refraction and spreading of the beam, and the inner and outer surfaces are not locally parallel.

Unfortunately, the only significant deviation from uniform wall thickness in the tube tested was at the dimple. This is discussed in Section 3.4.1. Wall thickness at this point could be measured by x-ray attenuation, by a special purpose opposing head gauge, or by eddy currents.

3.6 CRACK CLOSURE TESTS

It has been suggested that cracks might be detected by the variation of ultrasonic response with applied stress, as the crack opens and closes slightly. This was tested by applying a cyclic load to the sample and looking for a synchronous response in the sample.

The measurement of the variation of crack reflectivity with loading, which tends to close the crack, was performed using an immersion ultrasonic system. The ultrasonic system used a 50 MHz transducer oriented and positioned to produce a

45° shear wave propagating into a corner reflector. This corner reflector is formed by the lower surface of the bar and the surface of a crack produced by Knoop indentation.

Loading was applied by four point bending as shown in Figure 3-10. As shown in this figure, the bending moment is uniform between the two inner supports and is P /2 N-cm. The stress is given by:

$$\sigma = \frac{MC}{I}$$

where σ is the stress, M is the bending moment, C is the distance from the neutral axis to the outer surface of the bar and I is the moment of inertia about the neutral axis. This equation can be rewritten as:

$$\sigma = M/Z$$

where Z is the section modulus given by I/ C. The section modulus is, in turn, given by $wt^2/6$ where w and t are the width and thickness of the bar, respectively.

Substituting into the last equation gives:

$$\sigma = \frac{P}{2} \cdot \frac{6}{wt^2} = \frac{3P}{wt^2}$$

For the sample fabricated for this experimental measurement, l is 25.4 mm (1 inch), w is 18.95 mm (0.746 inch), and t is 4.57 mm (0.180 inch). Thus:

σ = [196.16 (10^4) P] Pa where P is in newtons

([124.1 P] lbs/in^2 where P is in pounds)

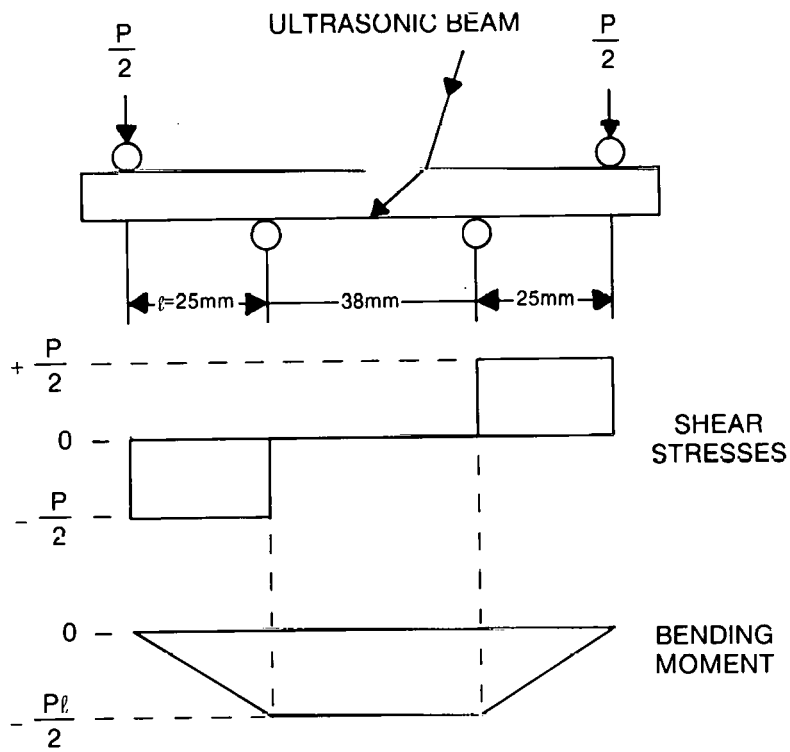

Figure 3-10. Four Point Loading of Sample to Determine Variation of Crack Reflectivity With Loading

For a stress of 68.95 mPa (10,000 psi), a total downward load of P = 358N (80.6 lbs.), or 179N (40.3 lbs.) is applied at each end of the bar.

Application of loads as shown in Figure 3-10 produces longitudinal compression in the lower surface of the bar. This stress would cause closure of the crack, if more closure is possible. The forcing of mating surfaces into contact would cause the crack to become ultrasonically transparent and, hence, would reduce the amplitude of the reflected signal.

Loads were applied in steps of approximately 89N (20 pounds) up to 445N (100 pounds). This produced a stress of about 86 mPa (12,500 psi). The load was increased to nearly 534N (120 pounds) when the bar failed, near one of the inner load points. During the variation in load and stress, the echo signal amplitude did not change significantly. From no load to 20 pounds, the amplitude decreased by less than 5%, and then remained constant thereafter. The initial decrease was probably caused by a change in transducer-sample orientation as the load was applied.

Had the stress applied to the bar been tensile at the surface containing the crack, a small change might have been obtained. Because of the high value of Young's modulus, high stresses would be required to cause crack opening. These stresses would probably have resulted in sample failure because of the stress concentration produced by the crack. It is likely that stresses large enough to begin to open the crack would cause failure before a significant change in reflectivity had occurred.

Unfortunately, there seems to be no practical means of applying this test to a full size recuperator tube.

3.7 UNSEEDED SPECIMENS

3.7.1 Microfocus X-Ray

Over one hundred naturally occurring flaws (i.e., porosity and high density inclusions) were detected in the silicon carbide specimens which consisted mainly of flat plates and sections of a heat exchanger tube. These flaws were internal type flaws and not the surface type defects detected in some of the specimens. The dimensions of the majority of the naturally occurring flaws were in the 200 to 625 μm range. Several flaws, however, had dimensions greater than 1000 μm.

Figure 3-11 shows an example of porosity type flaws in a silicon carbide plate (6.7 cm x 3.2 cm x 0.61 cm) with both surfaces machined to a smooth finish. At a magnification factor of 5x, the porosity type flaws are seen as small circular light spots on the photographic reproduction. The dimensions of the porosity were in the range of 200 to 300 μm. The vertical dark lines are the aluminum wires in the DIN 62 AL penetrameter described in Section 2.2.1.

Shown in Figure 3-12 is an example of high density inclusions. These inclusions were suspected to be a contamination of small iron particles. At a magnification factor of 5x, the high density inclusions are seen as small circular dark spots on the photographic reproduction of the radiographic film. The high density inclusions were in a silicon carbide plate (6.7 cm x 6.7 cm x 0.75 cm), both surfaces of which were very rough.

A conventional radiographic image of a sectioned specimen from a heat exchanger tube having a nominal wall thickness of 6.4 mm is shown in Figure 3-13. A large hook-shaped low density type defect can be seen at the lower

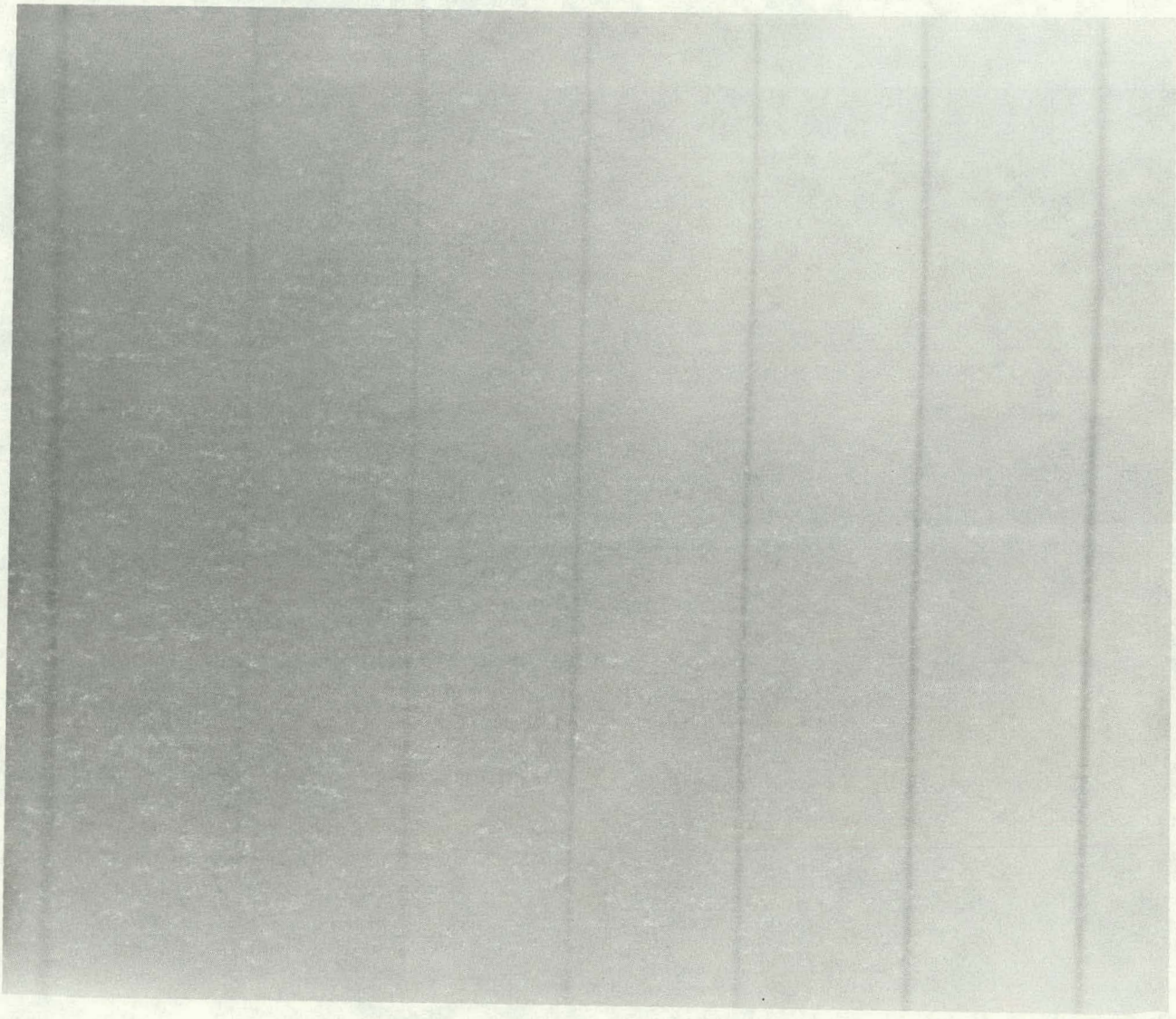

Figure 3-11. Microfocus Image of Porosity Type Naturally Occurring Flaws

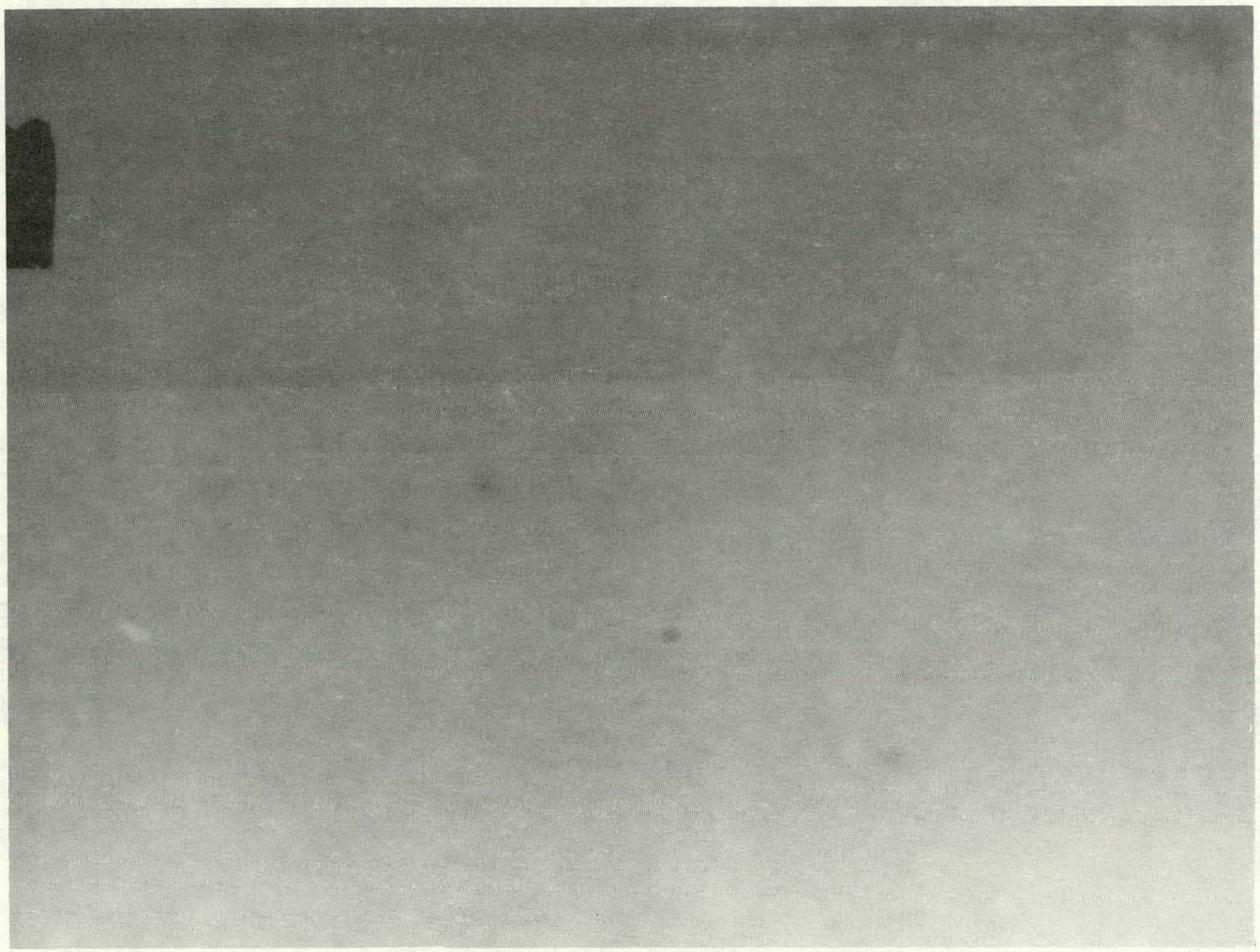

Figure 3-12. Microfocus Image of High Density Inclusions

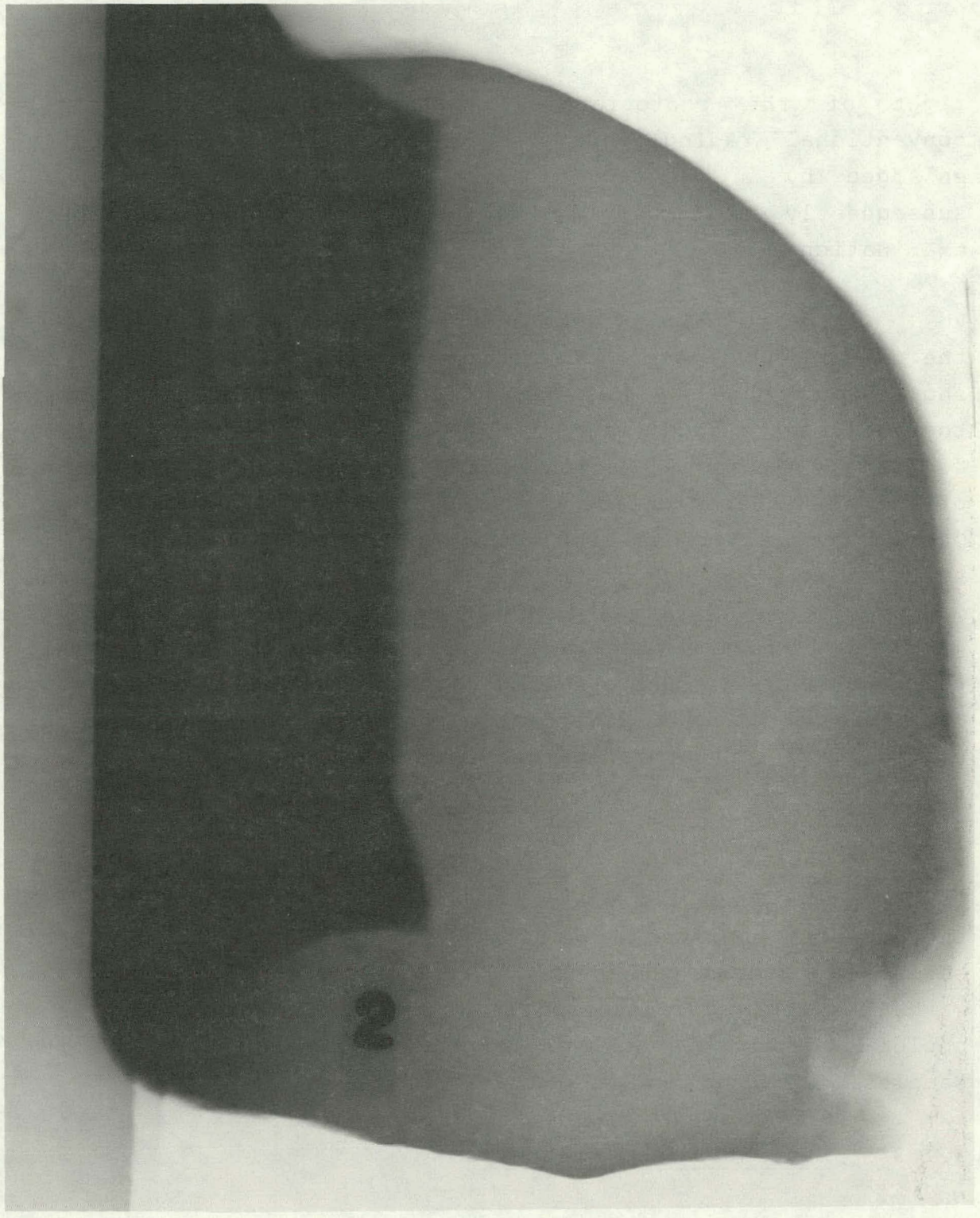

Figure 3-13. Conventional Contact Radiographic Image of Natural Flaws in Section of Heat Exchanger Tube

right of the photographic reproduction. The original conventional radiographic image has been photographically enlarged by a factor of about two. The specimen was subsequently sectioned at the defect for metallographic examination.

For comparison with conventional contact radiography, the microfocus radiographic image of the same specimen is shown in Figure 3-14. The sectioned pieces were taped together, but a good image of the hook-shaped defect can still be seen. The magnification factor was 3.6x. The dimensions of the hook-shaped defect were approximately 4.2 mm x 1.8 mm. Over thirty additional low density defects were detected in the same specimen using microfocus projection techniques. The defect dimensions ranged from 200 to 1400 μm, and the defects are seen as small circular light spots on the photographic reproduction. It should be noted that less than ten percent of these additional low density defects were detected by conventional contact radiographic methods.

3.7.2 SLAM

The SLAM was unable to detect any natural flaws in the unseeded specimens. As discussed in 3.4.2 and 2.3.2, the surface roughness caused such gross distortion of the sound waves that only delamination flaws or surface breaking cracks could be detected. Neither of these were found in the few samples of tubing tested.

3.7.3 Conventional Ultrasonics

Several flat samples were made with different densities; none of these contained intentional inclusions. One surface was polished on each of several samples. Ultrasonic C-scans were then made. In all of the C-scans, many small indications were obtained. By time gating the

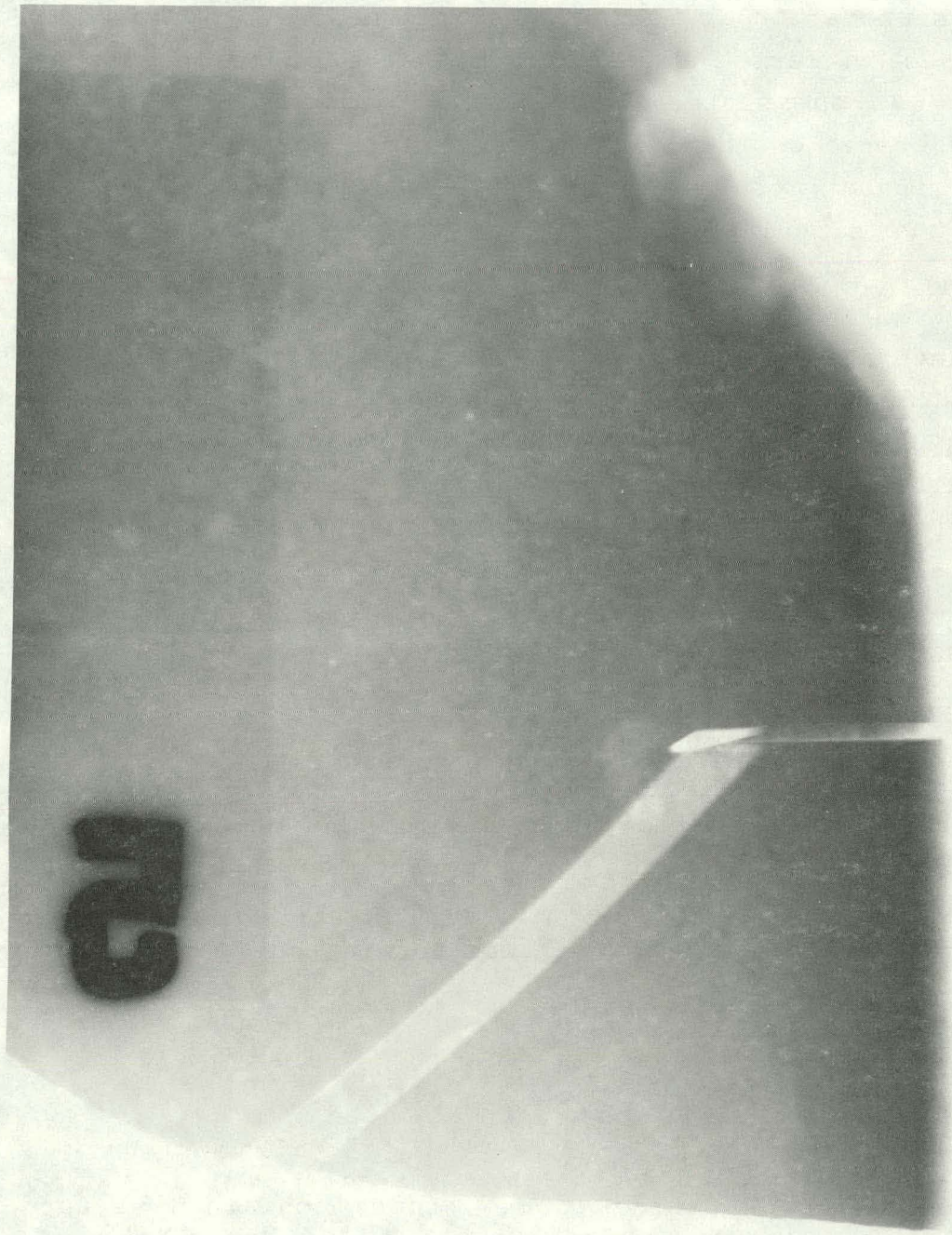

Figure 3-14. Microfocus Project Radiographic Image of Natural Flaws in Section of Heat Exchanger Tube

signal with a gate width of 0.4 microsecond, only defects in a laminar section about 2.5 mm thick are displayed. The indications appear on at least two scan lines 0.25 mm apart so that they do in fact indicate the presence of reflectors in the plate. In one plate, a circular pattern about 4.5 cm in diameter centered on the 5.7 cm square plate appeared to be of different microstructure (Figure 5-1). Many small reflectors, found in the circular region, were later determined to be porosity.

Several C-scans are included in Section 5. For these C-scans, a 50 MHz transducer with a 50 mm focal length (in water) was used. The focal length is reduced to about 6 mm in silicon carbide. The focal spot diameter should be about 2.0 mm, measured to the -6 dB points. Small reflectors would then be magnified in the C-scan.

3.8 HOT ISOSTATIC PRESSED SPECIMENS

Tests were to be run on Hot Isostatic Pressed (HIP) specimens supplied by TNEL. Unfortunately, the samples prepared were not of sufficient quality to be used. This was primarily due to the lack of a developed HIP technique. Development of such a technique was not an objective of this project and therefore this effort was terminated.

3.9 SEEDED FLAW SPECIMENS

3.9.1 Microfocus X-Ray

A silicon carbide plate that contained seeded spherical inclusions was examined. The spherical inclusions had nominal diameters of 750 μm, 250 μm, 100 μm, and 37 μm. One side of the specimen had been machined, and the other side was as-pressed. The results of the radiographic examination showed that several low density class defects were detected

with dimensions in the range of 250 to 625 μm. Figure 3-15 is a photographic reproduction of the radiographic film image of the seeded specimen where the magnification factor was 2.5x. The low density defects are seen as localized light areas on the photographic reproduction. The three largest seeded defects can be located from the map made when the specimen was fabricated. They are not otherwise distinguishable from the naturally occurring flaws.

A silicon carbide plate that contained seeded wire inclusions was examined. The specimen contained two platinum wires having diameters of 0.5 mm and 0.3 mm, respectively, and one tungsten/rhenium wire having a diameter of 0.25 mm. The wires were approximately 40 mm in length. Figure 3-16 shows a photographic reproduction of the radiographic image of the seeded wire inclusions where the magnification factor was 2.5x. Evidently, the platinum flowed and was forced out of the center of the billet during pressing. See Section 4.3.2 for results when the sample was sectioned.

A silicon carbide plate that contained seeded linear fiber inclusions was also examined. The fibers, made of graphite and aluminum oxide, were 10 μ and 12 μ in diameter. The radiographic examination showed no indication of the presence of linear inclusions.

3.9.1.1 Surface Flaws

The surface flaws were electrical discharge machining (EDM) notches placed in the wall of sectioned parts of a cylinder having a nominal wall thickness of 6.9 mm. ID and OD EDM notches were placed in different sectioned parts of the same cylinder. All notches were in the axial direction, and each set (both ID and OD) contained five notches with nominal depths of 0.13 mm, 0.25 mm, 0.51 mm, 0.76 mm, and 1.27 mm.

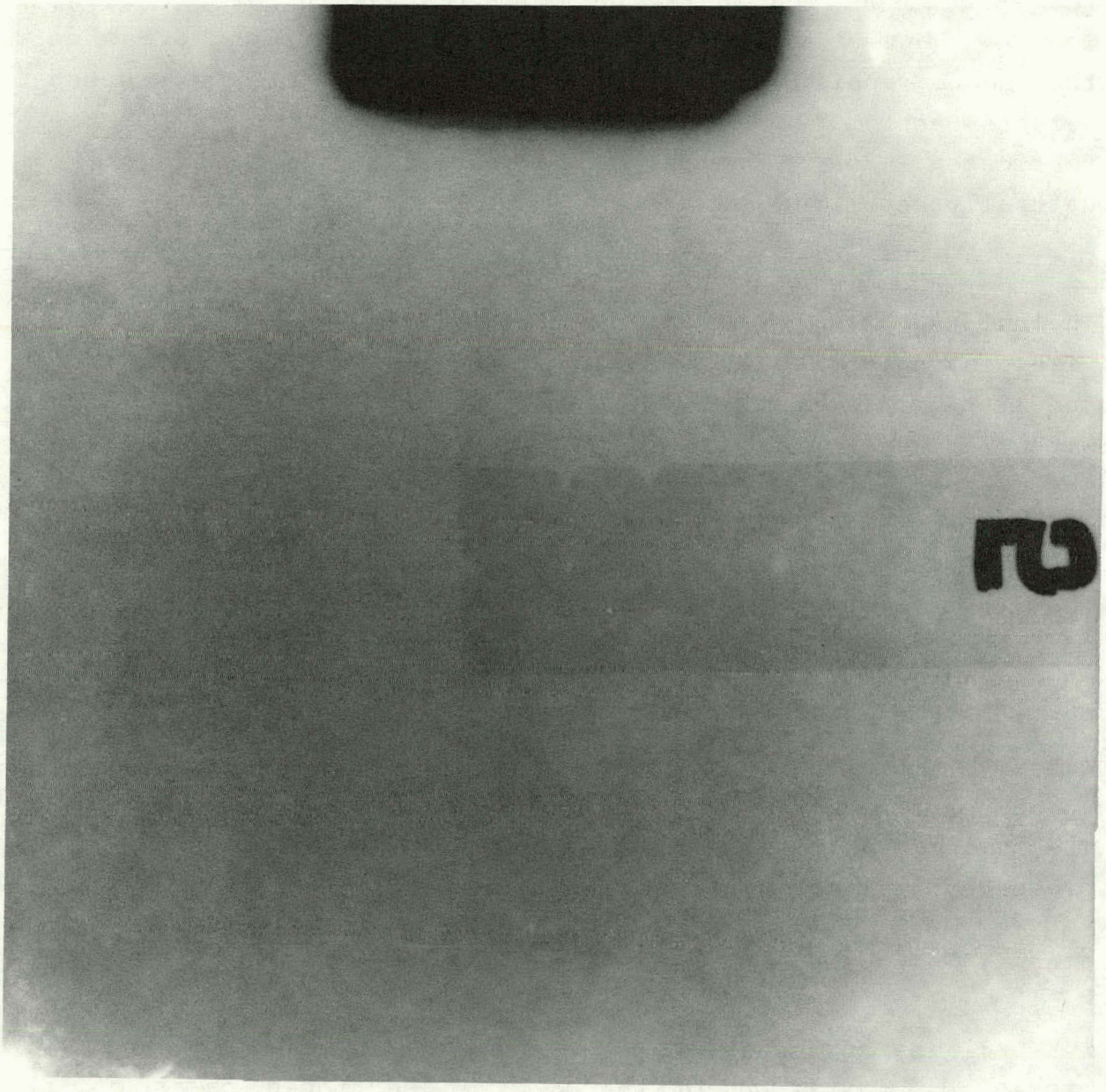

Figure 3-15. Microfocus Image of Silicon Carbide Specimen Containing Seeded Spherical Inclusions

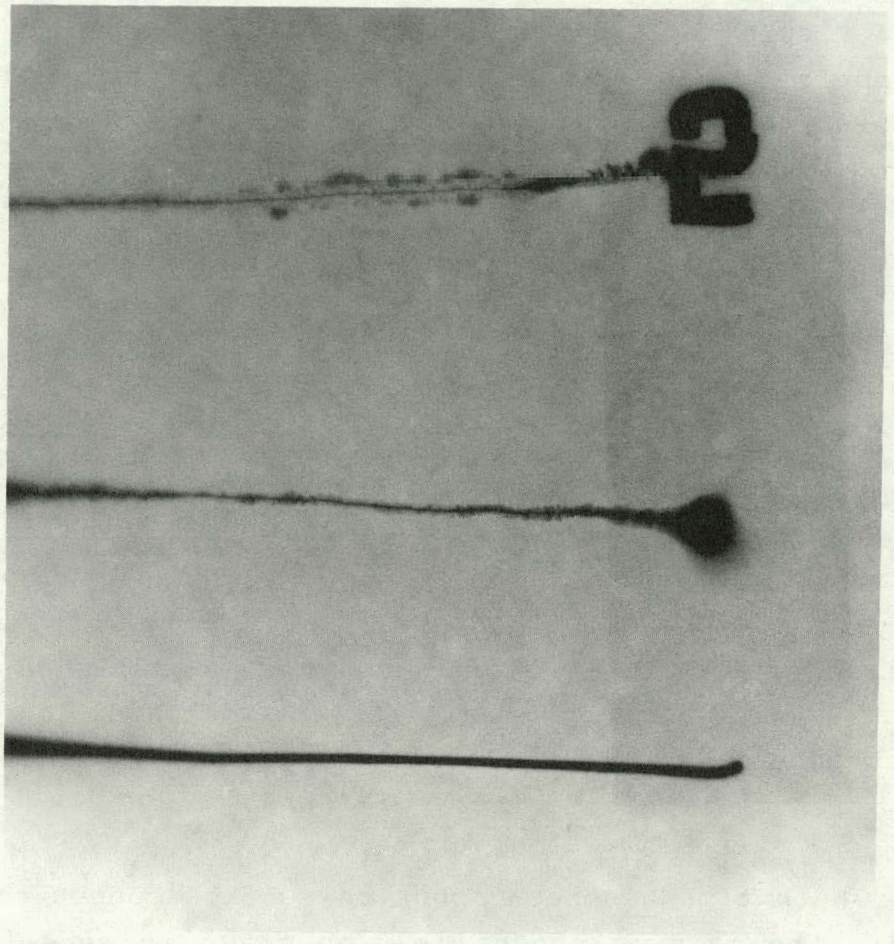

Figure 3-16. Microfocus Image of Seeded Wire Inclusions

The notch length in the axial direction was three times the notch depth. The EDM notches were aligned in the axial direction and spaced at intervals of approximately 25 mm.

Radiographic examination revealed all of the EDM notches, both ID and OD.

Figure 3-17 is a photographic reproduction of the radiographic image of the ID EDM notches at a magnification factor of 2x. The largest ID EDM notch having a depth of 1.27 mm is not shown in the view of the specimen seen in Figure 3-17. A 10x magnification of the two smaller OD EDM notches is shown in Figure 3-18.

3.9.2 SLAM

Although SLAM is excellent for surface crack detection, none of the embedded flaws were detected with the SLAM. This is probably because of the scattering from rough surfaces, described in Section 3.4.2. Because of the high velocity, most of these flaws are of the order of a wavelength or less in size. These can be detected on polished surfaces by their typical bullseye diffraction pattern, but not on rough surfaces. On the other hand, large delamination type cracks are immediately obvious with SLAM.

Much time has been spent on surface connected cracks, which are the main strength limiting flaws in ceramics. The standard SLAM inspection method is to look for the acoustic shadow of a crack. Because of the scattering and reverberation in this material, this method does not work well. However, reversing the sound field so that only backward reflected waves are detected provides a huge increase in sensitivity. Small indents on polished material are

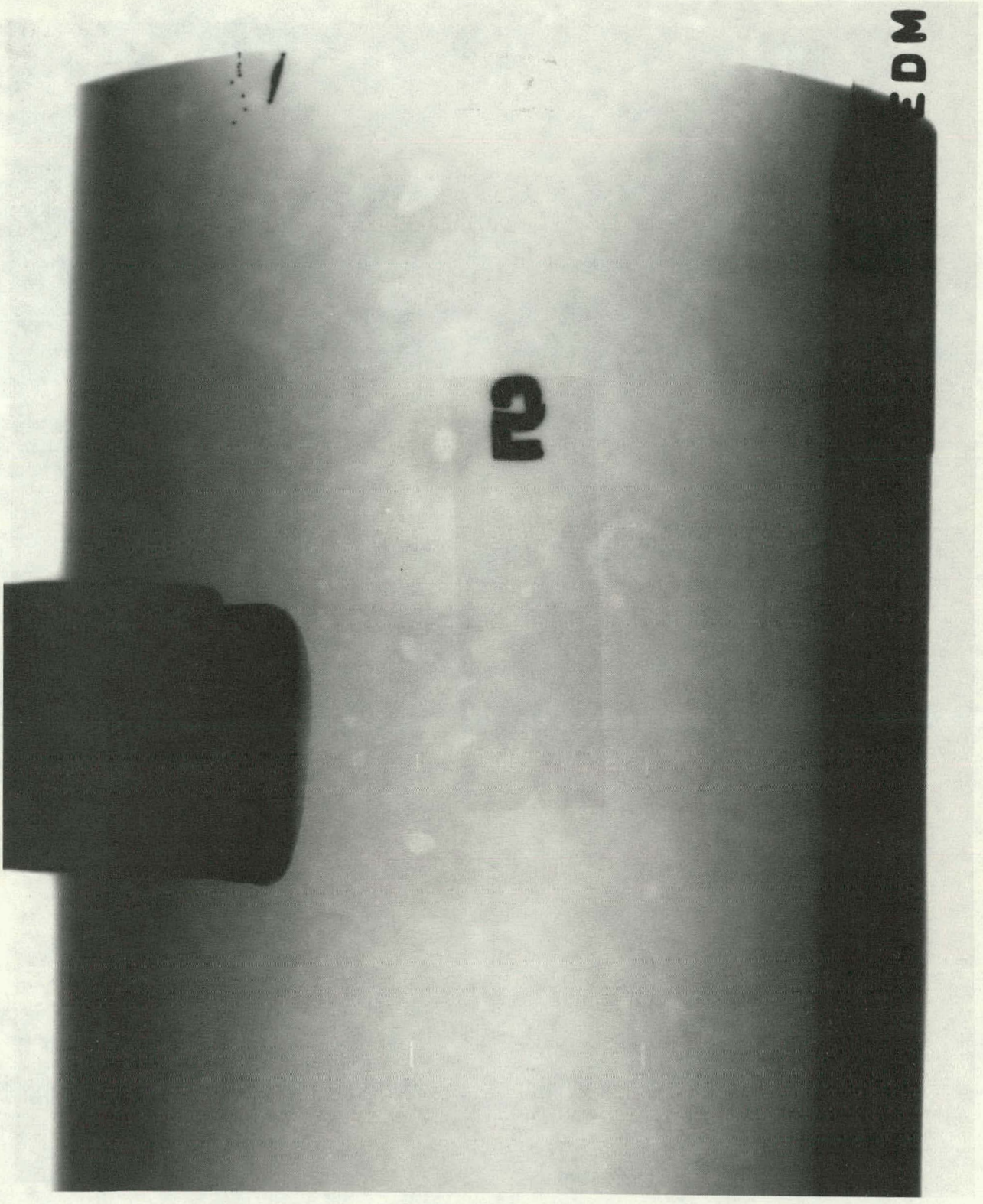

Figure 3-17. Microfocus Image of ID EDM Notches

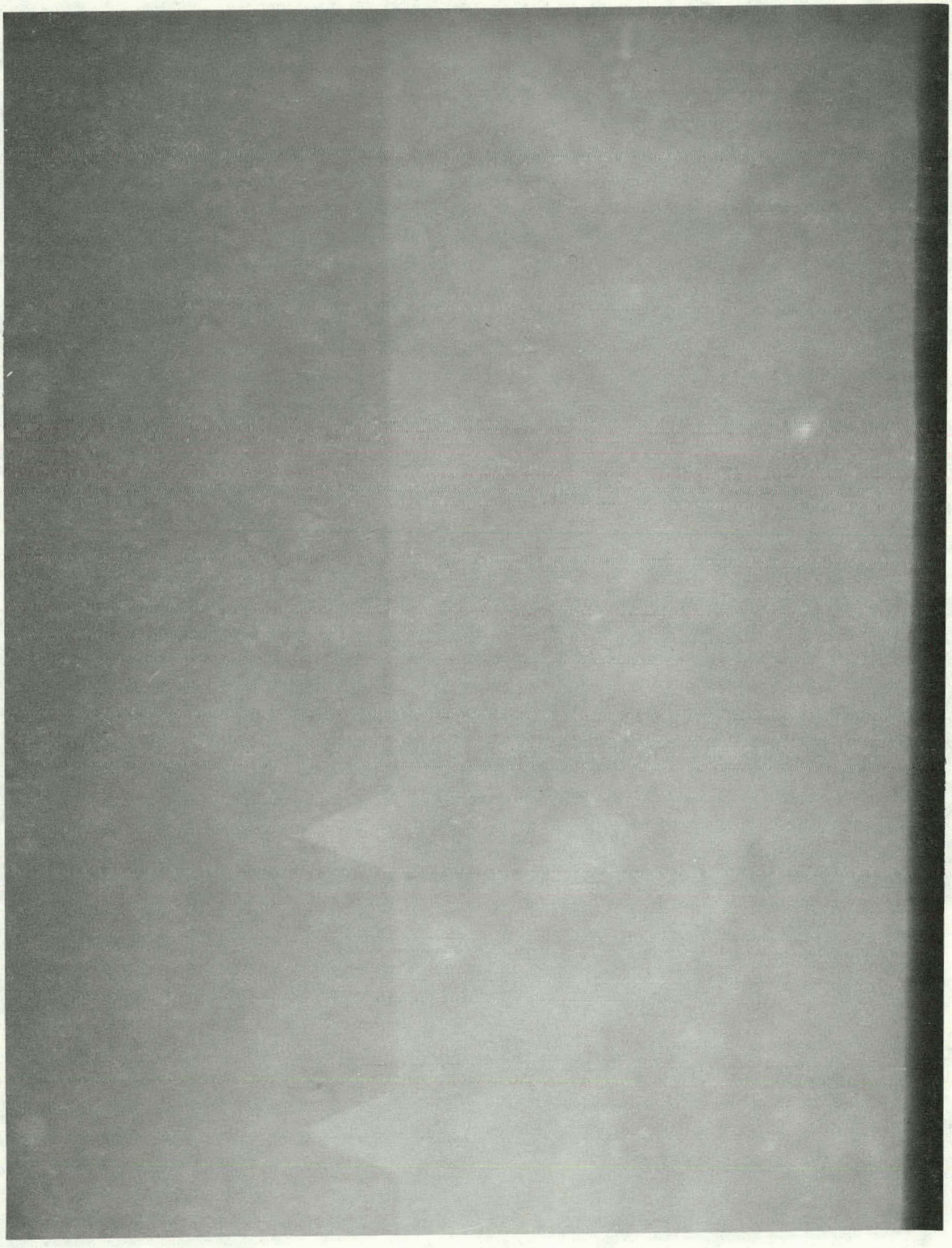

Figure 3-18. Microfocus Image of OD EDM Notches

extremely easy to locate. The SLAM was the only test method able to locate an eight newton Knoop indent on a polished surface. On tube samples, with the two curved surfaces and surface roughness, angles are critical and background is higher, but the four largest EDM notches can clearly be seen. The smallest (0.125 mm deep by 0.375 mm long) is lost in the background.

The SLAM is sensitive only to waves approaching at a certain small range of angles. This is because of the detection system. The effective detection frequency is shifted from the transducer frequency by the doppler effect, and the detected frequency is controlled by the local oscillator and the IF filter bandpass. These are factory set, but the local oscillator can be changed. When the reflection from a flaw has been in a direction with little scattering, and the oscillator tuned to the proper frequency, great sensitivity increase has been realized. Figure 3-19 shows SLAM images of EDM notches 0.25, 0.50, 0.75, and 1.25 mm deep. Lengths can be measured to 1 mm, but depth cannot be measured.

3.9.3 Conventional Ultrasonics

The development of techniques for detection and evaluation of bulk or embedded defects has been hindered by the difficulty of fabricating samples with known internal defects. Two samples were initially prepared, one with spherical inclusions and the second with linear filament inclusions. Only one spherical inclusion was found and it was not in the position where it had been placed. This defect was also found at the same place by microfocus radiography. Two other inclusions found by radiography were not detected ultrasonically.

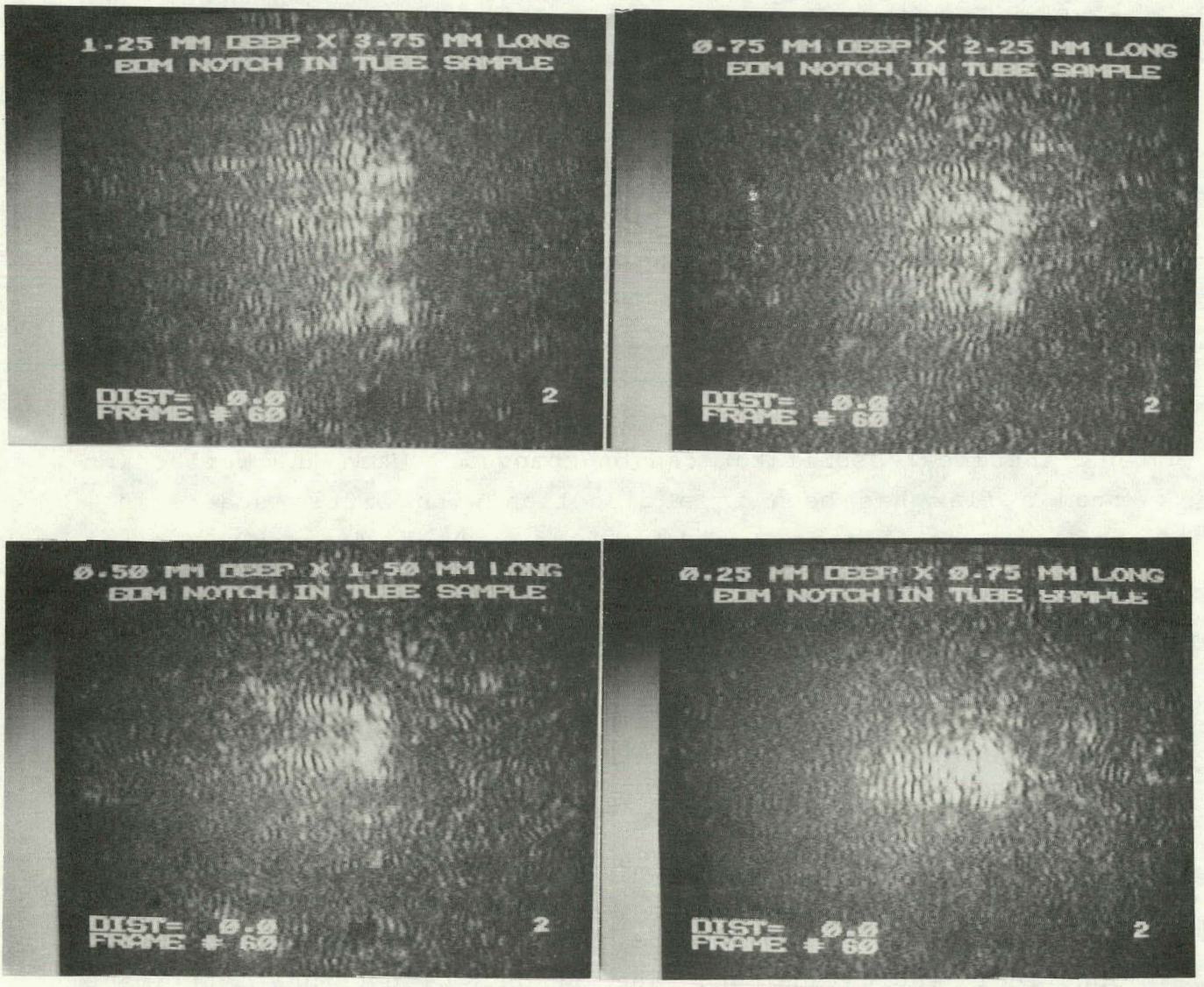

Figure 3-19. SLAM Images of EDM Notches

The linear inclusions were made of alumina fibers and graphite fibers. In one area, a small linear ultrasonic indication was found. Even after destructive testing it was not possible to determine whether this was a portion of one of the fibers.

A second sample with 0.5 and 0.3 mm diameter platinum wires, and a 0.25 mm diameter 75% tungsten - 25% rhenium wire was also inspected ultrasonically. All three wires were detected, but ultrasonic C-scan images of the wires were discontinuous. The C-scans are included in Section 5.

3.9.4 Surface Defect Detection

Surface defects have been simulated by placing EDM notches in the inner and outer surfaces of sections of heat exchanger tubing. These notches are 0.125, 0.25, 0.50, 0.75, and 1.25 mm deep with surface lengths three times the depth. The long dimensions of the notches are oriented axially and circumferentially on both surfaces.

All axially and circumferentially oriented notches on the outer surfaces, except the 0.125 mm deep notches, can be detected using ultrasonic shear waves. The waves are generated by mode conversion at the outer surface, propagate inwards at a 45° refracted angle, return to the outer surface to a corner reflector formed by the notch and the surface. The pulse then returns along the same path with reconversion to longitudinal waves at the surface, before returning to the transducer.

For the axially oriented notches, the ultrasound travels in a circumferential direction. If the transducer is moved towards the notch with the beam axis remaining parallel

to its initial orientation, the angle of incidence increases and the angle of refraction would also increase. The critical angle for shear waves would then be exceeded and the critical angle for Rayleigh waves would then be reached. (For silicon carbide in water, the Rayleigh wave critical angle is just over 12°.) No indications of Rayleigh waves were obtained, perhaps because surface roughness on the samples may be attenuating the surface waves. Shear waves of only slightly longer wavelength travel through the bulk material without excessive attenuation. Surface roughness may well be scattering the Rayleigh waves excessively. An additional possible cause for failure to see evidence of Rayleigh waves is the relatively high radiation losses encountered as the Rayleigh wave propagates along the surface.

Section 4
DESTRUCTIVE EXAMINATION OF SEEDED AND UNSEEDED SPECIMENS

4.1 INTRODUCTION

Some of the flat plate ceramic billets were cut into Modulus Of Rupture (MOR) test bars. These included both clean material and samples in which various naturally occurring defects had been located by NDE. In general, the detected defects were not strength limiting in this test, which emphasizes surface defects.

C-ring sections were cut from an actual heat exchanger tube sample, both at random and at locations selected for NDE indications. Again, the indications were not generally strength limiting.

The fractured surfaces have been examined by optical and electron microscopy.

4.2 MECHANICAL TESTING

Two types of strength testing were performed on specially prepared SiC specimens in 4- point bending. Four billets of different densities with no seeded defects were selected. Table 4-1 shows the density of each billet.

Table 4-1
Ceramic Densities for MOR Testing

Billet	% Theoretical Density
564	89.8%
565	99%
566	91.5%
568	97.6%

Each specimen prepared was approximately 0.75 cm x 0.32 cm and 6.6 cm in length. Five specimens were prepared from each billet. Before testing, the density of each specimen was determined using both an immersion technique and a geometrical technique. Only averages are reported, as density variations along the length of each specimen were unknown. Specimens were loaded on a 5 cm lower span and loaded in 4 point bending with the upper span being 2.5 cm. Each specimen was tested at 0.5 mm/min. until failure occurred.

Stress, strain and modulus of elasticity were determined from the load-displacement data collected. Table 4-2 summarizes the density and strength data obtained.

Table 4-2

Summary of Density and Strength Data

Sam.	Failure Stress mPa	St. Dev (mPa)	Average Mod of Elasticity	Average Immersion Density g/cc	Average Geometrical Density g/cc
564	185.1	19.97	3.44E + 07	2.86	2.91
565	226.7	41.5	4.16E + 07	3.17	3.13
566	179.8	17.3	3.31E + 07	2.92	2.86
568	211.9	23.96	3.45E + 07	3.05	3.07

From the data, it appears that there was no significant difference in strength between the compositions. There may be a trend of increasing strength with increasing density, as is shown in Figures 4-1 and 4-2, but the data scatter is too large to draw a firm conclusion. See Section 5.4 for more detail.

The second testing was conducted on C-ring specimens prepared from an as-received tube. Some specimens were prepared from randomly selected locations while other specimens were located at a position where a flaw or crack was detected using NDE.

Three sites on the tube were selected to obtain the randomly selected specimens. Four specimens were prepared from position A while three specimens each were prepared from positions B and C.

The remaining sections were examined using microfocus X-Ray. Detected flaws were identified, and then C-rings were

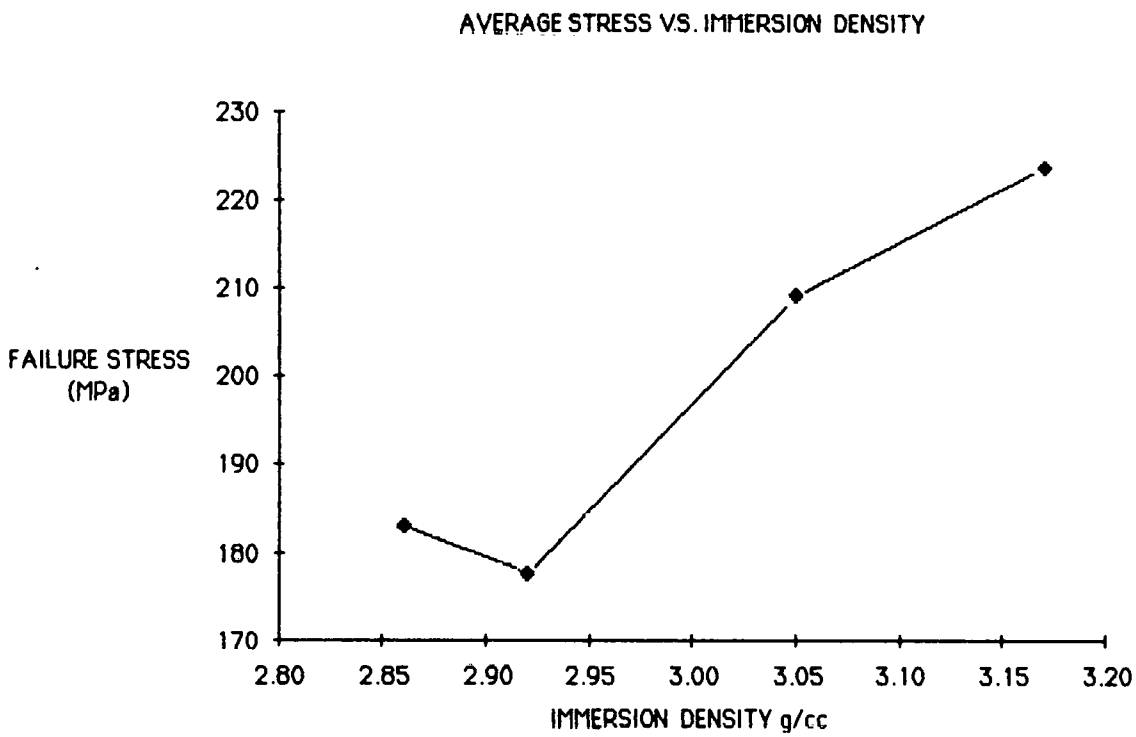

Figure 4-1. Failure Stress vs. Immersion Density

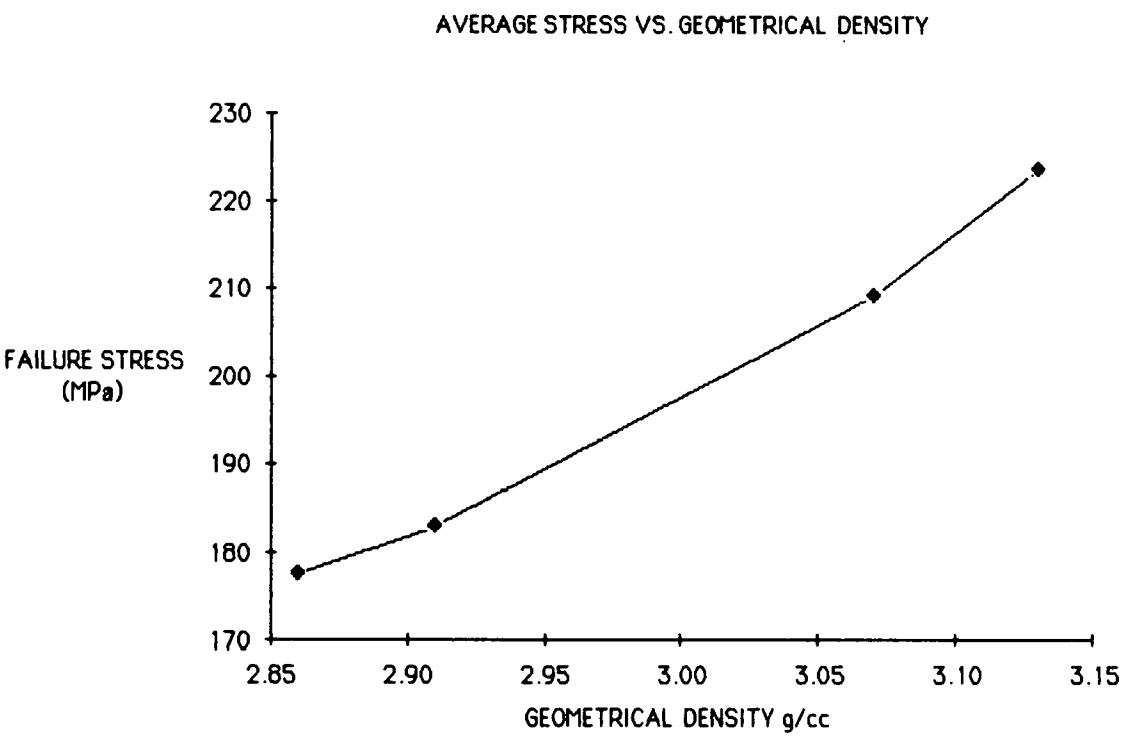

Figure 4-2. Failure Stress vs. Geometrical Density

cut with identified flaws in the testing area. Twelve specimens were prepared.

The C-rings were loaded in compression at a rate of 0.5 mm/min. until failure occurred. Table 4-3 summarizes the data obtained from the testing of the randomly selected specimens, and Table 4-4 shows the data from the specimens containing flaws. When tested, the majority of the specimens fractured into more than two segments. One specimen had four complete fractures.

Table 4-3
Summary of Strength Testing of As-Received Tube

Location	Average Immersion Density g/cc	Average Geometrical Density g/cc	Average Failure Stress MPa	St. Dev MPa
A	3.05	3.02	174.3	33.46
B	3.10	3.05	173.5	8.8
C	3.06	3.04	172.6	14.75

Table 4-4

Strength of C-Ring Specimens Containing Known Flaws

Ring #	Type of Flaw	Void Size μm	Failure Stress MPa
1	pores	400	160.2
2	3 pores	400	163.8
3	2 pores	400, 500	161.6
4	pore	650	174.2
5	pore	650	198.3
6	2 pores	450, 500	172.4
7	pore	750	151.4
8	pore	400	167.2
9	crack	2.5 cm in length, throughwall	112.8
10	crack	5 cm in length, throughwall	149.5
11	pores (peppered)	400 - 500	149.8
12	no significant voids		174.5

4.2.1 Additional Testing

Silicon carbide billet number 571 contained five defects as determined by NDE techniques. Of these defects, three were point defects and two were linear defects. Using a diamond saw blade and a diamond grinding wheel, five MOR bars were prepared so that each bar contained one of the defects near its surface. The surface containing the defect was then located on the tension surface for MOR testing, conducted in the four point mode with the defect located in the center of the high-tension zone. The upper loading points were on a span of 1.25 cm, and the lower loading points were on a span of 2.5 cm. The samples were tested at a constant strain rate

of 0.5 mm per minute. The MOR of each bar was calculated by computer software, using inputs of sample dimensions and load at failure.

The fracture surfaces were examined with a 50X stereomicroscope to determine possible defects present. Table 4-5 summarizes the results of the MOR testing and evaluation of the fracture surfaces.

Table 4-5: Summary of Results of MOR Testing of Billet 571 Containing Unseeded Defects

Sample Number	Type of Defect	MOR (mPa)	Fracture Location and Comments	Observations of Fracture Surfaces
1	Point	214.9	One fracture about 0.5 cm from defect area.	Possible inclusions into sample thickness.
2	Point	>354.5*	Three fractures at defect area.	Possible inclusions into sample thickness.
3	Linear	337.3	One fracture about 0.25 cm from defect area.	Possible inclusions at tension surface. Possible inclusions into sample thickness.
4	Point and Linear	287	One fracture about 0.5 cm from nearest defect area.	Possible inclusion at tension surface. Possible inclusions into sample thickness.
5	Point	261.7	Two fractures at defect area; another about 0.75 cm from defect area.	Crater of missing material on tension surface at defect area. Sample appeared to have been notched at fracture away from defect area.

*The actual failure load slightly exceeded the read-out range of the load cell.

Relative positions of samples are shown in Figure 5-13.

4.3 DESTRUCTIVE SECTIONING

4.3.1 Evaluation of Seeded Defects - Billet Number 763

Silicon carbide billet number 763 contained four different sizes (0.4, 0.6, 1.4 and 1.9 mm diameter) of platinum spheres. The sizes of the spheres were dimensioned as processed into the billet before hot pressing. Using a microfocus radiograph to determine location, saw cuts (0.41 mm kerf, diamond saw blade) were made in both the x-z plane and the y-z plane of both the largest and the smallest sphere. The x- and y-axes are parallel to the edges in the plane of the billet, and the z-axis is perpendicular to the plane of the billet.

Cut sections were then analyzed for defect dimensions with the scanning electron microscope (SEM). Using backscattered electrons, an image was formed with contrast resulting from the atomic weight difference between platinum and silicon carbide.

Figures 4-3 and 4-4 are SEM photomicrographs (approximately 10X) of the cross-sections of the largest (1.9 mm) platinum sphere. Since the accuracy of the SEM at low magnifications could not be closely controlled, the magnification of each photomicrograph at low power was measured by comparing photo measurements with actual measurements of the billet thickness. The defect dimension as measured from the photomicrographs were about 3.9 mm along the x-axis, 8.8 mm along the y-axis, and 3.6 mm along the z-axis. The reason for the increase in defect size (from the original 1.9 mm diameter) is shown in Figure 4-5. This is a 500X magnification SEM photomicrograph of the defect. The light areas are platinum and the darker areas are silicon carbide and porosity. The platinum was fragmented as a result of the

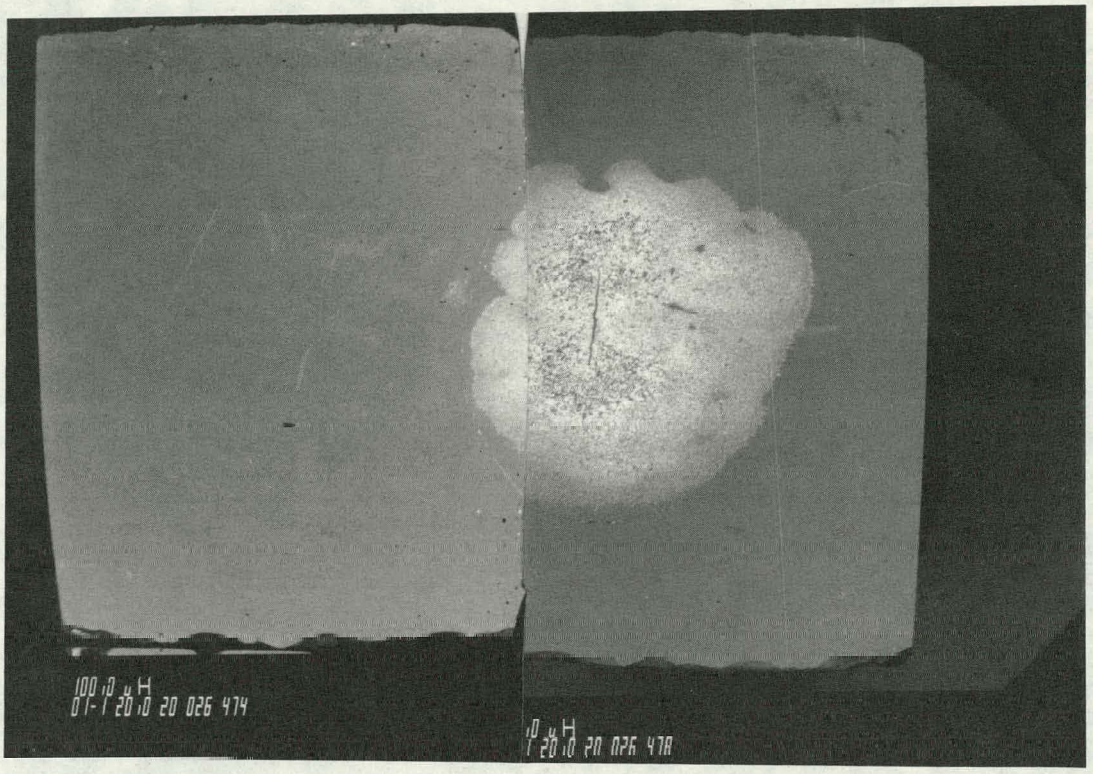

Figure 4-3. SEM Photomicrograph Showing Largest Platinum Seeded Defect, x-z Plane

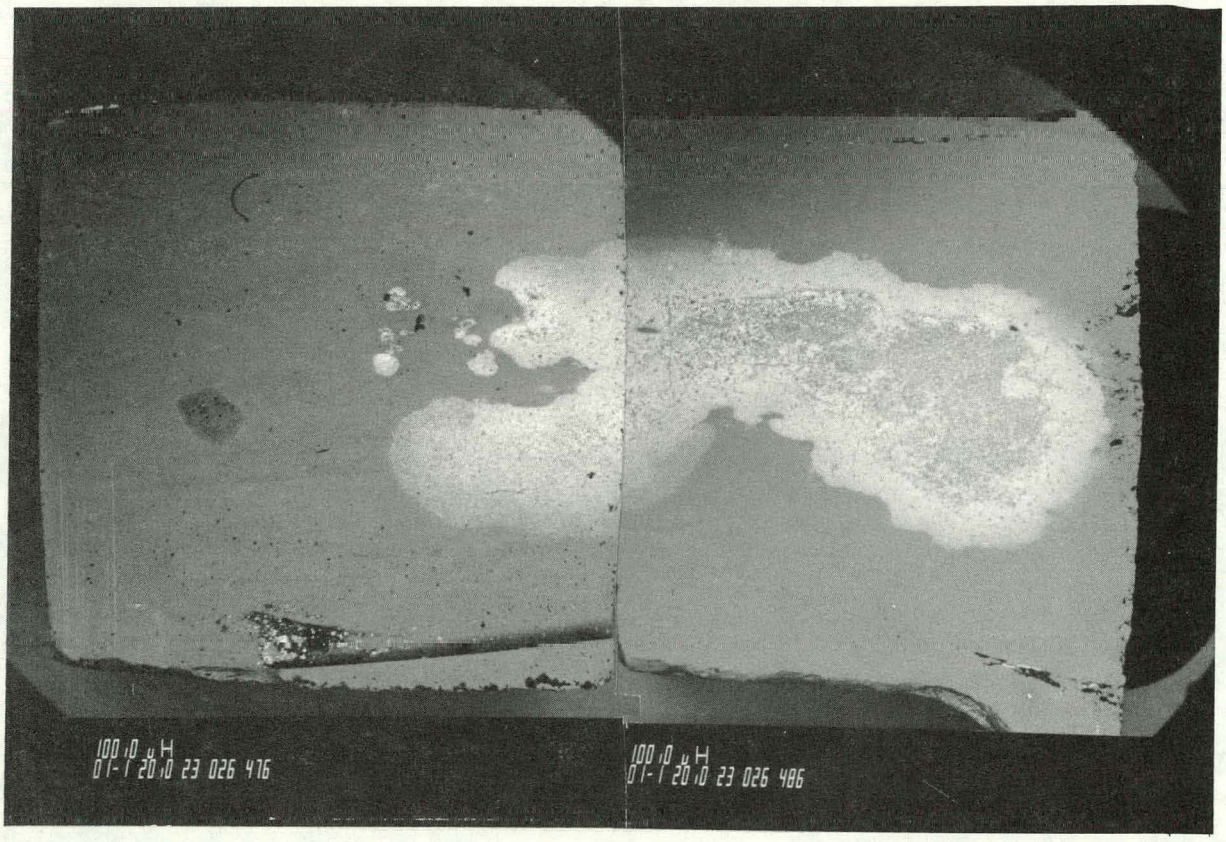

Figure 4-4. SEM Photomicrograph Showing Largest Platinum Seeded Defect, y-z Plane

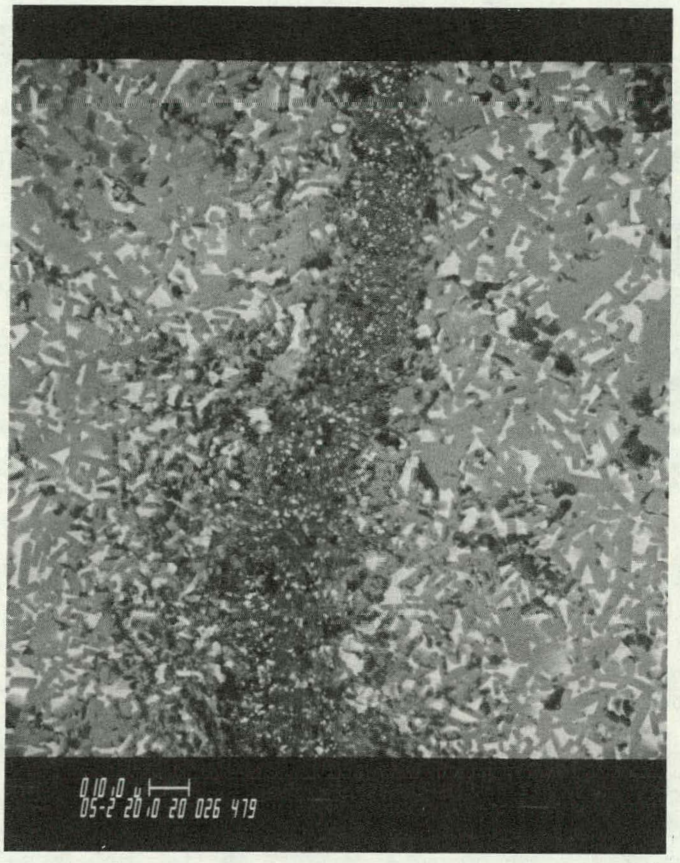

Figure 4-5. SEM Photomicrograph (500X) Showing Fragmentation of Platinum Seeded Defect

pressure/temperature of the hot pressing cycle and has been spread through a much larger volume than the original sphere occupied.

The same analysis was performed on the smallest platinum sphere which was originally 0.4 mm in diameter. Results showed the dimensions of this seeded defect to be about 3.0 mm along the x-axis, 3.6 mm along the y-axis, and 2.9 mm along the z-axis. The same fragmentation of the platinum sphere was evident.

4.3.2 Evaluation of Seeded Defects - Billet Number 759

Silicon carbide billet number 759 contained metal wires of three different diameters: 0.3 mm platinum wire, 0.5 mm platinum wire, and 0.25 mm tungsten/rhenium wire. These were the measured diameters prior to hot pressing in position along the y-axis of the billet.

A 1.4 mm kerf diamond saw blade was used to cut along the x-axis to determine cross-section dimensions of the seeded defects. The procedures used to destructively evaluate the size of the defects were similar to those used in evaluating billet number 763. SEM spectrum analysis was used to differentiate the platinum wires from the tungsten/rhenium wire.

Figures 4-6 and 4-7 are SEM photomicrographs (100X) of the cross-sections (x-z plane of the billet) of the platinum wires. Figure 4-6 shows the first platinum wire, measured to be 2.0 cm from a reference edge of the billet to the center of the defect. The major dimensions were measured to be about 0.75 mm along the x-axis and about 0.65 mm along the z-axis. Figure 4-7 shows the second platinum wire, measured to be 3.5 cm from the reference billet edge. The major dimensions were measured to be about 0.5 mm along the x-axis and about 0.8 mm along the z-axis. Referring to

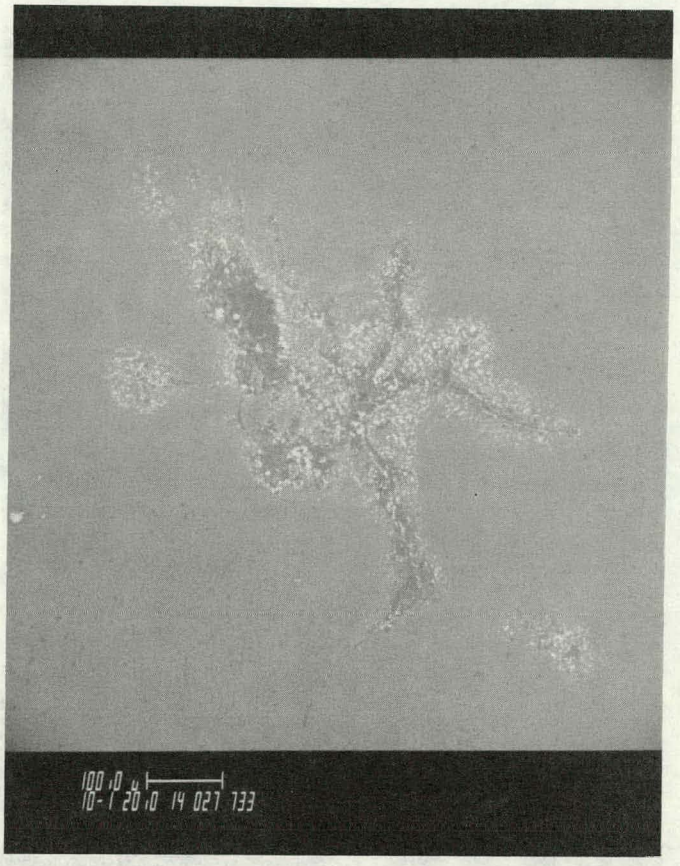

Figure 4-6. SEM Photomicrograph Showing First Platinum Wire

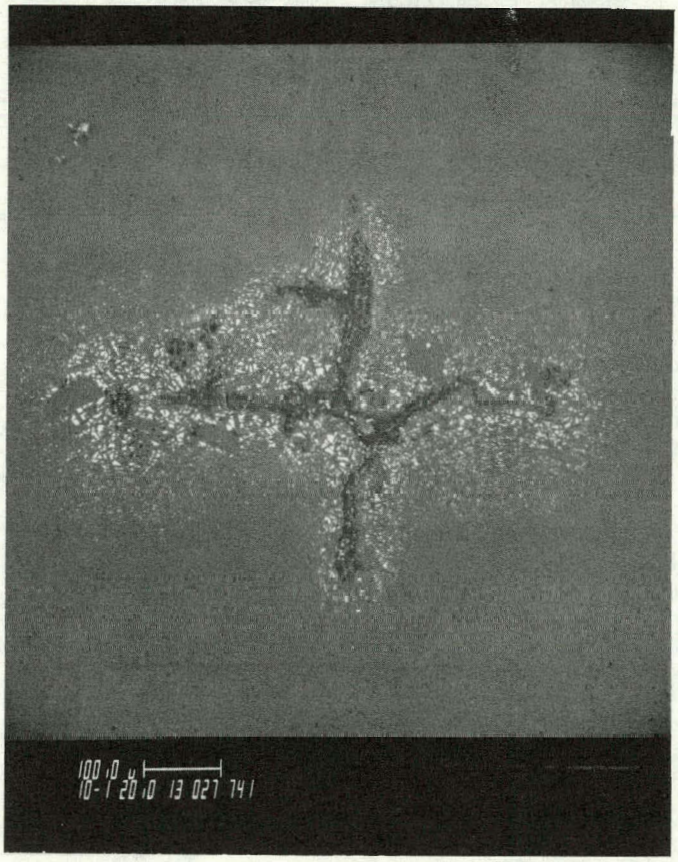

Figure 4-7. SEM Photomicrograph Showing Second Platinum Wire

processing information, it was determined that the wire in Figure 4-5 was the 0.5 mm wire and the wire in Figure 4-7 was the 0.3 mm wire. Because of the fragmentation of the platinum during the hot pressing cycle, it is difficult to differentiate the two from SEM photomicrographs.

Figure 4-8 is a SEM photomicrograph (150X) of the cross-section of the tungsten/rhenium wire. It was measured to be 4.9 cm from the reference billet edge. The major dimensions were measured to be about 0.48 mm along the x-axis and about 0.46 mm along the z-axis.

Both types of seeded defects showed the previously mentioned fragmentation due to the pressure/temperature of the hot pressing cycle.

4.4 FRACTOGRAPHY, SEM, AND OPTICAL EVALUATION

4.4.1 Scanning Electron Microscope (SEM)

The SEM was used to examine fracture surfaces and inclusions, and its X-Ray analysis capability was used to determine the elemental composition of inclusions. Section 4.3 contains six SEM photographs of metal spheres and wires in seeded samples. The elemental separations are dramatic.

4.4.2 Evaluation of Unseeded Defects - Billet Number 564

Silicon carbide billet number 564 contained two large defects, detected by NDE techniques. One defect was sized by microfocus X-Ray to be 0.3 mm along the y-axis and 0.6 mm along the x-axis. This defect was present but not significant on B&W and INEL C-scans. A second defect was sized by INEL C-scan to be 1.3 mm along the x-axis and 0.75 mm along the

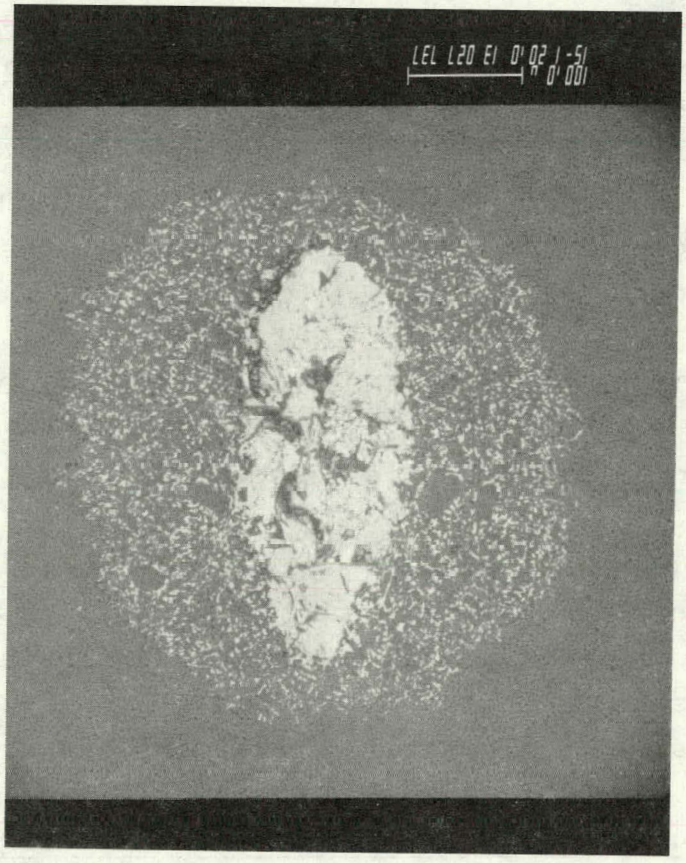

Figure 4-8. SEM Photomicrograph of Tungsten/Rhenium Wire

y-axis. This defect was not detected by B&W C-scans or x-ray. To evaluate these defects, a cut with a diamond saw blade was made outside of the defect area, located by NDE methods. The defect-containing piece was then ground down with a diamond grinding wheel in incremental amounts. At each increment, the surface of interest was examined using a 50X stereo-microscope. If a feature was evident, the surface was further examined with the SEM.

The defect sized to be 0.3 mm along the y-axis was also determined (by X-Ray) to be contained within the range of 0.5 mm and 0.8 mm inward from the surface of a preliminary cut billet 564. After grinding into this surface 0.5 mm, a feature was evident by optical microscopy. The feature was still evident at a total grind of 0.65 mm. At this level, the defect was examined by SEM. Figure 4-9 is a SEM photomicrograph (80X) of the x-z plane of this defect. The defect was made up of a large, dark inclusion mostly contained within a larger, oval crack. At this location, the dimensions of the dark inclusion were about 0.6 mm along the x-axis and 0.35 mm along the z-axis. The inclusion was determined by SEM spectrum analysis to be substantially made up of an element lighter than carbon. Since boron carbide was used as an additive in the preparation of the silicon carbide billet and since boron is lighter than carbon, it appears that this inclusion was a large grain of boron carbide. The dimensions of the oval crack were about 0.7 mm along the x-axis and 0.55 mm along the z-axis. It is interesting to note that the oval crack generally surrounds the inclusion, but it includes a significant amount of silicon carbide at one side and cuts off part of the inclusion at the other. It appears that the inclusion is well bonded to the silicon carbide, but has a different temperature coefficient of expansion.

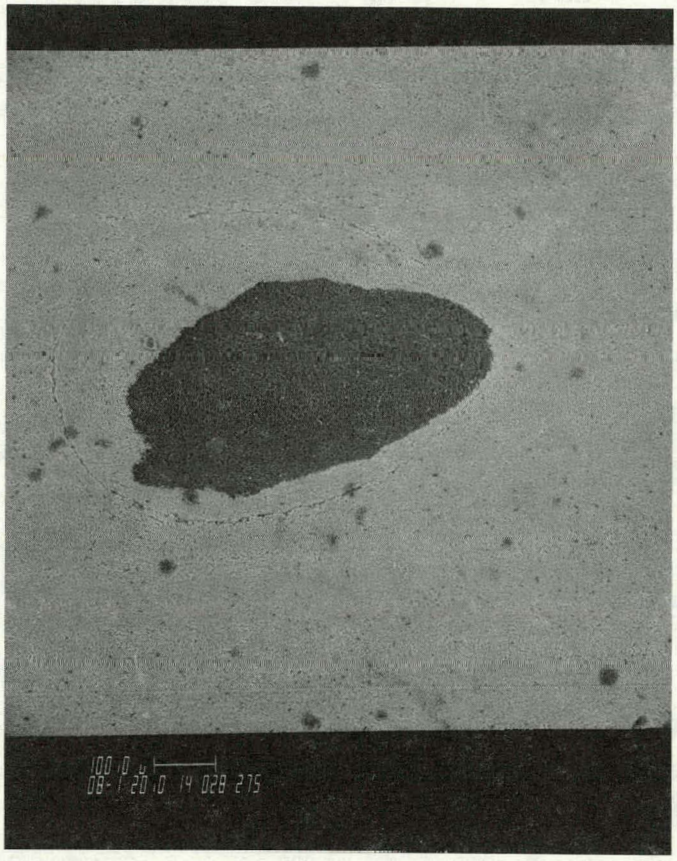

Figure 4-9. SEM Photomicrograph of Boron Carbide Inclusion and Oval Crack

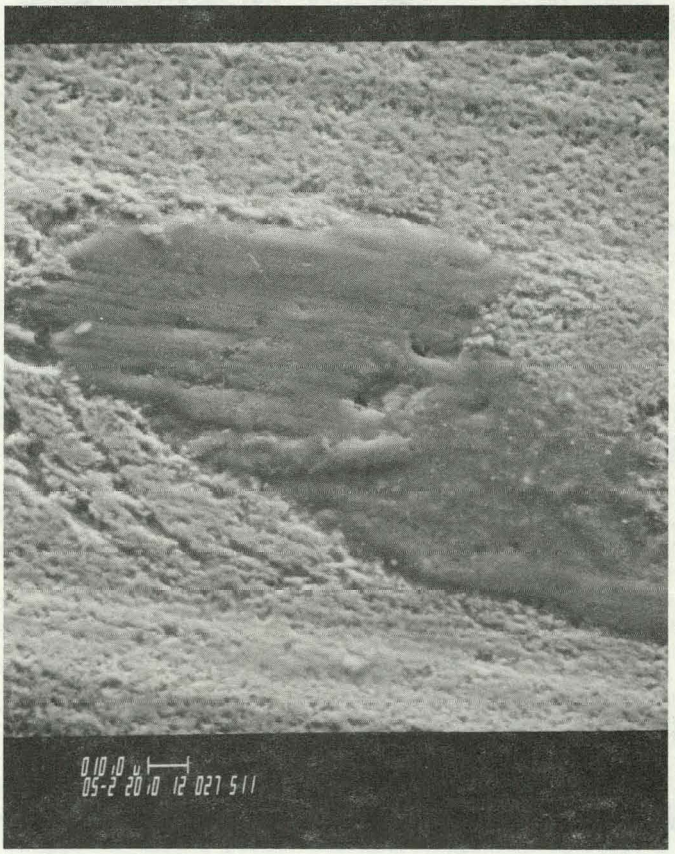

Figure 4-10. SEM Photomicrograph of Carbon Inclusion

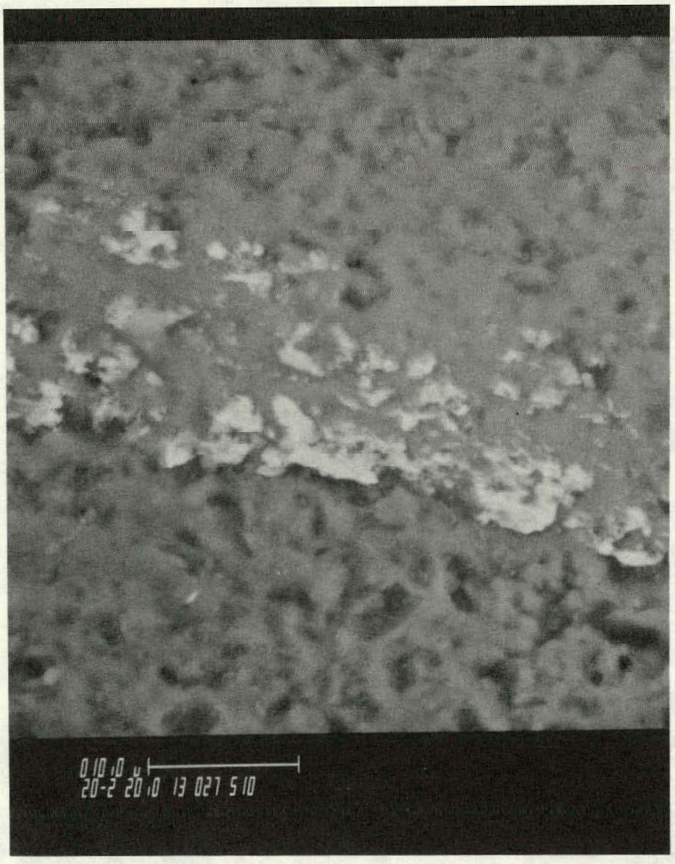

Figure 4-11. SEM Photomicrograph of Chrome-Iron Inclusion

The second, very large (1.3 by 0.7 mm) defect as detected by C-scan was not definitely located. Polishing revealed many spots of dense material in a more porous background, which formed a high background scatter for C-scan. The B&W C-scans showed this high background of dense regions, with nothing standing out. INEL evidently used a higher threshold, and may have located an extra-high-density region.

In the course of examining billet 564, two other inclusions were noted and photographed by SEM. They are shown in Figures 4-10, a carbon particle about 0.3 mm long, and Figure 4-11, a chrome iron alloy particle about 0.1 mm long. Neither inclusion produced a significant indication on any NDE technique.

4.4.3 Fractography

A fractographic analysis was conducted on all broken specimens. It was determined that some fractured surfaces exhibited features of slow crack growth while others exhibited features of fast fracture. Candidate sites for the crack origin were identified but the absolute identification of one critical flaw site could not be made. This work was carried out with the assistance of a consultant, J. J. Mecholsky of Pennsylvania State University.

Figures 4-12 and 4-13 show heat exchanger tube C-ring fracture surfaces at low and high magnifications. Note the bar in the identification block indicating 100 and 10 μm lengths.

The microstructure consists of large (50 to 150 μm diameter) silicon carbide grains and small (less than 10 μm diameter) grains of silicon carbide and silicon. The crack

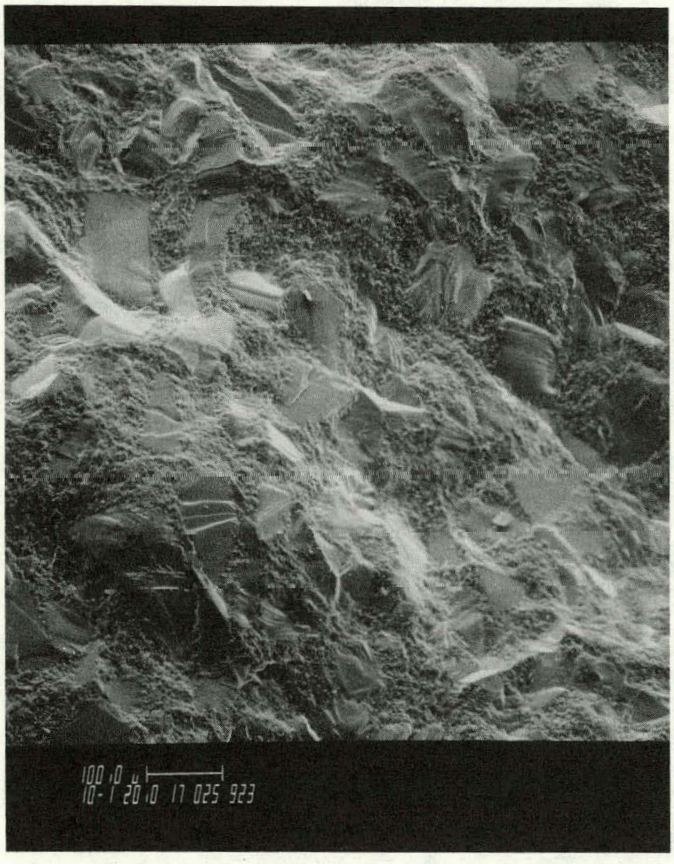

Figure 4-12. Tube Fracture Surface, Low Magnification

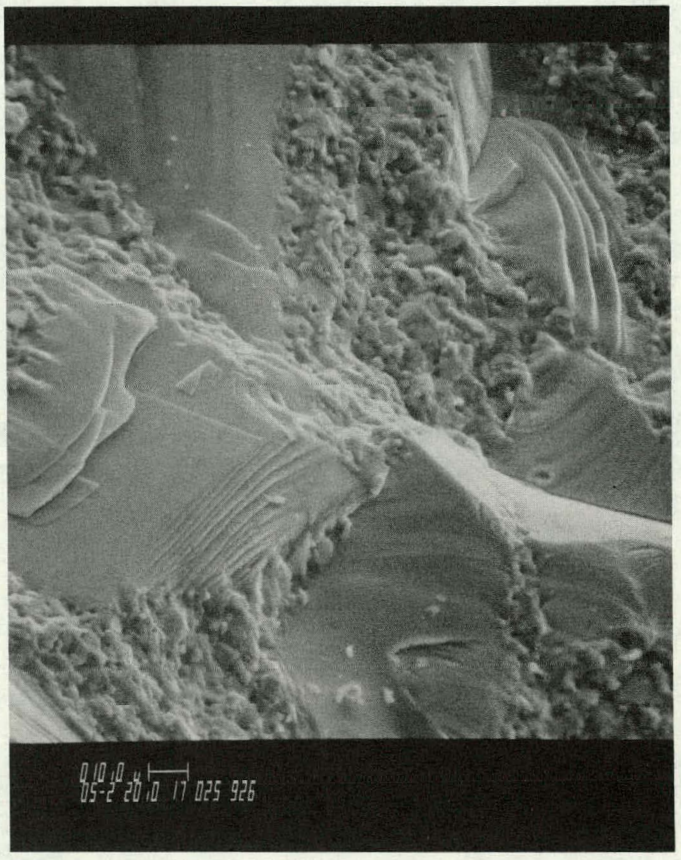

Figure 4-13. Tube Fracture Surface, High Magnification

front extended through the large silicon carbide grains. The fracture surfaces of the large silicon carbide grains show exfoliation in some areas and glassy fracture in other areas.

4.4.4 Fractographic Analysis and Optical Evaluation

Three C-rings which had NDE indications of natural flaws were examined to determine the primary break, and origin of fracture. NDE identified the flaws as discussed in Section 3. C-ring specimens were cut from the tube with one identified flaw or group of flaws in the testing area.

The C-ring configuration used for strength testing results in a stress distribution through the wall thickness of the specimen with the outside diameter surfaces in tension and the inside diameter surface in compression. Since ceramics normally fail in tension, the C-ring specimen is fractured with a bending stress with the crack originating on the tensile surface. The crack propagates radially from the outside surface but, may curl to the compression side.

The specimens were examined visually, and then optically with the use of a microscope and SEM. Visually, the overall topography of the surfaces was observed. Features such as surface roughness, coarse hackle markings, and hinges were noted.

Hackle markings (Figure 4-17) consist of ridges extending in the direction of fracture propagation and occur when the crack front is moving at a rapid velocity. Hinges are ridges formed during the last stages of crack propagation as the two fractured surfaces pivot just before complete fracture occurs. Consequently, crack initiation is located on

the opposite surface from the hinge. It is important to know the direction of crack propagation to determine the candidates for the first, or primary, fracture and the later, or secondary, fractures. In this test configuration, all fractures resulting from a crack propagating from the outside diameter toward the inside diameter are candidates for the primary break.

A rough surface indicates that fracture occurred at a high stress or that crack propagation was rapid. A smooth surface indicates the fracture occurred at a low stress, or the crack front velocity was slow. Distinguishing between high stress and low stress fractures is important when identifying the primary break and secondary breaks. The high stressed fracture would be a candidate for the primary fracture.

With the use of a microscope and SEM, surface features such as Wallner lines, cleavage marks, and river marks are identified. Wallner lines are very narrow curved undulations on the fracture surface and indicate the direction of crack propagation. Cracks propagate radially outward to the curved markings. Cleavage marks are short step markings. The individual markings are parallel and are perpendicular to the direction of crack propagation.

River marks are surface features which resemble the shape of a handheld fan. Crack propagation occurred parallel to the center axis of the fan from the base of the fan to the outer limits of the fan. Examples of cleavage marks, Wallner lines and river marks are shown in Figure 4-14. This area shows evidence of crack branching, that is, crack propagation occurred in several directions in one region, as indicated by the arrows.

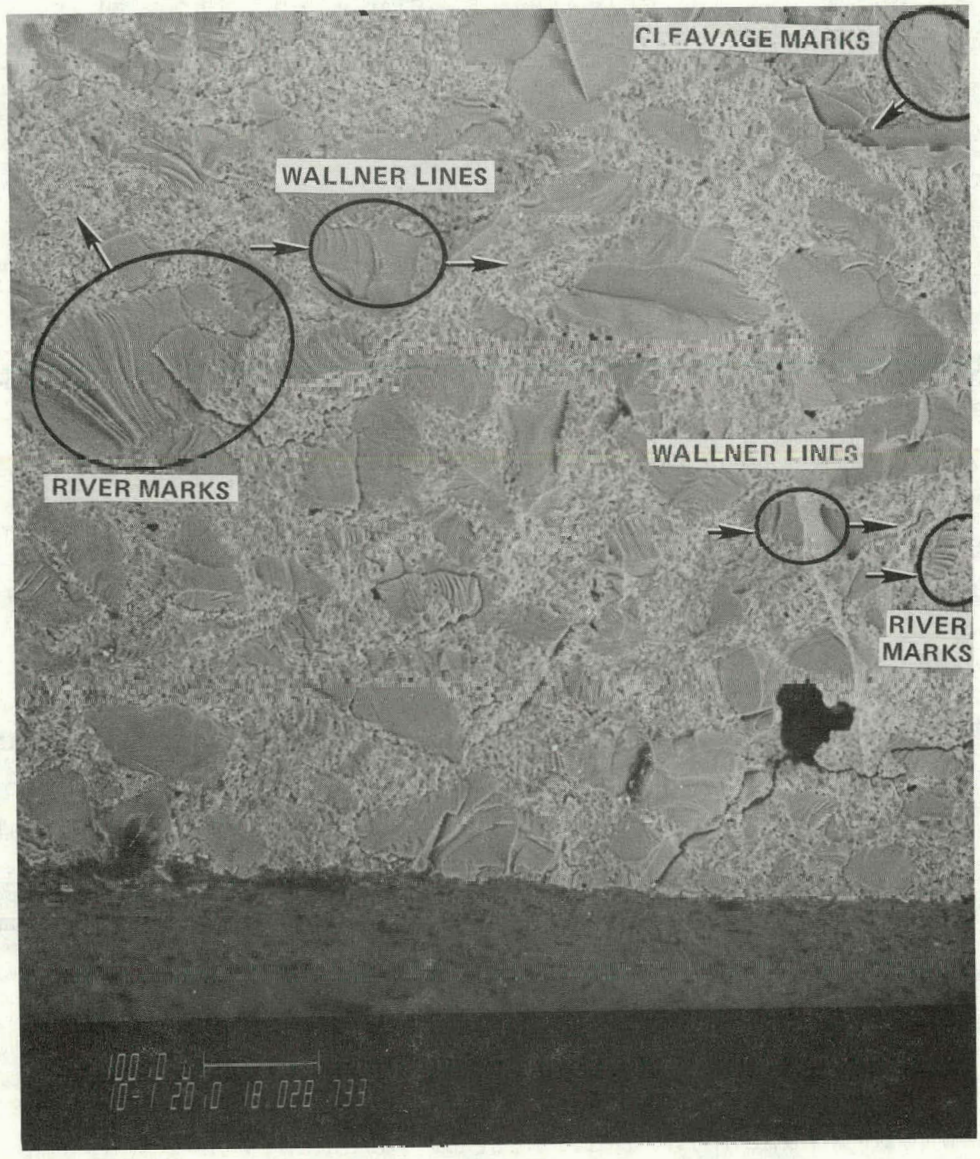

Figure 4-14. Crack Branching Area

The first specimen analyzed, designated CD-31, was prepared from an area of the recuperator tube in which NDE detected a number of pores each approximately 400 microns in diameter. The specimen fractured at three points at 23,000 psi. All three of the fractures appeared to be high stress fractures.

Two of the three fractures in this specimen contained hinges on the outside diameter which indicates that the crack started on the inside diameter surface and propagated toward the outside diameter. One of these two fractures occured directly under the loading point while the other fracture occurred in the testing zone. The latter break was examined to determine the origin of fracture. Figure 4-15 shows the fracture origin which appears to contain a cluster of large silicon carbide grains. It was concluded that both of these fractures are secondary since the crack started on the inside diameter surface.

Examining the overall topography of the third fracture resulted in the identification of a hinge on the inside diameter and a relatively smooth region on the fractured surface. This smooth region is a strong candidate to contain the fracture origin. Figure 4-16 shows an SEM photo of the fracture origin which was located in an area containing a number of pores. While the crack did not start at a pore, the pores could have influenced the crack propagation.

The second specimen examined has the designation of CD-23. Through the use of NDE, three pores were detected. These pores were estimated to be 400 microns in diameter. The C-ring specimen failed at 23,500 psi with two fractures. The primary break was identified due to location of the hinges and

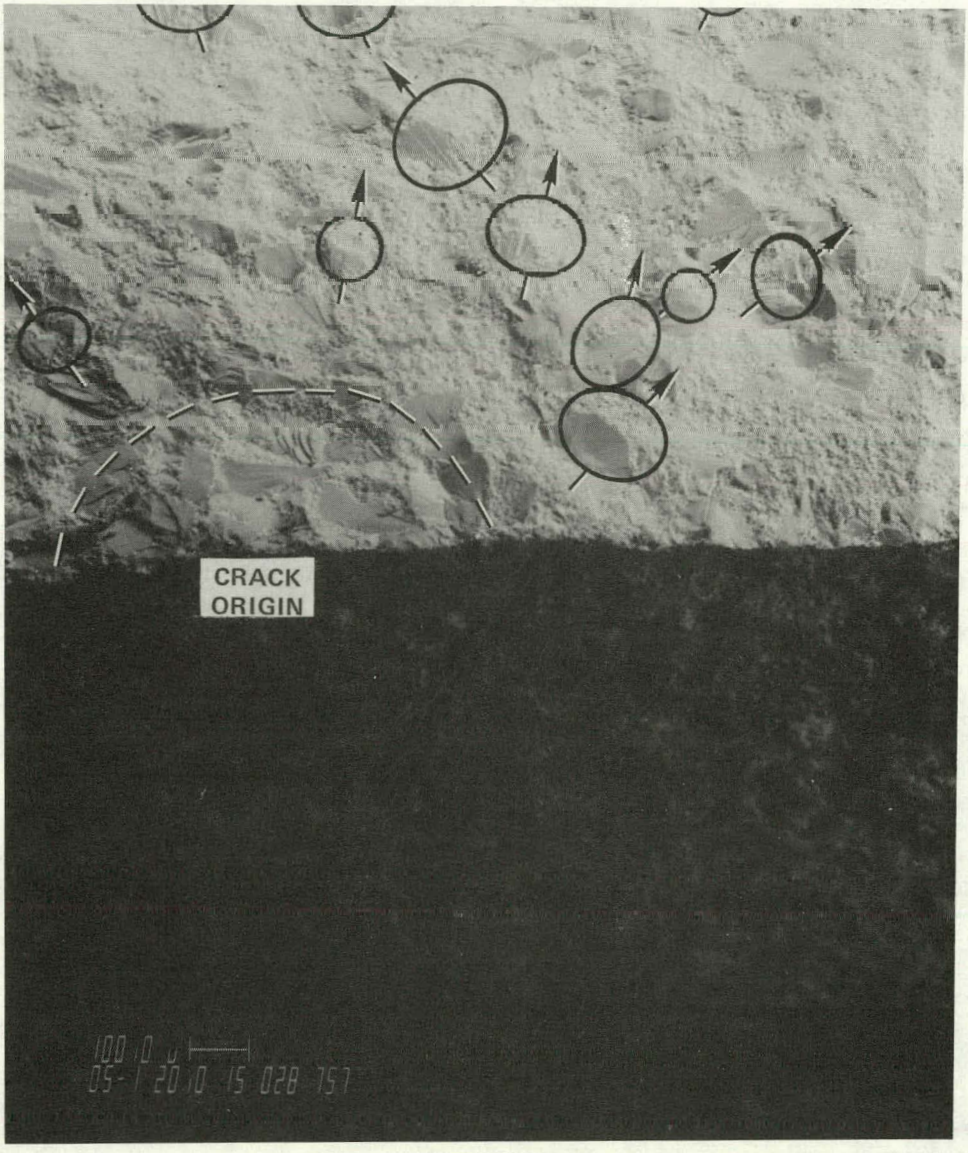

Figure 4-15. CD-31 Secondary Fracture

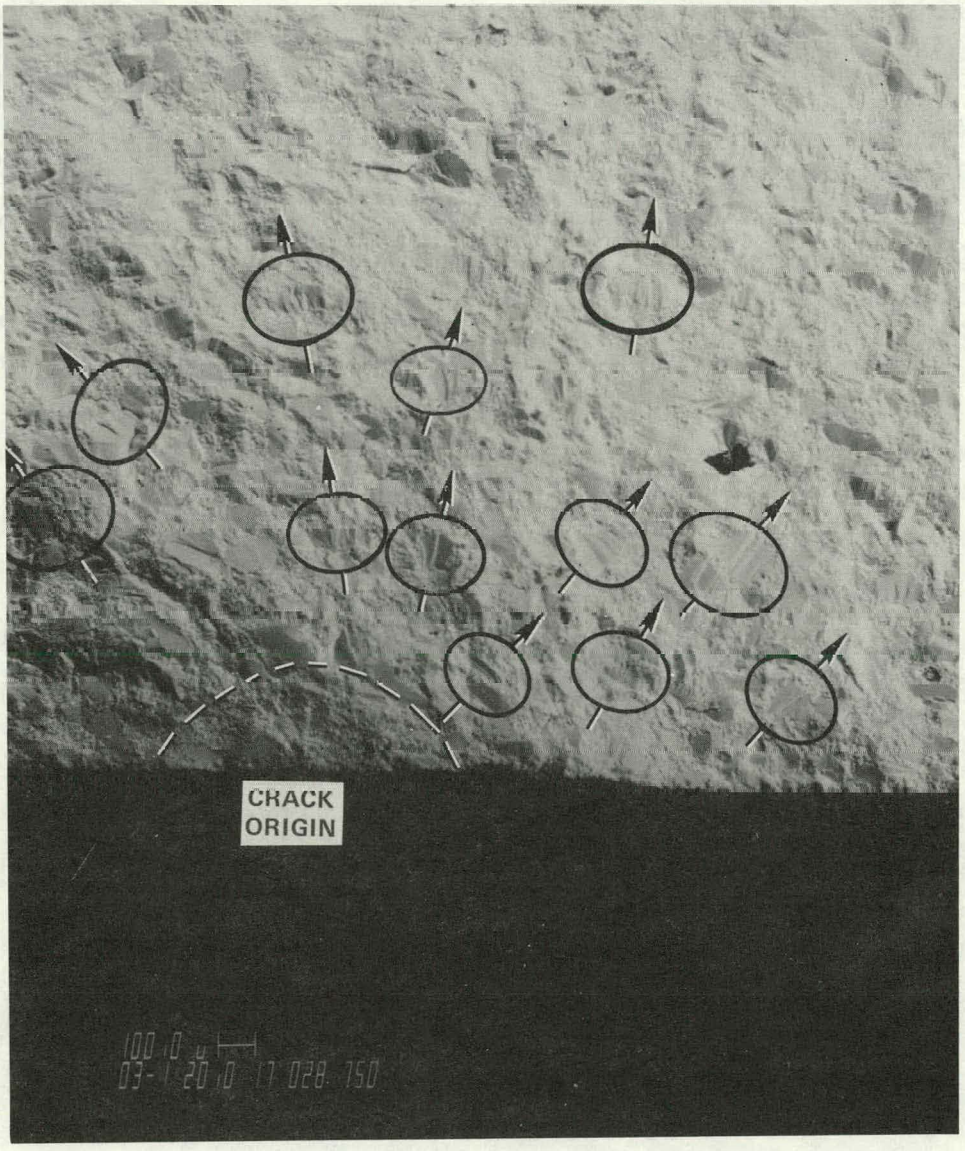

Figure 4-16. Primary Fracture

a topography that indicates a highly stressed fracture. This break occurred in an area identified by NDE as containing pores.

Figure 4-17 shows an overall view of the area containing the fracture origin. Present on this surface are a number of coarse hackle lines. The area at the hub of the hackle lines contains the fracture origin. Figure 4-18 shows a closer view of the fracture origin. Figures 4-19 and 4-20 compare the microstructure in and near the fracture origin and the microstructure in an area outside the fracture origin. The overall texture appears to be different. It also appears that there is a fine grained matrix on the fractured surface of the silicon carbide grain. It is believed that a crack in the silicon carbide grain had to exist before the firing operation in manufacturing to produce this feature.

The last specimen was CD-12 which contained one large void approximately 650 microns in length. The C-ring specimen fractured at 25,000 psi with three breaks. One break was directly under the loading pont and the topography indicated a low stress failure. The other two fractures indicated a high stress failure. One break was near the edge of the testing zone but appears to be the primary failure. This break was the only break with a hinge near the inside diameter.

The highly stressed secondary break was of interest since the fracture surface revealed the existence of a large void. Figure 4-21 shows an overview of this area and Figure 4-22 shows a photomicrograph of the void. It should be noted that this void was not the crack origin site. While the void should have influenced the crack propagation, the crack initiation site was actually just outside the void area. Figure 4-22 also shows the location of the edge of the fracture initiation site and Figure 4-23 shows the complete fracture origin.

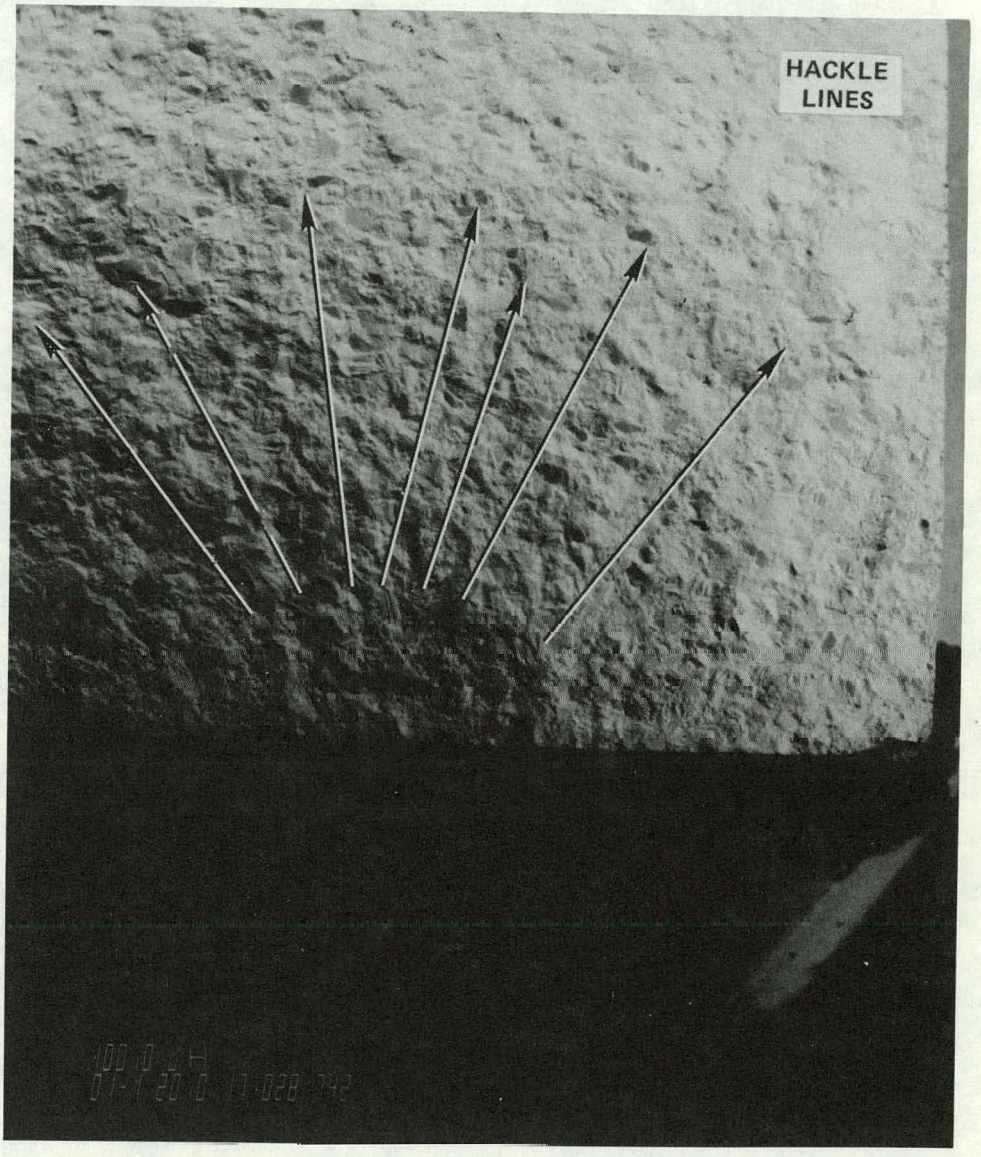

Figure 4-17. Specimen CD-23

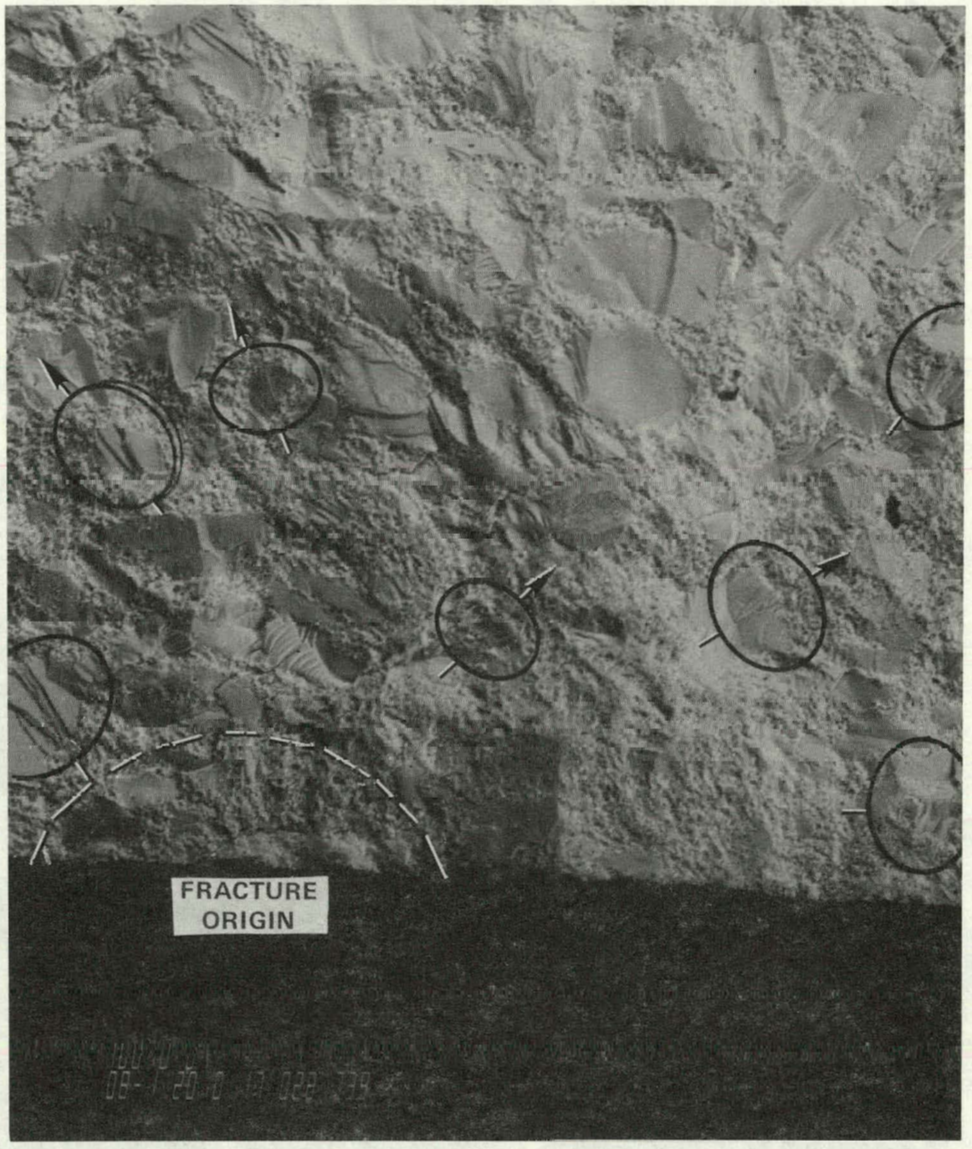

Figure 4-18. Fracture Origin

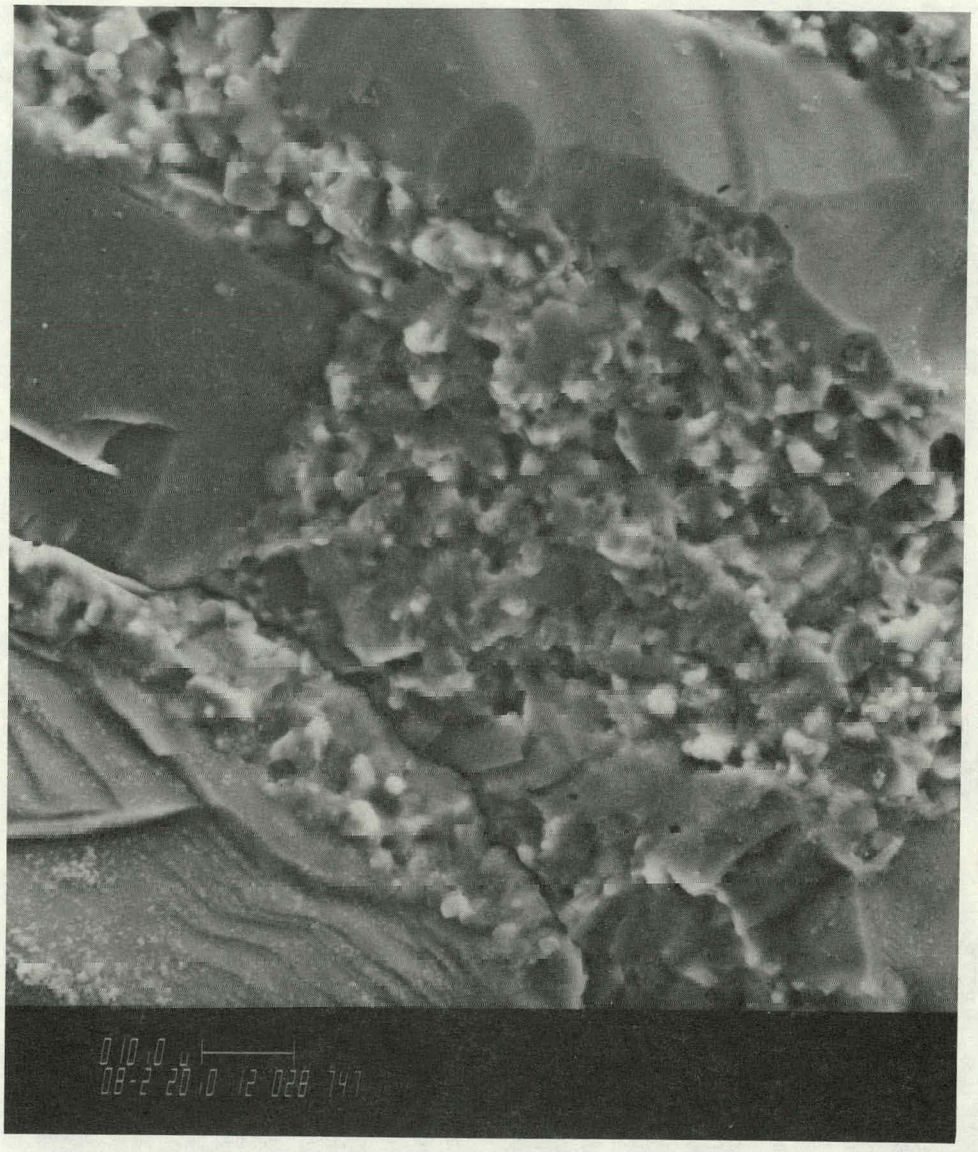

Figure 4-19. Microstructure Outside Fracture Origin

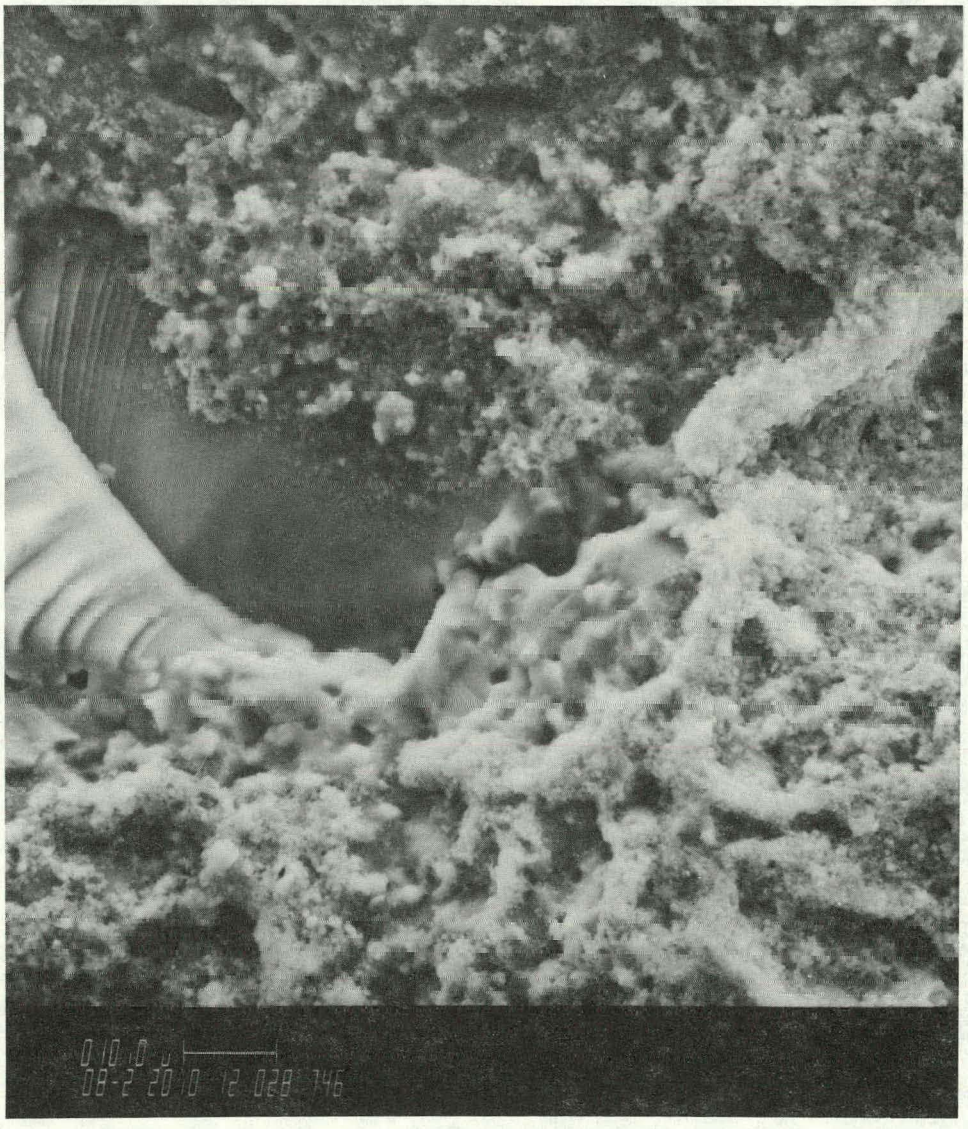

Figure 4-20. Microstructure in Fracture Origin

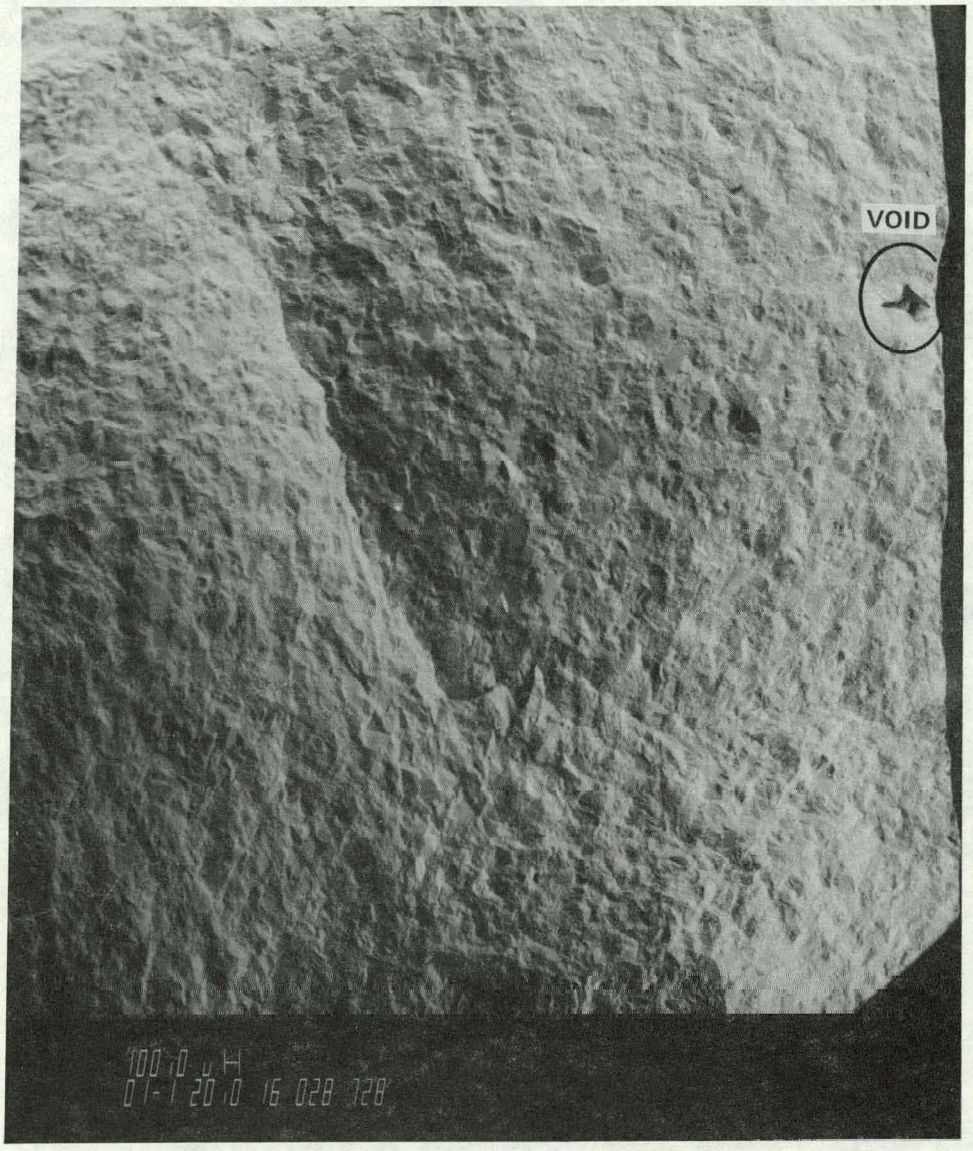

Figure 4-21. Secondary Fracture

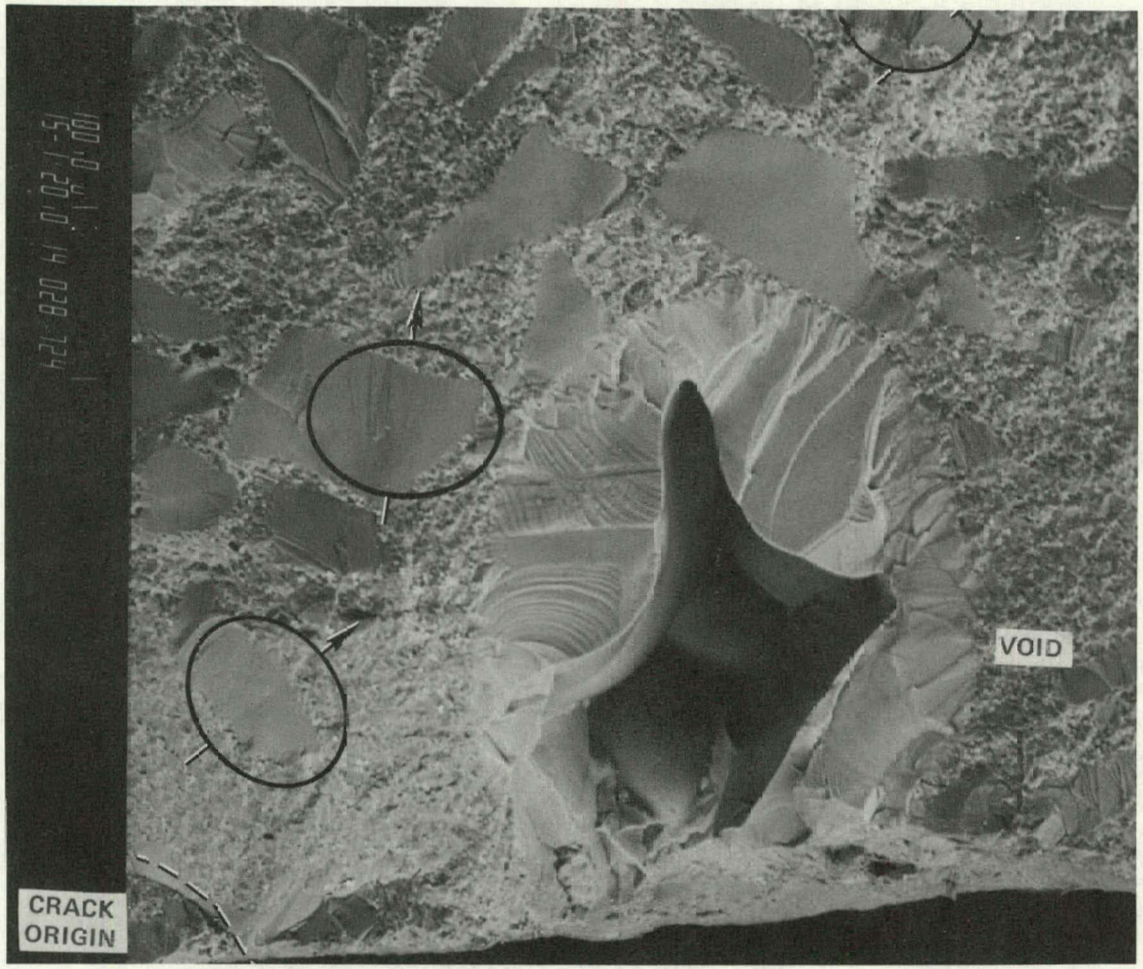

Figure 4-22. Void Present in Secondary Fracture

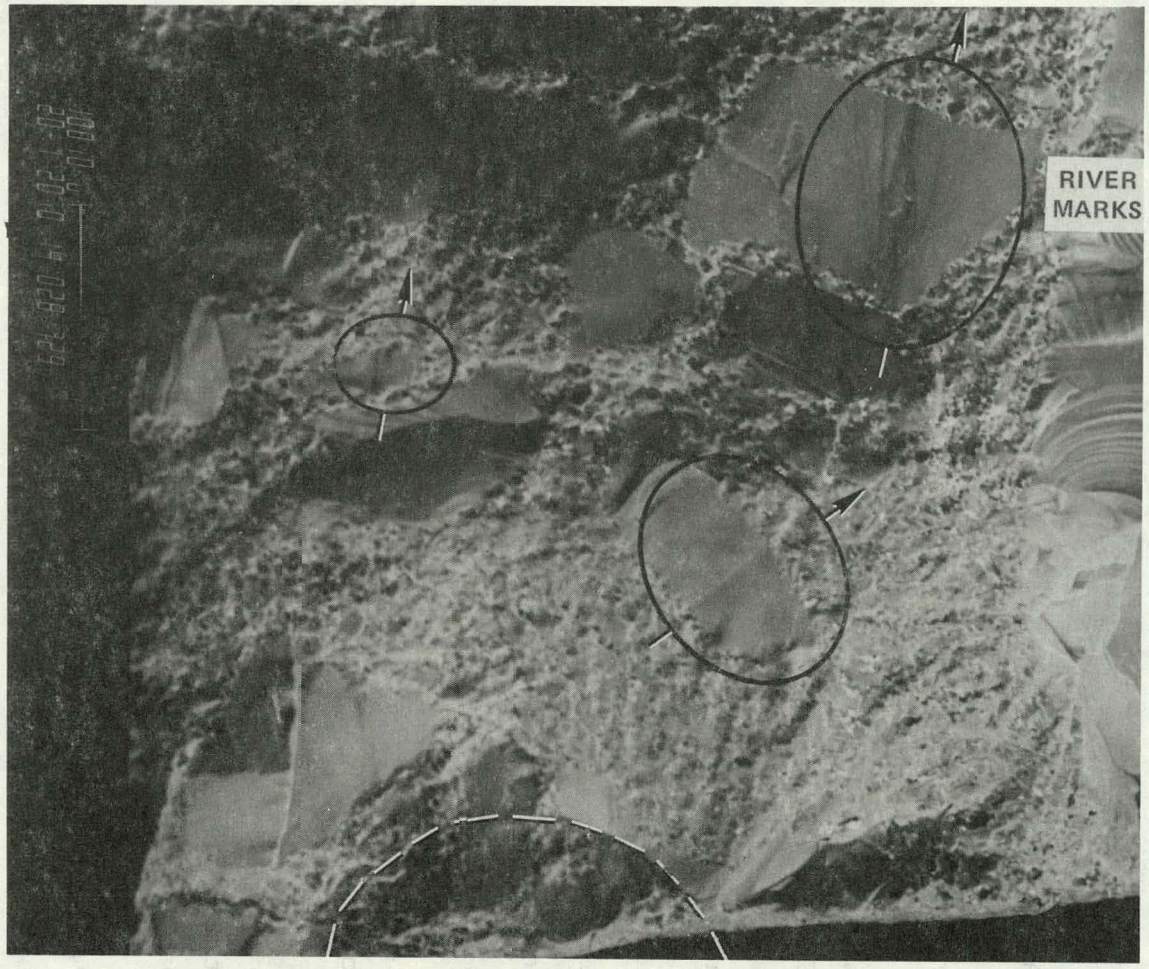

Figure 4-23. Crack Origin and Secondary Fracture

Section 5

CORRELATION OF NDE AND DESTRUCTIVE EVALUATION RESULTS

5.1 INTRODUCTION

Four NDE techniques were applied to silicon carbide plates and heat exchanger tube material. Three of them produced results: microfocus X-Ray, SLAM and conventional ultrasonics. Acoustic holography did not produce satisfactory results. The following section discusses the correlations between these tests, and concludes that they have complementary capabilities. Next, sizing correlations are briefly discussed. Finally, there is a discussion of strength correlations with NDE results.

It was found that some inclusions located were strength limiting. However, in most cases, failure originated at the surface of the sample as a result of strength testing by bending. It is well known that maximum stresses are at the surfaces and cutting ceramics always produces microcracks which lead to fracture. This type of stress is not truly representative of the thermal stresses on SiC tubes in service, and tubes in service will not have cut or ground surfaces. However, the testing used in this program establishes at least the minimum stress the material can withstand. The results also show that there are no major internal defects which might cause failure but which could escape detection by any of the three NDE methods.

5.2 DETECTION CORRELATION

Sample 528 - 6.6 x 6.6 x 1.2 cm plate, 99+% dense, surfaces as pressed.

This sample showed no significant defects on any test; that is, there are no indications which stand out above the background noise level in ultrasonics or above the surface roughness thickness variations in X-Ray. This sample is intact.

Sample 534 - 6.6 x 6.6 x 1.2 cm plate, 97% dense, cut in half and polished.

This sample has an internal circular structure detected by SLAM, ultrasonics, and X-Ray at both B&W and INEL. Figure 5-1 shows several C-scans made at B&W at different depths in the sample. The dark vertical line is the joint between the halves. The edge scan shows the indications to be centered in the sample.

Figure 5-2 is an INEL C-scan of one-half of Sample 534. The major indications match those in the B&W scan at 1.4 to 1.8 microsecond gate time.

Figure 5-3 is a microfocus X-Ray image of one-half. It shows a high density ring at the edge of the ultrasonically detected circular area.

Figure 5-4 is an INEL conventional X-Ray. It shows the same ring, but with less detail than the microfocus system.

Figure 5-5 is a SLAM view of a corner of the plate, showing the same circular pattern of density variations. It is interesting to note that X-Ray showed the density variation but no point like defects, while the ultrasonic tests showed many small and some large defects. The porosity pattern resulted from deliberate low densification, a method involving compression to a predetermined volume. None of the thinner samples showed this pattern.

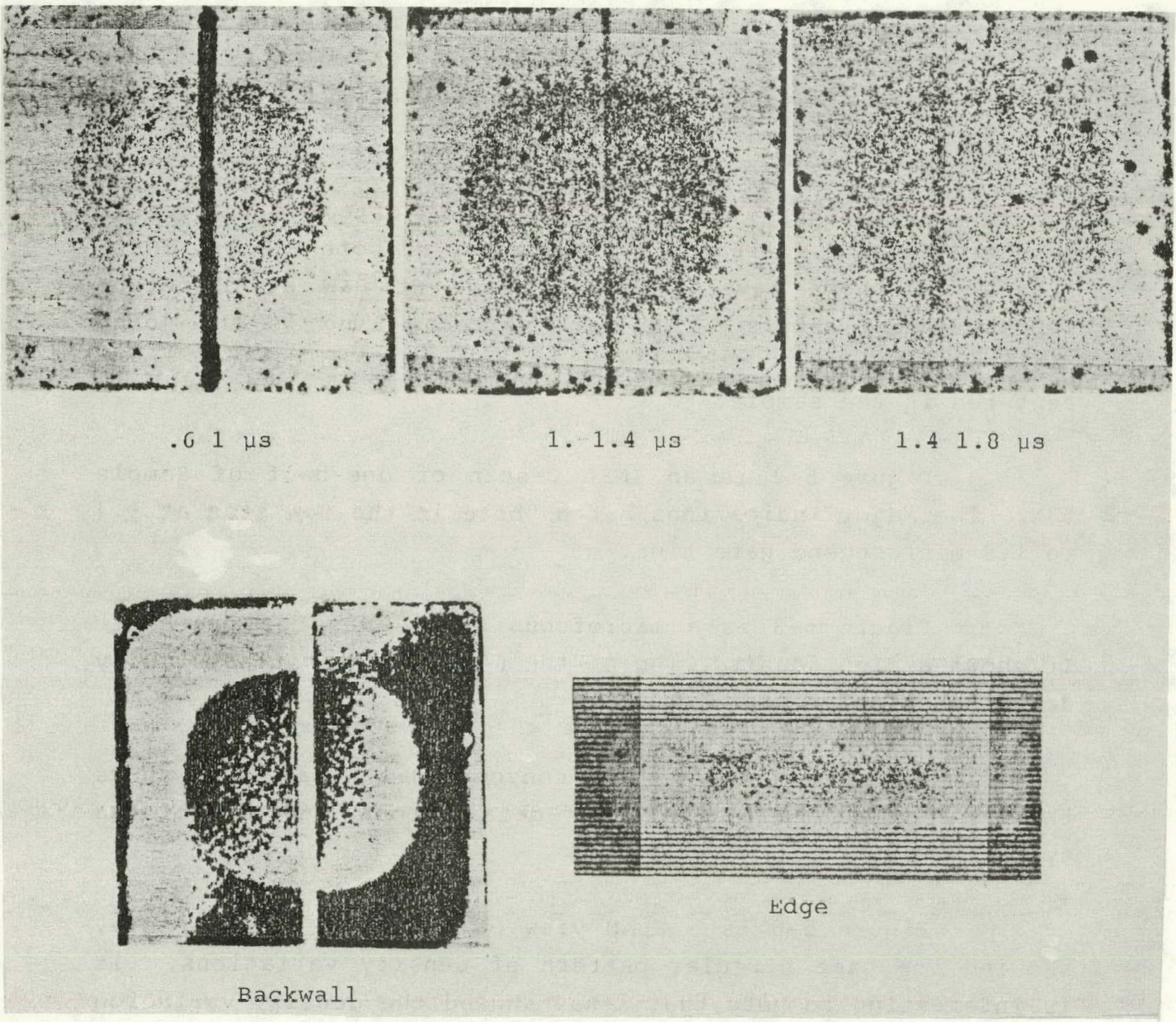

Figure 5-1. B&W C-Scans, Sample 534

Figure 5-2. INEL C-Scan, Sample 534

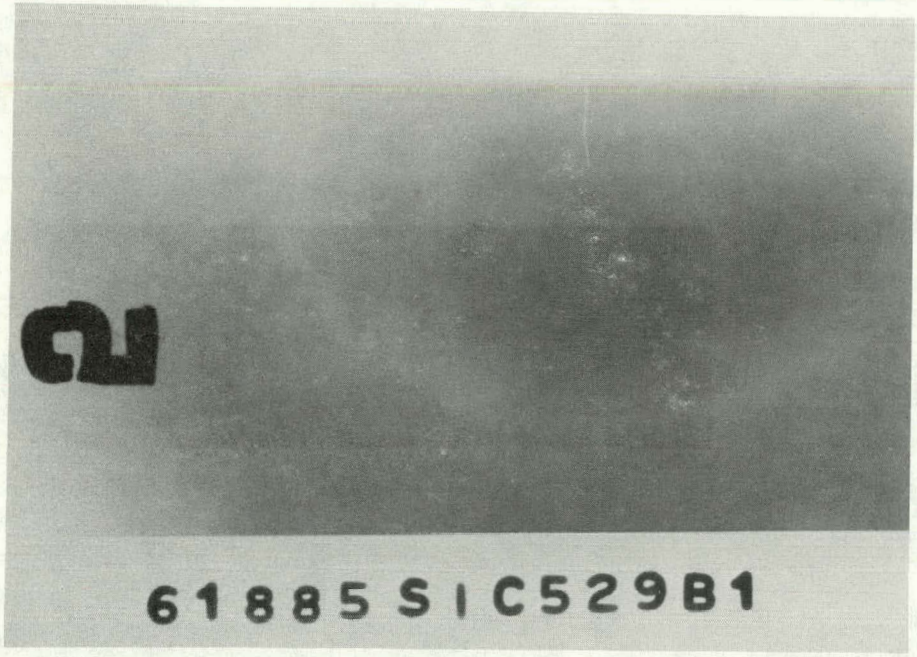

Figure 5-3. B&W Microfocus X-Ray, Sample 534

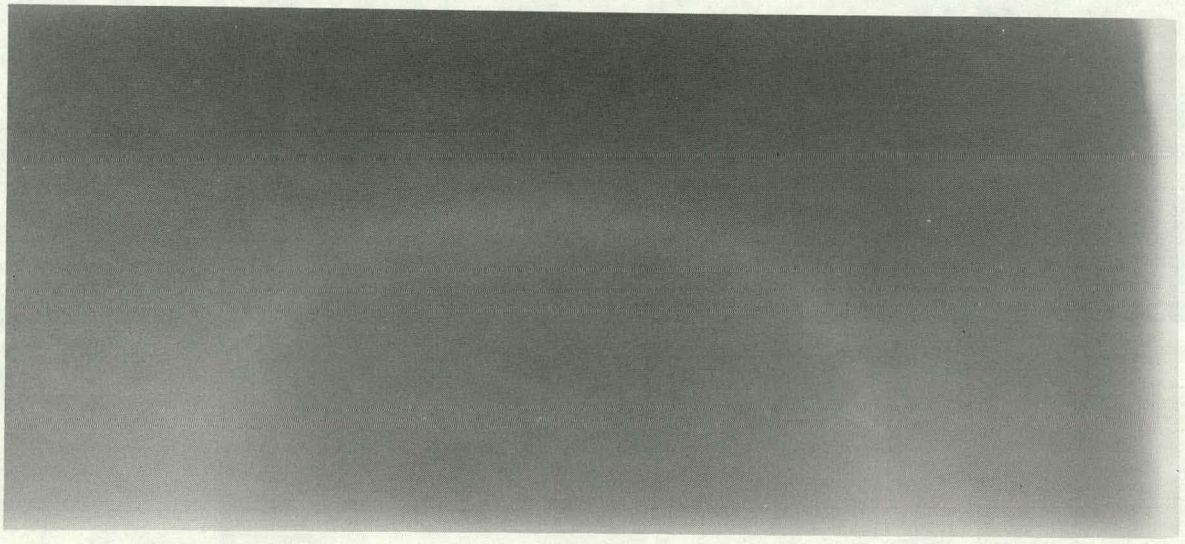

Figure 5-4. INEL X-Ray, Sample 534

Figure 5-5. SLAM Image, Sample 534

Sample 563 - 6.6 x 6.6 x 0.6 cm plate, 99% dense, dual use.

Sample 563 was first tested as pressed. There were no ultrasonic or SLAM indications. Microfocus X-Ray showed about 20 pores or low density inclusions in the 0.2 to 0.33 mm diameter range.

The sample was later cut in half and used for Knoop indent tests. The surfaces were ground and some were polished before indenting. The indents ranged from 8 to 400 newtons in load. The SLAM detected all indents; conventional ultrasonics detected the largest one; and microfocus X-Ray found none. Figure 5-6 shows SLAM images of several indents.

Sample 564 - 6.6 x 6.6 x 0.6 cm plate, 89.8% dense, cut in half and polished.

B&W ultrasonics found very high background, as expected for low density, high porosity material, with no significant indications. INEL C-scan found one particularly large indication; microfocus X-Ray found one low density inclusion; SLAM found nothing. The two inclusions reported were in different areas of the plate.

Half of the plate was cut into MOR (Modulus of Rupture) test bars.

Sample 565 - 6.6 x 6.6 x 0.6 cm plate, 99% dense, surface as pressed.

Microfocus X-Ray found four low density indications in the range of 0.3 to 0.6 mm. UT and SLAM found nothing. Half the sample was cut into MOR bars.

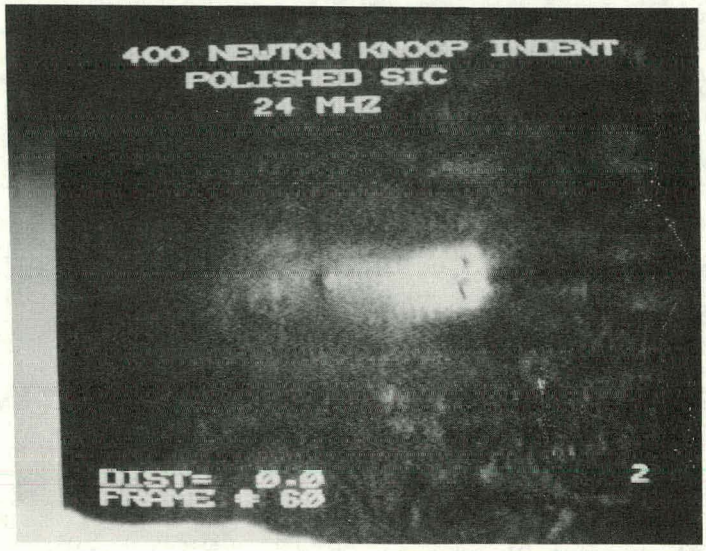

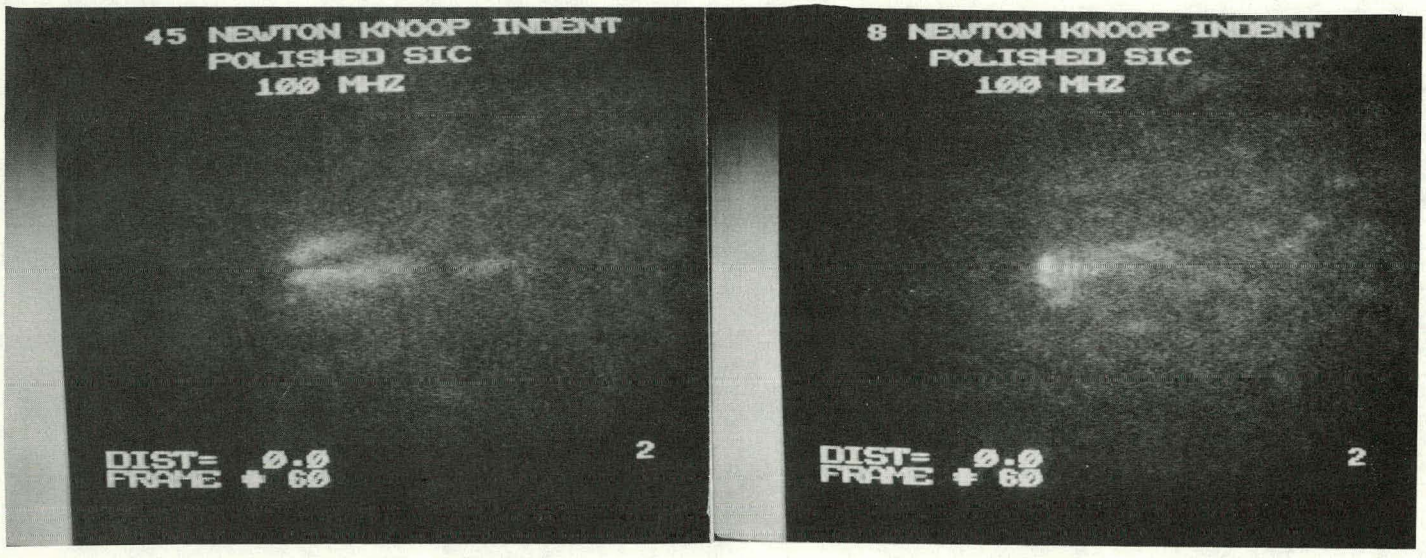

Figure 5-6. SLAM Images of Knoop Indents

Sample 566 - 6.6 x 6.6 x 0.6 cm plate, 91.5% dense, surfaces as pressed.

Microfocus X-Ray found five small indications of less than 0.5 mm. No other test method found anything. Half the sample was cut into MOR bars.

Sample 567 - 6.6 x 6.6 x 0.6 cm plate, 98.1% dense, surface as pressed.

Microfocus X-Ray found five small indications. No other test method found anything. This sample is completely intact.

Sample 568 - 6.6 x 6.6 x 0.6 cm plate, 97.6% dense, surfaces as pressed.

Microfocus X-Ray found one high density inclusion. No other tests found anything significant. Half the sample was cut into MOR bars.

Sample 570 - 6.6 x 6.6 x 0.6 cm plate, 98.8% dense, one surface ground.

This sample was seeded with four graphite inclusions. Three were detected by microfocus X-Ray, although they were not distinguishable from other inclusions except by their known locations. X-ray also found a large low density area. Ultrasonic C-scan detected one inclusion after one face was ground flat, but it was an insignificant indication. INEL C-scan detected none of the inclusions, but did find one other indication also found by B&W. SLAM found nothing significant.

Sample 571 - 6.6 x 6.6 x 0.6 cm plate, 99% dense, ground on one side.

This sample had embedded fibers. C-scan at B&W probably located two of them. X-Ray and INEL C-scan and SLAM located none. There were more accidental indications. Two were located by B&W and INEL C-scans, one by B&W only, and one by both C-scans and X-Ray. These were cut into MOR bars for testing. X-ray found other additional indications. SLAM found none.

Figure 5-7 shows two B&W C-scans and Figure 5-8 is the INEL C-scan.

Sample 759 - 6.6 x 6.6 x 0.6 cm plate, 99.5% dense, surfaces as pressed.

This sample had three wires embedded, two platinum and one tungsten-rhenium. They showed up extremely well in X-Ray, as would be expected for high atomic number materials in a low atomic number matrix. The X-Ray showed that the platinum flowed and distorted during the pressing operation. The wires were also detected by both B&W and INEL C-scans, but not by SLAM. Figures 5-9, 5-10, and 5-11 are X-Rays and C-scans of this plate.

Sample 763 - 6.6 x 6.6 x 0.6 cm plate, 96.5% dense, surfaces as pressed.

This plate contains four platinum spheres. They were readily detected by X-Ray but not by any other method.

Samples D1, D2, D3, D4 semicylindrical tube sections.

These four samples have EDM notches of various dimensions and orientations. Most notches were detected by all test methods. Only the 0.125 mm deep by 0.375 mm long

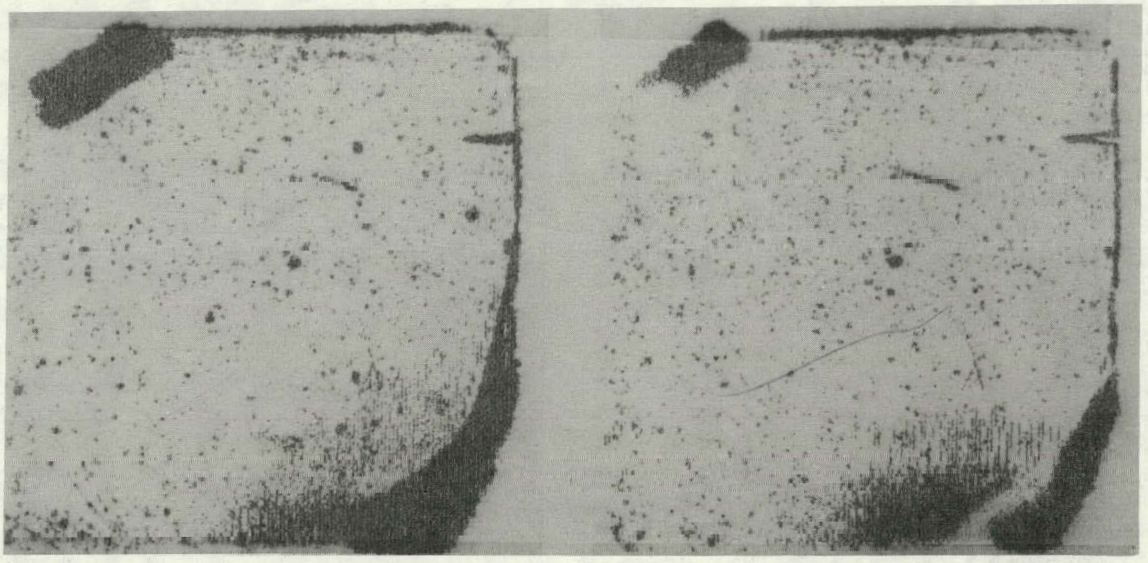

Figure 5-7. B&W C-Scans, Sample 571

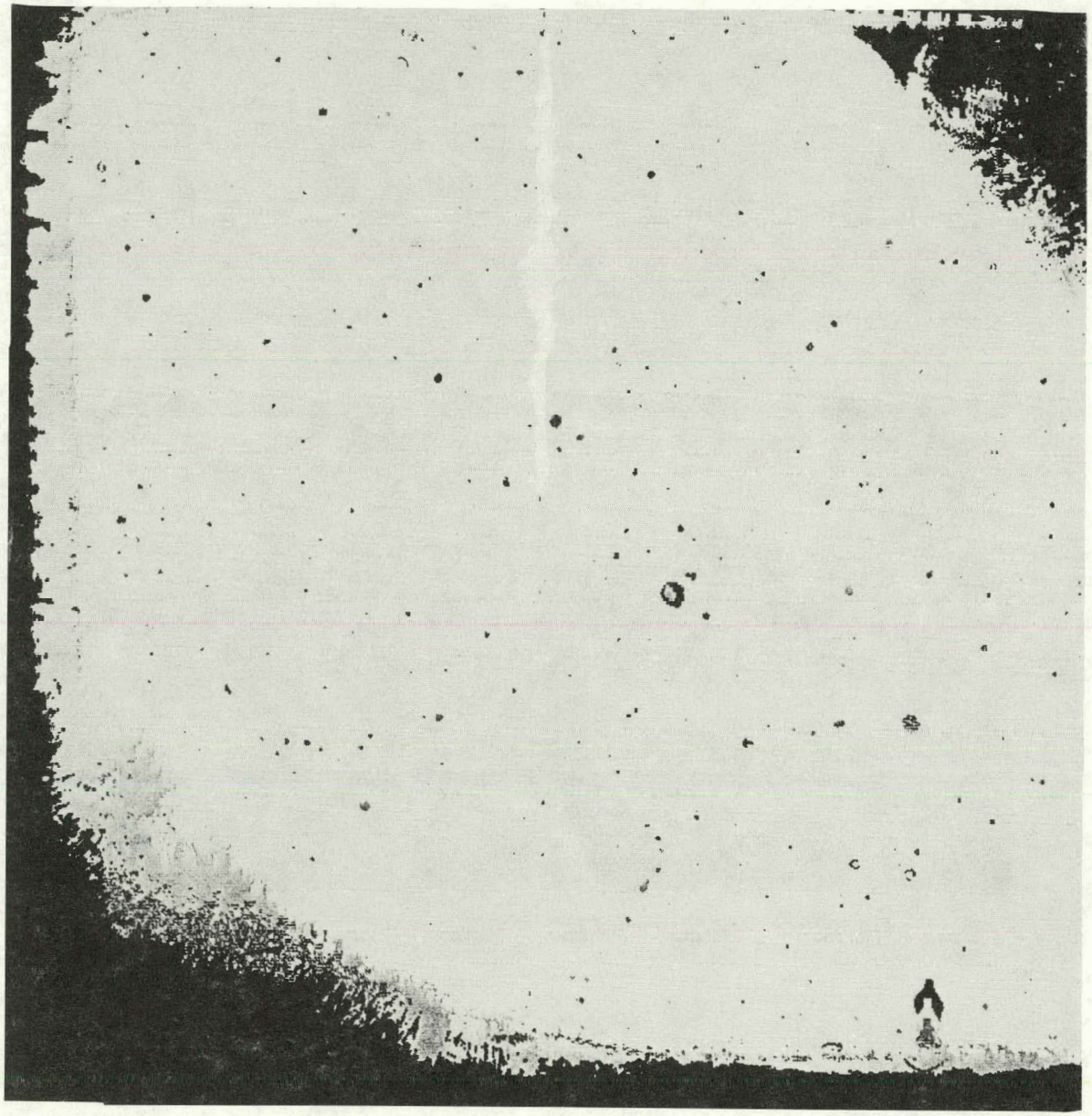

Figure 5-8. INEL C-Scan, Sample 571

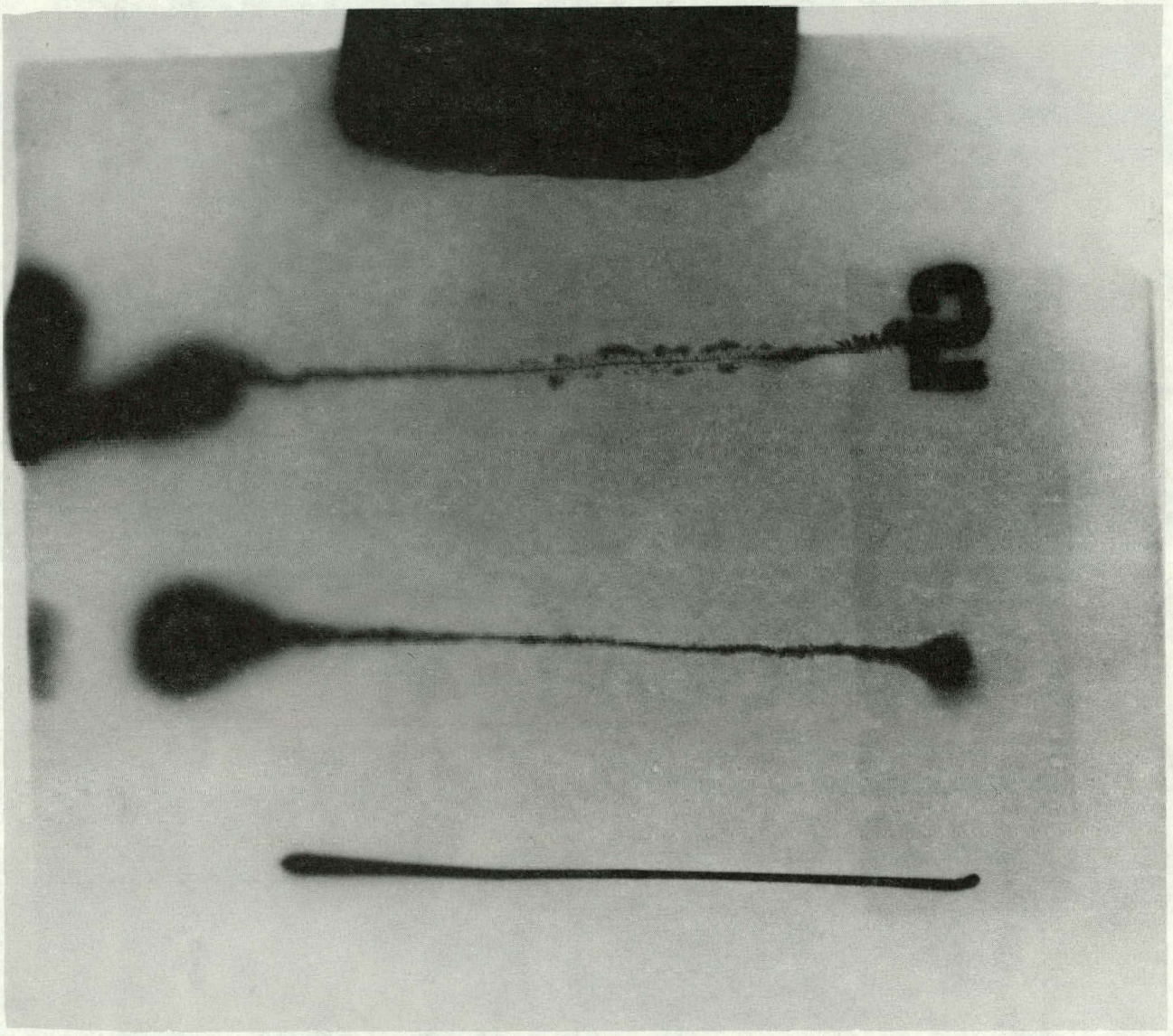

Figure 5-9. Microfocus X-Ray, Sample 759

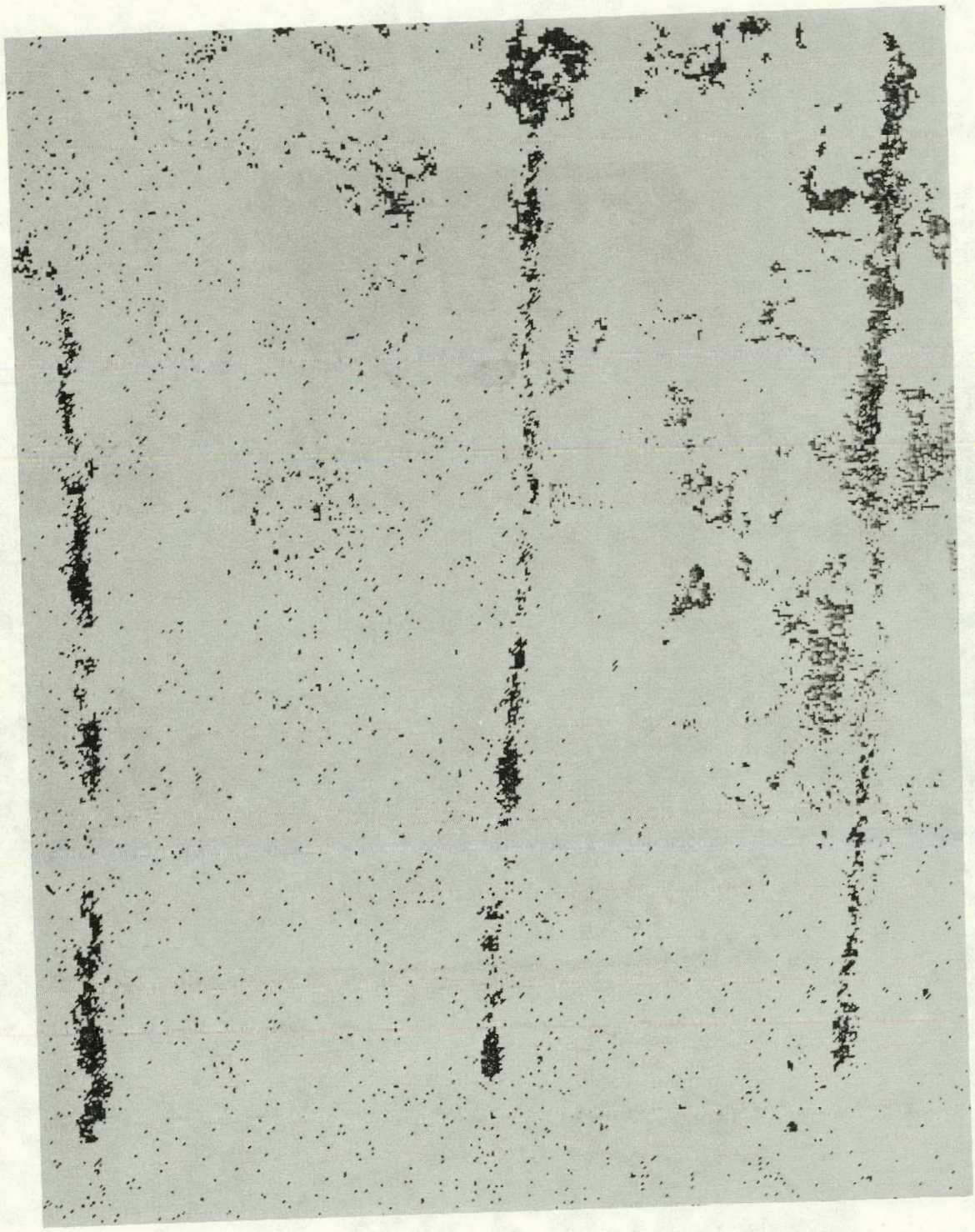

Figure 5-10. INEL C-Scan, Sample 759

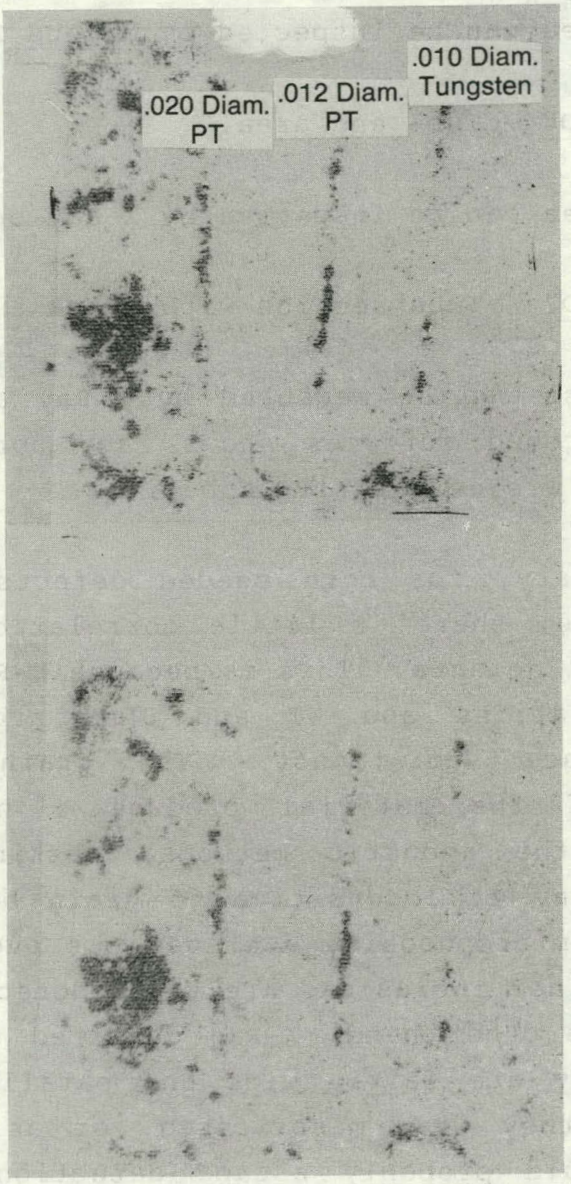

Figure 5-11. B&W C-Scan, Sample 759

notches were not detected by UT or SLAM. SLAM was also unable to detect notches on the inner surface of the tubes.

Sample D5 - Tube flange area.

This area can be inspected by UT and X-Ray.

Sample D6 - Tube end area.

This area can be inspected by X-Ray only.

Sample D7 - Tube section with thickness steps.

Thickness can be measured by X-Ray and UT. Visual inspection of ground surfaces shows many pores and silicon inclusions which are essentially spherical.

In summary, for both seeded defects and naturally occurring defects, there is little correlation between test results for small defects. This is because X-Ray is sensitive to density variations and UT and SLAM are sensitive to acoustic impedance variations. The grain boundary and microporosity of the material produce a high scattering background for the acoustic methods, masking other small inclusions. X-Ray is insensitive to grain boundary effects and the uniform microporosity averages out over the material thickness. If minor inclusions are to be detected, X-Ray must be used. On the other hand, X-Ray detected the EDM notches only because they are fairly wide and parallel to the beam direction. If they were misoriented, or as tight as real cracks, they would probably escape detection, just as the Knoop indents did. UT and SLAM are sensitive only to the presence of an open crack, not its width. If cracks are to be detected, UT or SLAM must be used. SLAM is by far the fastest method of scanning for OD cracks, but only UT will find ID cracks.

5.3 SIZING CORRELATIONS

Sizes determined by microfocus X-Ray are accurate to within the spot size, a few micrometers. Sizes determined by UT or SLAM are determined by the interaction of the beam and the defect, and determining a size for a small defect is much more difficult. In the actual tube material, UT and SLAM can determine the length of an OD surface breaking crack, but the depth is more difficult to determine because the rough surface makes determination of beam direction nearly impossible.

5.4 STRENGTH CORRELATIONS

5.4.1 Strength vs. Density

Section 4.2 describes testing of MOR test bars. The test results indicate that the average of the strength values for the 99+% dense material was 20 to 25% higher than that for 90% dense material, as measured by stress to failure. There is considerable scatter in the data. The figures in Section 4.2 are averages; Figure 5-12 shows the original data. The sets of connected points are samples from the same billet. The variation of density within the billets is significant, so the variation along the length of individual bars is probably also significant, but is unknown.

5.4.2 Strength vs Defects

The variable density MOR bar billets were examined before cutting the bars. The only indications were found by microfocus X-Ray. The bars contained three high density and one low density inclusion in the central, stressed region of the bars. None of the bars broke near the inclusions.

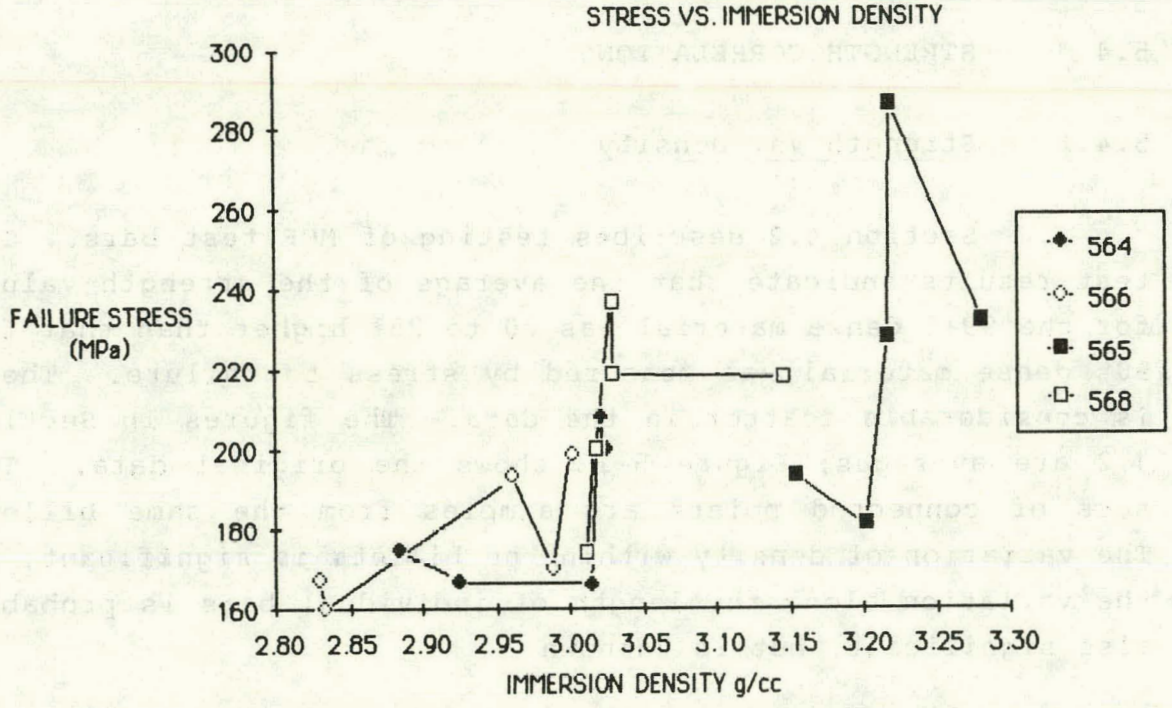

Figure 5-12. Strength vs. Density of MOR Bars

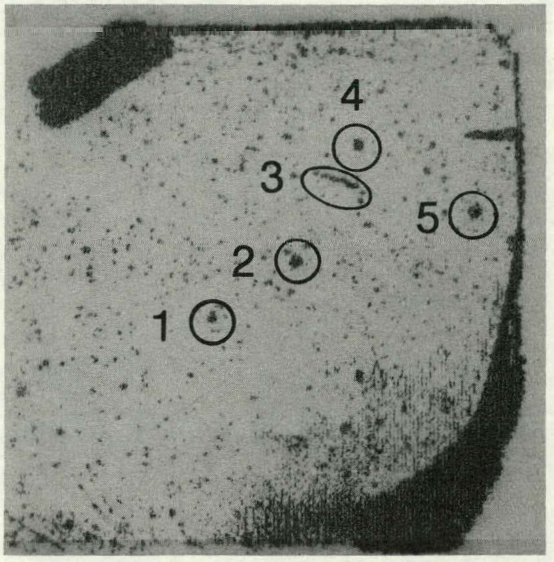

Figure 5-13. Defects included in MOR Bars

Additional testing as described in Section 4.2 was carried out on MOR bars cut from Sample 571, the seeded fiber sample. Figure 5-13 shows a B&W C-scan of this sample, with the selected defects circled. The strength results are in Table 4-5. The correlations are as follows:

Defect 1 is present but not significant on both INEL and B&W C-scan, and present as a low density defect in X-Ray. The bar did not break on this inclusion.

Defect 2 is the largest indication on the INEL C-scan, large in the B&W C-scan, and barely visible in X-Ray. The bar broke at this defect, but it was at the highest stress of any of the 25 bars tested. It would not have been strength limiting in any of the other bars.

Defect 3 is a linear indication, seen only by B&W C-scan. It runs the full width of the bar, and was not strength limiting. This was the second strongest bar.

Defect 4 was fairly large on both INEL and B&W C-scans, but was not visible on X-Ray. The bar did not break on the inclusion, nor on the part of defect 3 which extended into this bar.

Defect 5 was large in the B&W shallow C-scans, did not show up in INEL C-scans or deep B&W scans, nor on X-Ray. The bar broke at the indication.

It is interesting that the two bars which failed at the indications had branched fractures, resulting in production of a chip of ceramic. The others failed by single fracture.

5.4.3 C-Rings

Twelve C-rings were cut with defects detected by microfocus X-Ray located at the center of the C. Their testing is described in Section 4.2. Because they were tested in compression, the tube's outer surface was in tension. We would expect defects near the outer surface to fail first. Two of the rings failed with a single, branched, fracture. The others had two, three, or four well separated fractures.

The only ring which failed at the identified defect was #9, which had a circumferential crack about 2.5 cm long. The break runs from the edge of the ring to the crack, follows the crack (which is perpendicular to the break direction) about 7 mm, and then turns again to the other edge.

After the rings were broken, the X-Rays were re-examined for indications at the break sites. Nothing unusual was found.

One crack in ring 2 passed through the side of an inside surface pore. The pore opening diameter is 0.25 mm and there is a width of about 0.01 mm between the crack and the pore opening. At a depth of about 0.1 mm, the side of the pore is open to the crack, with a hole of 0.03 mm. In spite of this near miss, there is no sign that the fracture surface shape was affected by the presence of the pore.

In ring 4, there is an outer (tension) surface pore of diameter 0.6 mm, and ring 5 has a group of three from 0.1 mm to 0.3 mm. Neither of these failed at a pore, although they had three and four fractures, respectively.

The same pores are found in other samples, but surface breaking pores are not critical in this material.

Section 6
SUMMARY OF RESULTS

6.1 APPLICABILITY OF THIS WORK TO THE DESIGN OF CERAMIC TUBES

The goal of the entire three phase program is to assure energy efficient lifetimes of high temperature structural ceramics by being able to specify acceptance criteria on ceramics. These criteria are to be validated through nondestructive methods and fracture mechanics. Meeting this goal requires the ability to specify what defects can be detected and what effect the detected defects have on strength. With these results, it will be possible to design tubes for long life in various applications and to test them to assure that no defects are present to prevent their survival.

The results of this first study are more limited, but still provide useful guidelines. First, surface irregularities are a major limitation to testing. The eventual tests will be much more sensitive if surface finish can be improved. Second, porosity is another major limit to testing. Pores are not generally strength limiting in this material, except perhaps as porosity reduces the amount of ceramic present. But pores scatter ultrasound very badly and produce irregular densities on X-Ray film, in both cases obscuring more important defect indications. Third, the dimple shape of the closed end is essentially untestable. Unless there are very strong reasons for maintaining this shape, a smooth curve with no external concavity would be much easier to test.

The fourth design guideline is provided by the fractography results. In some cases, failure was initiated in or near clusters of large grains. Whether the cause was the grains themselves, or microcracking caused by a cluster of grains having a thermal expansion coefficient different from the rest of the material, is not clear. However, avoiding clusters of large grains in the starting material would remove these failure initiation sites.

6.2 RECOMMENDATIONS FOR FUTURE WORK

Ultrasonic testing, SLAM, and microfocus X-Ray have all proved capable of detecting flaws in ceramics. SLAM could be further improved by adding Acoustic Holography capability, although the improvement to be expected in material as strongly scattering as the tube material is questionable. Microfocus X-Ray will be definitely improved by adding computed tomography capability.

With the applicable test methods established, the next step should be to proceed toward finding out what defects are present, whether they can be detected, and their influence on strength. It is apparent from this work that minor pores and inclusions are not nearly so critical as cracks, which are usually the source of failure in test specimens. The next stage of testing should concentrate on locating cracks, and separating crack indications from others. Testing is needed to determine the stresses which will cause cracks to grow. There will always be microcracks, but larger cracks grow at lower stress. The limit of crack detectability and the stress needed to cause growth of cracks below the limit will set the stress limit on tube designs.

Section 7
REFERENCES

1. D. Weinstein and H. J. Shaw, PVF2 Transducers for Nondestructive Evaluation of Ceramics and Brittle Materials, AFOSR-TR-81-0881, Edward L. Ginzton Laboratory of Physics, Stanford University, Stanford, California, 1981, pp. 1-67.

2. L. W. Kessler, D. E. Yuhas, C. L. Vorres, "Acoustic Microscopy of Ceramics", Technical Paper, Nondestructive Evaluation, Sonoscan, Inc., Bensenville, Illinois, 1981.

3. R. L. Thomas, Laser Photoacoustic Technique for NDE, ARO-1574.14-MS, Department of Physics, Wayne State University, Detroit, Michigan, 1981, pp. 1-6.

4. J. C. Glandus, P. Boch, "High and Medium Frequency Nondestructive Testing of the Thermal Shock Resistance of Ceramics", Technical Paper, National Ceramic Industries, Limoges, France, 1982.

5. D. E. Yuhas, M. G. Oravecz, L. W. Kessler, "Quantitative Flaw Characterization by Means of the Scanning Laser Acoustic Microscope (SLAM)", Review of the Progress in Quantitative Nondestructive Evaluation, Vol. 1, Plenum Press, New York, NY (1982), pp. 761-766.

6. L. J. Bond, N. Jayasundere, D. A. Sinclair, I. R. Smith, "Investigation of Ultrasonic Transducers as used for Nondestructive Testing", Review of the Progress in Quantitative Nondestructive Evaluation, Vol. 1, Plenum Press, New York, NY (1982), pp. 691-701.

7. L. J. Inglehart, R. L. Thomas, L. D. Favro, P. K. Kuo, "Scanning Photoacoustic Microscopy (SPAM) of Si_3N_4 Ceramic Test Bars", Review of the Progress in Quantitative Nondestructive Evaluation, Vol. 1, Plenum Press, New York, NY (1982), pp. 673-676.

8. L. J. Inglehart, R. L. Thomas, J. Schuldies, "Photoacoustic Microscopy of Ceramic Engine Hardware", Journal of Nondestructive Evaluation, 1, December 1980, pp. 287-293.

9. C. H. Chou, B. T. Khuri-Yakub, G. S. Kino, A. G. Evans, "Defect Characterization in the Short-Wavelength Regime", Journal of Nondestructive Evaluation, 1, December 1980, pp. 235-247.

10. D. S. Kupperman, M. J. Caines, A. Winiecki, "Assessment of Ultrasonic NDE Methods for Ceramic Heat Exchanger Tubes", Materials Evaluation, 40, June 1982, pp. 774-782.

11. D. J. Cassidy, Ceramics for High Performance Applications 2, Brook Hill Publishing Company, Chestnut Hill, Massachusetts (1978), pp. 231-242.

12. L. D. Favro, L. I. Inglehart, P. K. Kuo, J. J. Pouch, R. L. Thomas, "Photoacoustic Microscopy", DARPA/AFWAL Review of the Progress in Quantitative NDE, LaJolla, California, 14-18 July 1980, Materials Laboratory, Air Force Wright Aeronautical Laboratories, Wright-Patterson Air Force Base, Ohio (1981), pp. 236-238.

13. J. J. W. Tien, B. T. Khuri-Yakub, G. S. Kino, A. G. Evans, D. Marshall, "Surface Acoustic Wave Measurements of Surface Cracks in Ceramics", DARPA/AFWAL Review of the Progress in Quantitative NDE, LaJolla, California, 14-18, July 1980, Materials Laboratory, Air Force Wright Aeronautical Laboratories, Wright-Patterson Air Force Base, Ohio (1981), pp. 144-150.

14. B. T. Khuri-Yakub, C. H. Chou, K. Liang, G. S. Kino, "NDE for Bulk Defects in Ceramics", DARPA/AFWAL Review of the Progress in Quantitative NDE, LaJolla, California, 14-18, July 1980, Materials Laboratory, Air Force Wright Aeronautical Laboratories, Wright-Patterson Air Force Base, Ohio (1981), pp. 137-143.

15. D. K. Goebbels, H. Reiter, "Characterization of Defects and Heterogeneities in Silicon Nitride and Silicon Carbide by Different NDE Methods", DARPA/AFWAL Review of the Progress in Quantitative NDE, LaJolla, California, 8-13, July 1979, Rockwell International Science Center, Thousand Oaks, California (1980), pp. 713-718.

16. D. S. Kupperman, W. D. Deininger, N. P. Lapinski, C. Sciammarella, D. Yuhas, "Nondestructive Evaluation Techniques for Silicon Carbide Heat Exchanger Tubing", DARPA/AFWAL Review of the Progress in Quantitative NDE, LaJolla, California, 8-13, July 1979, Rockwell International Science Center, Thousand Oaks, California (1980), pp. 700-712.

17. T. Derkocs, I. M. Matay, "Ultrasonic Detection of Surface Flaws in Gas Turbine Ceramics", DARPA/AFWAL Review ofthe Progress in Quantitative NDE, LaJolla, California, 8-13, July 1979, Rockwell International Science Center, Thousand Oaks, California (1980), pp. 691-699.

18. D. E. Yuhas, T. E. McGraw, L. W. Kessler, "Scanning Laser Acoustic Microscope Visualization of Solid Inclusions in Silicon Nitride", DARPA/AFWAL Review of the Progress in Quantitative NDE, LaJolla, California, 8-13, July 1979, Rockwell International Science Center, Thousand Oaks, California (1980), pp. 683-690.

19. D. E. Yuhas, T. E. McGraw, L. W. Kessler, "Differentiation of Various Flaw Types in Ceramics using the Scanning Laser Acoustic Microscope", DARPA/AFWAL Review ofthe Progress in Quantitative NDE, LaJolla, California, 8-13, July 1979, Rockwell International Science Center, Thousand Oaks, California (1980), pp. 678-682.

20. J. Tien, B. Khuri-Yakub, G. S. Kino, "Acoustic Surface Wave Probing of Ceramics", DARPA/AFWAL Review of the Progress in Quantitative NDE, LaJolla, California, 8-13, July 1979, Rockwell International Science Center, Thousand Oaks, California (1980), pp. 671-677.

21. L. A. Ahlberg, R. K. Elsley, L. J. Graham, J. M. Richardson, "Long Wavelength Ultrasonic Characterization of Inclusions in Silicon Nitride", DARPA/AFWAL Review of the Progress in Quantitative NDE, LaJolla, California, 8-13, July 1979, Rockwell International Science Center, Thousand Oaks, California (1980), pp. 656-662.

22. M. Srinivason, D. Lawler, L. J. Inglehart, R. L. Thomas, D. Yuhas, "Comparison of NDE Techniques for Sintered - SiC Components", Proceedings, 6th annual Conference on Composites and Advanced Ceramic Materials, Cocoa Beach, Florida, January 17-21, 1982.

23. T. M. Yonushonis, A. A. Scilingo, K. A. Lark, "Flourescent Dye Penetrant Inspection of Silicon Nitride Bearing Surfaces", Review of the Progress in Quantitative Nondestructive Evaluation, Vol. 1, Plenum Press, New York, NY (1982), pp. 263-267.

24. S. J. Klima, G. K. Watson, T. P. Herbell, T. J. Moore, Ultrasonic Velocity for Estimating Density of Structural Ceramics, 0499-9320, Lewis Research Center, Cleveland, Ohio, 1982.